Experimental and Analytical Assessment of Cavity Modes in a Gas Turbine Wheelspace

by

Rachel A. Berg

B.S Aerospace Engineering (2007) and M.S. Mechanical Engineering (2008)
Worcester Polytechnic Institute

Submitted to the Department of Aeronautics and Astronautics
in partial fulfillment of the requirements for the degree of

Master of Science in Aeronautics and Astronautics

at the

MASSACHUSETTS INSTITUTE OF TECHNOLOGY

February 2016

Signature redacted

Author .....
Department of Aeronautics and Astronautics
January 15, 2016

Signature redacted

Certified by .....
Choon S. Tan
Senior Research Engineer of Aeronautics and Astronautics
Thesis Supervisor

Signature redacted

Certified by .....
Greg M. Laskowski
Principal Engineer at GE Aviation
Thesis Supervisor

Signature redacted

Accepted by .....
Paulo C. Lozano
Associate Professor of Aeronautics and Astronautics
Chair, Graduate Program Committee

Experimental and Analytical Assessment of Cavity Modes in a Gas Turbine Wheelspace

by

Rachel A. Berg

Submitted to the Department of Aeronautics and Astronautics
On January 15, 2016, in partial fulfillment of the
requirements for the degree of
Master of Science in Aeronautics and Astronautics

Abstract

High response pressure data from a high-speed 1.5-stage turbine Hot Gas Ingestion Rig shows the existence of cavity modes in the rim-seal-wheelspace cavity for representative turbine engine operating conditions with purge flow. The experimental results and observations are complemented by computational assessments of cavity modes associated with flow in canonical cavity configurations. The cavity modes identified include Shallow Cavity modes and Helmholtz resonance. The response of the cavity modes to variation in design and operating parameters are assessed. These parameters include cavity aspect ratio, purge flow ratio, and flow angle defined by the ratio of primary tangential to axial velocity. Scaling the cavity modal response based on computational results and available experimental data in terms of the appropriate reduced frequencies appears to indicate the potential presence of a Deep Cavity mode as well. Computational assessment of canonical cavity flow suggests that increasing purge flow ratio mitigates Shallow Cavity modal response, in accord with data for the first Shallow Cavity mode but in contrast to data for the second Shallow Cavity mode. Likewise, increasing primary flow angle reduces the Shallow Cavity modal response that vanishes for flow angle beyond 45°. This computational observation is in contrast to the rig data that show the modal response is nevertheless present with a flow angle greater than 45°. An implication from the computational parametric assessments is that increasing purge flow and primary flow angle could provide a stabilizing effect on the response. Experimental requirements to quantify the effects of cavity modes on hot gas ingestion are identified along with inadequacies in the current rig set-up with the associated instrumentation system. As such, the role of cavity modes on hot gas ingestion cannot be clarified based on the current set of data.

Thesis Supervisor: Choon S. Tan

Title: Senior Research Engineer of Aeronautics and Astronautics

Thesis Supervisor: Greg M. Laskowski

Title: Principal Engineer at GE Aviation

Acknowledgements

First and foremost I would like to express sincere gratitude to my advisor, Dr. Choon Tan. He has taught me how to learn and explore, how to be an "astronomer" in summarizing my observations, and how to "cut away the bad part of the apple" to find insightful data. I appreciate his understanding of my balance between being a GE employee and an MIT graduate student. I am perhaps most thankful for the fun and enjoyment he brought to my graduate experience.

I am also grateful for my GE Advisor Greg Laskowski who has provided extensive guidance and expert advice in support of my research efforts.

This research would not have been possible without the support of Kevin Kirtley at GE Power and Tim Stone at GE Aviation who kicked off the collaborative research effort between the GE businesses and MIT and brought me on board. I am thankful for the continued and active encouragement they have provided on this research topic.

A special thank you goes out to other GE colleagues who have supported my research. Eric Ruggiero, Pepe Palafox, and Rinaldo Miorini at GE Global Research and Ben Ding at GE Power have provided guidance in learning about the Hot Gas Ingestion Rig and abundant feedback and assistance along the way.

I would like to acknowledge Julius Montgomery at GE Aviation for supporting my efforts throughout the program and including me in his own turbine rim-seal research to expand my learnings.

Another colleague important to the success of this project is Peter Catalfamo who is working a complementary project in this field and has been a great collaborative resource for reflecting concepts and learnings.

I would also like to acknowledge General Electric for funding and sponsoring this research through a contract with MIT and the GE managers who have allowed me the opportunity to pursue this degree.

I am thankful to the staff and students in the MIT Gas Turbine Lab for providing a welcoming home during a significant portion of my time at MIT.

Finally, I thank my family for their support of my accomplishments: my parents who have encouraged me every step of the way and my husband Matthew who has given me energy and focus to complete this work.

Contents

List of Figures

List of Tables

Nomenclature

Subscripts

B	Buffer cavity
c	Coolant
r	Radial component
R	Rotor
S	Stator
T	Trench cavity
X	Axial component
Θ	Tangential component
∞	Freestream

Symbols

A	Neck area for Helmholtz resonator
AR	Aspect ratio
b	Seal radius
BR	Blowing ratio
c_w	Non-dimensional flow rate
D	Cavity depth
f_D	Deep cavity mode frequency
f_H	Helmholtz frequency
f_s	Shallow cavity mode frequency
G_c	Non-dimensional seal clearance
H	Shape factor
L	Neck length
M	Mach number
$\dot{m}$	Mass flow rate
n	Mode number
R	Turbine hub radius
Re_c	Reynolds number of cavity coolant flow

Re_θ	Reynolds number based on momentum thickness
Re_Ω	Rotational Reynolds number
s_c	Seal clearance
T	Temperature
U	Velocity
V	Cavity volume
W	Cavity width

Greek

a	Speed of sound
η	Sealing effectiveness
θ	Boundary layer thickness
μ	Fluid viscosity
ρ	Density
Φ	Flow coefficient
ω	Rotating speed of the rotor disk (RPM)

Abbreviations

HGIR	Hot Gas Ingestion Rig
NGV	Nozzle Guide Vane
PSD	Power Spectral Density

Chapter 1 Introduction

1.1 Background and Motivation

A turbine stage representative of a high performance gas turbine engine for aerospace propulsion and power generation consists of a stationary vane and rotor. The vane is mounted on a stationary disk while the rotor is on a rotating disk. There is a mechanical requirement that an axial gap exists between the stationary and rotor disks. This gap constitutes the wheelspace secondary flowpath illustrated in Figure 1.1.

A gas turbine operates following the Brayton cycle: air passes through the compressor which increases the gas pressure, the combustor increases the temperature of the gases, and the turbine extracts work from the hot gas to drive the compressor. The hot gas exiting the combustor and entering the first nozzle guide vane (NGV) can reach a temperature of 2500°F [1] and a pressure ratio of 50 with respect to the inlet [2]. The pressure distribution in the main gas flowpath and the secondary flow path is such that the hot gas in the main flowpath can be ingested into the wheelspace secondary flow path. To limit ingestion, cooling air is extracted from a compressor stage upstream in the gas turbine and this air is purged into the gaspath between the rotor and stator. The level of purge flow air is typically 3% of the gaspath mass flow rate [3]. The disk (stationary and rotating) material is typically a nickel-based alloy [4] with thermal limit below 2000°F [5], which is less than the main flowpath hot gas temperature. Therefore, this ingestion can have a negative impact on the life of the disk hardware because the materials typically cannot withstand the high temperature of main gas flowpath air.

The sealing effectiveness of a gas turbine is a measurement of how well the purge air reduces ingestion into the wheelspace cavity. To improve the sealing effectiveness of the purge flow between the rotor and stator, industrial turbines typically employ rim seals that provide a smaller clearance gap the purge air must travel through. When using multiple rim seals, the wheelspace is divided into individual regions. Figure 1.1 shows an example of a turbine with two radial rim seals and the nomenclature used for the different regions of the wheelspace: trench cavity for the region closest to the gaspath, inner wheelspace for the innermost region before the seals, and buffer cavity for the cavity between those two.

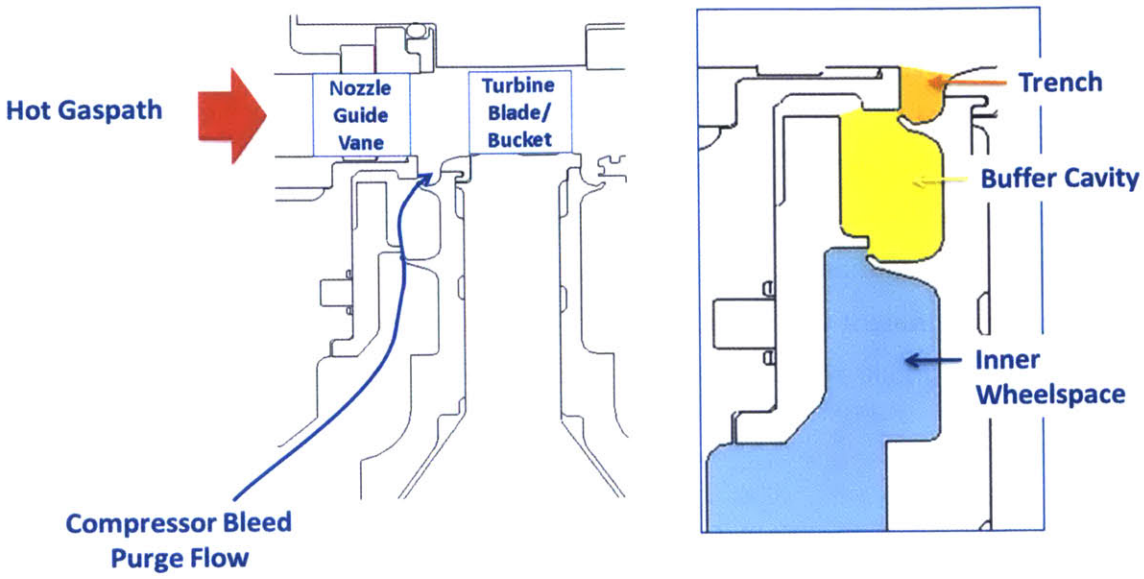

Figure 1.1: Secondary flow circuit and nomenclature for wheelspace between turbine disk and stator.

Although the purge air limits the ingestion levels, it has a negative impact on performance – the extracted cooling air does not contribute to work extracted by the turbine since it bypasses the combustor where energy is added to increase the temperature. Kerrebrock [1] quotes a 6.5% impact on turbine efficiency for 2.5% secondary flow extracted from the compressor. Therefore, the goal in designing wheelspace purge air is to minimize the amount of purge air extracted from the compressor while also reducing the amount of wheelspace ingestion. In addition, there is also a need to minimize the loss associated with introducing purge flow into the main gas flowpath; the loss mechanisms associated with this purge flow-main flow interaction have been assessed in a separate thesis by Zlatinov [6] on a quantitative basis. Zlatinov found that purge flow injected into the main gas flowpath at the hub between the rotor and stator disks contributed to increased stage losses. However, there has not been a detailed quantitative assessment of flow mechanisms in the wheelspace and any attending hot gas ingestion. While considerable research on hot gas ingestion yielding useful results has been conducted, the focus tends to be on *what* rim seal features improve sealing effectiveness rather than on *why* and *how* they do so. This thesis focuses on flow effects and processes in the wheelspace to address *why* and *how* rim seal features affect sealing. This is done by considering experimental data used in conjunction with computational study on a canonical cavity model to determine flow events and processes that drive ingestion.

1.2 Literature review

This section provides a concise description of the pertinent work on hot gas ingestion in the turbine rim-cavity seal flow. The first subsection focuses on the experimental aspect.

To assess the flow features present in turbine rim-cavity flow, examples of canonical cavity flow are also examined. More specifically, acoustic modes present in canonical cavity are used to provide insight into phenomena that affect hot gas ingestion in a gas turbine. A summary of cavity mode research on canonical configurations is presented in the second subsection.

1.2.1 Experimental Turbine Rigs for Determining Rim Sealing Effectiveness

Several rigs have been designed and constructed to experimentally assess the sealing effectiveness of turbine rim seals. The rigs typically employ a method of seeding purge flow with a gas such as CO_2 (carbon dioxide) and measuring the concentrations of that gas at different locations within the turbine-stator wheelspace to determine the level of ingestion for the experiment. The following constitutes a concise summary of the rigs that have been published to date.

An early rig at United Technologies Research Center (UTRC) was detailed by Daniels et al. [7]; the rig consisted of one stage and tested the effectiveness of a radial seal with an axial overlap. They concluded that reducing the radial gap has a larger effect on sealing effectiveness than that associated with increasing the axial overlap. Green et al. [8] carried out investigations on a rig at University of Sussex that consisted of a one-stage axial seal to assess the effect of rotor speed on sealing effectiveness of an axial seal. They found limited increase in ingestion rate with rotor speed, but indicated that the interaction of the rotor blades and upstream nozzle guide vanes (NGVs) is an important factor affecting ingestion. Further study on axial seals and the effect of the presence of rotor blades was analyzed by Bohn et al. [9] on a rig at Aachen and found that axial seals are more effective at preventing ingestion than a cavity without an axial seal for configurations with downstream rotor blades. Teramachi [10] at Ishikawajima-Harima Heavy Industries (IHI) analyzed radial rim seals with an axial overlap and found that the presence of rotor blades had a negative

impact on sealing effectiveness regardless of the degree of axial overlap. The configuration with overlap performed better than the configuration without overlap for this set of experiments.

More recently, rigs at University of Bath and Arizona State University (ASU) have been the predominant sources of investigation into sealing effectiveness in turbine rim cavities. Several papers have been published by Sangan et al [11] that detail experimental results on the Bath rig for axial and radial seals as well as single and double overlap seals in the study of externally and internally induced ingestion. The results show significant improvements in sealing effectiveness using radial seals with double-overlap. Balasubramanian [12] interrogated the ASU rig data to assess sealing effectiveness for double radial rim seals with axial overlap and found increasing ingestion levels for increasing gaspath flow rate and rotor speed. Zhou [13] looked at the rim cavity aspect ratio impact and found that larger depth to width aspect ratios contribute to more ingestion. One investigation of the ASU rig data by Roy [14] looked at instantaneous unsteady pressure measurements at the rim seal; he identified the effect of unsteady pressure disturbance caused by passing blades as well as another response attributed to an unsteady flow pattern rotating slightly below rotor speed. An example of these responses can be found in Figure 10 in Roy [14], where results are presented for several non-dimensional flowrates c_w – the ratio of purge mass flowrate through the seal to the product of the fluid viscosity μ and the seal radius b, i.e. $c_w = \frac{\dot{m}}{\mu b}$. However, there were no definitive conclusions on the role of unsteadiness on sealing effectiveness.

The Penn State 1.5 stage rig to study secondary flows in a gas turbine is described in detail by Barringer [15]. This rig will be used to assess the relationships between sealing effectiveness and turbine stage efficiency.

The data investigated in this thesis was acquired on a rig at the GE Global Research Center and detailed by Palafox [16]. This 1.5-stage Hot Gas Ingestion Rig (HGIR) measures gas concentrations to assess sealing effectiveness, as has been done in other rig experiments [7]- [15]. This data has been used to assess CFD models of the rig by Ding et al [17]. A capability assessment of the rig demonstrates that it can run at scaled engine conditions with acceptable data repeatability and measurement uncertainty. The differentiating factor for this rig is that it is scaled from an existing industry gas turbine and represents engine-matched conditions that allow results and learnings to be applied to other in-

dustrial turbines. It is also instrumented with several Kulite high response dynamic pressure transducers that enable the investigation of unsteady pressure phenomena not previously explored in other rigs. Details of the HGIR and instrumentation will be presented in Section 2.3 .

1.2.2 Cavity modes

For this investigation, Kulite measurements indicate the presence of cavity modes that influence an unsteady pressure response. Several studies have been performed on the presence of these mode types for canonical cavity geometries. These studies are concisely reviewed here and are later connected to the existence of such modes in HGIR data (Section 3.6) and analyses (Section 4.5).

1.2.2.1 Shallow Cavity

There have been many studies that investigate pressure fluctuations for flow over cavities, especially for the application of engineering devices (e.g. certain types of payload bays in transport aircraft). An early experimental study by Krishnamurty [18] at the California Institute of Technology used hot wire measurements to assess the response of the cavity pressure fluctuations for varying Mach numbers and cavity width-to-depth ratios. The experiments found dominant frequencies emerging from unsteady flow across the cavity and produced a set of data that correlate cavity geometry parameters to the frequency of the response. Similar experiments were also conducted by Plumblee et al. [19] and East [20]. In these experiments, fundamental responses in the cavity were identified. Several explanations and hypotheses have been put forward for the observed cavity flow response and behavior, but it is generally agreed that the instability in the shear layer forms upon separation of the boundary layer at the cavity lip. This instability results in a street of discrete vortices, each impinging on the opposite side of the cavity to generate a pressure disturbance that propagates in the cavity to generate a response. This response will be referred to as a "shallow cavity mode" (i.e. one of the natural cavity modes most receptive to the shear layer instability).

Rossiter [21] performed experiments to understand unsteady pressure fields for cargo bay applications in transport aircraft and developed an empirical formulation to deter-

mine the expected flow response in terms of resonant frequency given the cavity width and the Mach number of the flow over the cavity. This correlative relationship is given in Equation 1.1, where W is the cavity width, M is the Mach number of the flow across the cavity, a is the speed of sound, and n is the mode number. The first mode number starts at 1. The reduced frequency $\left(\frac{f_S W}{U_\infty}\right)$ is a function of Mach number and the mode number. Rossiter's expression in Equation 1.1 is in accord with data for Mach numbers ranging between 0.4 and 1.2.

$$\frac{f_S \cdot W}{M \cdot a} = \frac{n - 0.25}{M + \frac{1}{0.57}} \qquad \text{Equation 1.1}$$

Additional details will be provided in Section 3.6 on how this formulation is used to assess the rig data. Rossiter found that shallow cavity mode pressure fluctuations were present for cavity width-to-depth ratios greater than 4. For deeper cavities, a periodic standing-wave deep cavity mode was more prominent.

Heller et al. [22] provided modifications to Rossiter's formula for Mach numbers greater than 2, shown in Equation 1.2. Further findings supported the observation that the unsteady pressure fluctuations were more prominent for the laminar boundary layer than for turbulent.

$$\frac{f_S \cdot W}{M \cdot a} = \frac{n - 0.25}{\frac{M}{\left(1 + \frac{(\gamma - 1)M^2}{2}\right)^{1/2}} + \frac{1}{0.57}} \qquad \text{Equation 1.2}$$

Several studies have also been performed to evaluate the strategies by which shallow cavity response pressure oscillations could be mitigated. Heller, et al. [23] performed analytical and experimental assessments to identify the physical mechanisms that control occurrence of pressure fluctuations in shallow cavities. They found that a slanted wall at the cavity trailing edge helped to mitigate the pressure oscillations. Shaw [24] also found benefit in the ramped cavity trailing edge on flight test experiments. This type of configuration is shown in Figure 1.2.

Figure 1.2: Cavity configuration with trailing edge ramp as assessed by Shaw [24] for mitigating cavity response in pressure fluctuation.

Sarohia et al. [25] studied the effect of mass injection of flow at the base of the cavity and found that it had a stabilizing effect on the shear flow for some cavity configurations when the injected mass flow rate percentage was 5-15% of the freestream ρU_∞. However, some conditions led to enhanced cavity noise when mass injection was introduced. A similar study was performed by Sarno et al. [26], where flow was injected at the leading edge to suppress the response. Sarohia [27] also studied the ratio of shear layer thickness and momentum thickness to cavity width-to-depth ratios. He found that no vortex rollup, and therefore no response, occurred beyond a cavity width to momentum thickness ratio of 100. Gharib et al. [28] performed the same study but found the critical ratio to be 160.

Several reviews on shallow cavity flow research have been documented. Rockwell et al. [29] reviewed literature on flow past cavities and identified distinct categories of cavity oscillations: fluid-dynamic response which is caused by flow instability and fluid-resonance that manifests as standing waves in the cavity. Komerath et al. [30] performed a survey of available literature on flows over cavities including observed phenomena and methods for estimating their characteristics. Overall, existing literature has shown the following aspects associated with shallow cavity modes: (i) flows over shallow cavities are influenced by characteristics of the shear layer; (ii) there is evidence of modes co-existing; (iii) for a small ratio of cavity width to boundary layer thickness, the shear layer will "jump" over the cavity gap , meaning that a disturbance in the shear layer is not generated; (iv) frequency increases with Mach number; and (v) shear layer momentum thickness Reynolds number is important in instability.

Most recently, studies performed by Haigermoser et al. [31] at Polytechnic University of Turin using PIV to visualize the flow structure at low Mach numbers. They analyzed the behavior of vortex shedding for turbulent and laminar boundary layers to elucidate the three-dimensional characteristics in the form of a horseshoe vortex structure that are asso-

ciated with span-wise disturbances. The impingement of the vortex on the downstream cavity edge was found to be the primary mechanism for generating pressure disturbance. Figure 1.3 shows the recirculation identified in the streamlines as measured by the PIV in their experiment. Their findings showed larger pressure fluctuations for cavities with larger width-to-depth ratios.

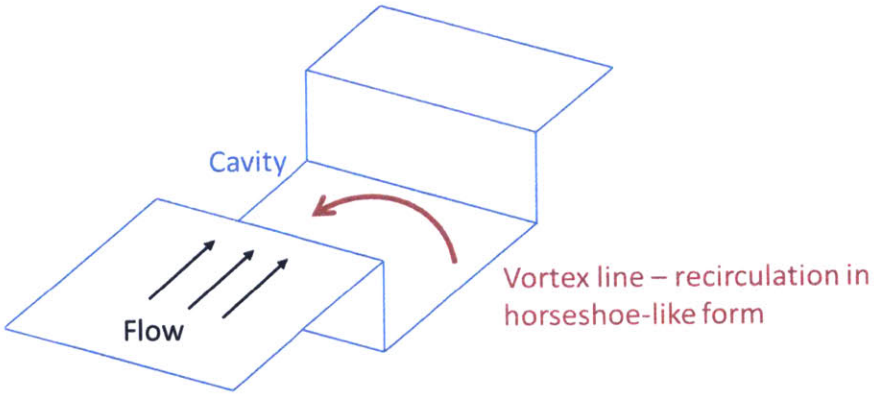

Figure 1.3: Sketch of horseshoe-like vortex in flow over a shallow cavity as identified by Haigermoser et al. [31].

In summary, existing studies have not provided any quantitative clarity on how mass flow injection into the cavity affects the shallow cavity mode. The effect of introducing a tangential component of the velocity in the primary flow has also not been analyzed and assessed. An objective of this thesis is to address these aspects of the flow (i.e. mass injection and tangential component of primary velocity) to determine the impact on the measured responses in the HGIR.

1.2.2.2 Helmholtz Resonance

The existence of the Helmholtz resonant mode in a turbine rim-cavity wheelspace system is also to be assessed. The excitation of a Helmholtz resonant mode occurs in a volume with a narrow neck that experiences an acoustic response initiated by unsteadiness in shear layer flow moving across the neck opening. Thus there exists a strong likelihood of turbine rim-cavity flow to exhibit a Helmholtz resonant response which would indirectly affect hot gas ingestion. The Helmholtz response is a well-known phenomenon described in many texts [32]. Figure 1.4 depicts a canonical Helmholtz resonator: the figure on the left is the resonator or oscillator with a container of air in volume V with an opening (i.e. neck) of cross-

sectional area A and length L; the figure on the right is the equivalent spring mass system with mass M and spring constant k.

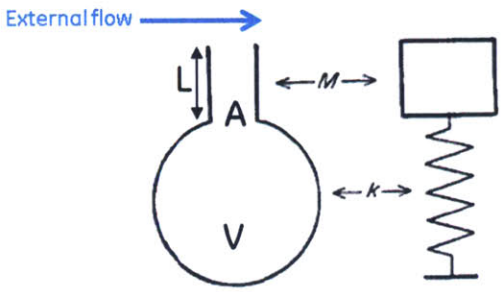

Figure 1.4: Canonical Helmholtz resonator and equivalent spring-mass system adopted from Alster [33].

The expression for the Helmholtz frequency is provided in Equation 1.3 where a is the speed of sound, A is the neck area (which would be the seal clearance in a representative turbine-rim-cavity configuration), V is the cavity volume, and L is the neck length.

$$f_H = \frac{a}{2\pi}\sqrt{\frac{A}{VL}} \qquad \text{Equation 1.3}$$

In a typical Helmholtz resonator, the fluid moving in and out of the neck entrains additional air inside and outside of the neck. This entrainment creates an effective neck length longer than the physical length (i.e. an end correction added to the neck length). This phenomenon is detailed by Ingard [34] with mass corrections provided for some configurations. Alster [33] also identified corrections to the classic formulation to account for variations in volume and neck type.

1.3 Problem Statement and Research Questions/Issues

The research questions that must be addressed are the following:

1. What flow drivers limit the sealing effectiveness of rim seals and why?
    a. What cavity acoustics are present in the rim seal cavity and what role do they play in driving ingestion?

i. What flow mechanisms affect the presence of cavity acoustics in the rim seal cavity?

b. What are the sources of flow unsteadiness and flow asymmetry internal and external to the wheelspace?

c. How are these sources, identified in (b) above, quantitatively linked to ingestion?

2. How can conclusions about flow phenomena be scaled to representative engine configurations?
3. How do ingestion levels affect heat load into the hardware?

This thesis focuses specifically on research questions 1a and 1b to identify what sources of unsteadiness and acoustics are present in the wheelspace cavity.

1.4 Thesis Contributions

A focus of this thesis is on assessing and interrogating experimental and computational data for the existence of modal resonance in the turbine-rim-cavity system and the impact on ingestion. Data is used in conjunction with CFD on canonical geometry to determine flow events and processes that drive ingestion. This investigation differs from others in that the focus is on identifying acoustic modal response and flow processes that could drive hot gas ingestion in a turbine engine.

The key findings consist of:

1. Cavity modes exist in the turbine rim-cavity wheelspace of a gas turbine. This is supported by experimental data on a test rig with turbine stage and wheelspace configuration representative of that on a gas turbine engine. Cavity modes identified in this work are the Shallow Cavity mode and Helmholtz resonance.
2. Computational modeling of canonical cavity flow suggests that increasing the mass flow injection into the cavity (more precisely, increasing the ratio of injected mass flow rate to the main flow mass flow rate) reduces the amplitude of the response of Shallow Cavity modes. This is in agreement with data from the HGIR for Shallow Cavity Mode 1, but in contrast to data from HGIR for Shallow Cavity Mode 2 which shows trench cavity modal response increasing with purge flow level.

3. Computational modeling of canonical cavity flow suggests that increasing the primary flow tangential to axial velocity ratio mitigates the shallow cavity mode response, exhibiting a cut-off point where the response is no longer present for flow angle beyond 45°. Again this observation is in contrast to the HGIR data that show the modal response is present with a flow angle greater than 45°.
4. The implication of 2 and 3 in the computational assessment is that the purge flow and main gas flowpath swirl angle in a gas turbine provide a stabilizing effect on the cavity modal response.
5. Experimental requirements to capture the effects of cavity modes are identified along with inadequacies in the current rig set-up with the associated instrumentation system.
6. Because of 5, the role of cavity modes on hot gas ingestion cannot be clarified based on the current set of data.

1.5 Central Theme and Organization of Thesis

The underlying theme of this thesis is on the presence of cavity modes in the stator/rotor rim-seal cavity wheelspace system. Evidence of several cavity modes identified in the Hot Gas Ingestion Rig (HGIR) at GE Global Research Center is presented and assessed against results obtained from analysis of simple cavity configurations. The modes that will be addressed are Helmholtz, Shallow Cavity, and Deep Cavity responses, and they will be examined across several rig configurations. A computational assessment of one of these modes (Shallow Cavity) and the impact of rig conditions (purge flow and flowpath swirl angle) on the modal response will also be assessed.

This thesis is organized as follows: First, the research framework is presented in Chapter 2 . This chapter includes experimental attributes of the Hot Gas Ingestion Rig, the computational framework that serves to complement the experimental data, and the synergism between the experimental data and computational results. Chapter 3 evaluates the HGIR Kulite data, including comparisons to canonical responses of Shallow Cavity and Helmholtz resonance to formulate the hypothesis of the presence of these modes. The results support the presence of these modes. These comparisons confirm the hypothesis that the Shallow Cavity and Helmholtz mode responses are present in the turbine rim-cavity. A

more in-depth assessment into the effects of industrial gas turbine design parameters on the Shallow Cavity Mode response via computational modeling is presented in Chapter 4 . The hypothesis on the existence of Shallow Cavity mode is assessed using a canonical CFD model of a rectangular cavity. The assessment of the computational results from the canonical cavity model provides further insight into the Shallow Cavity mode and further supports the presence of this mode in a gas turbine configuration. Additional observations are also made to suggest the plausibility of suppressing undesirable modes (i.e. those impacting hot gas ingestion unfavorably) during gas turbine operation. Chapter 5 synthesizes the findings from the experimental and computational results. The key findings of the thesis are presented in the Summary along with recommendations for future work.

Chapter 2 Research Framework and Approach

This chapter describes the experimental and computational approach to assessing flow features in the turbine rim-seal cavity. First, details on non-dimensionalizing the design and operating parameters are presented. Next, the characterizing parameters of the turbine rim-cavity wheelspace system are identified for the rig configurations studied in this thesis. Details of the Hot Gas Ingestion Rig are presented along with an assessment of the quality of data obtained from the rig experiments. Then, the characterizing parameters of canonical cavity flow are presented. Finally, the framework for computational assessment of canonical cavity configurations is described to provide the synergism between the computational and experimental results.

2.1 Non-Dimensionalization of Parameters in a Turbine Rim-Cavity Wheelspace System

When processing high-frequency content, the Welch power spectrum is used. With this method, periodograms of the signal are divided into several windows and averaged. This method reduces variance in the signal to bring out responses in the data. The goal is to use the largest number of windows possible to reduce variance while still keeping enough resolution in the data to capture relevant lower frequencies [35]. For the 100 kHz signal, a window size of 2^{10} samples (0.01 seconds) was used. This window size breaks the signal into just under 100 windows for averaging and maintains enough resolution to capture frequencies as low as 200 Hz.

Frequencies obtained from post-processing Kulite data are normalized to the blade passing frequency in this thesis. Normalizing the data with this method enables clear discernibility between the pressure disturbances caused by the presence of airfoils (i.e. blades) in the main gas flowpath and those caused by other sources.

2.2 Characterization of Flow in a Turbine Rim-Cavity Wheelspace System

In this section, the key parameters that describe the geometric and aerothermal characteristics of the turbine rim-cavity wheelspace system are presented. These parameters are compared between the turbine rim-cavity configuration on the HGIR and computational model for the canonical cavity flow configuration. Figure 2.1 shows the geometrical features referenced in this section.

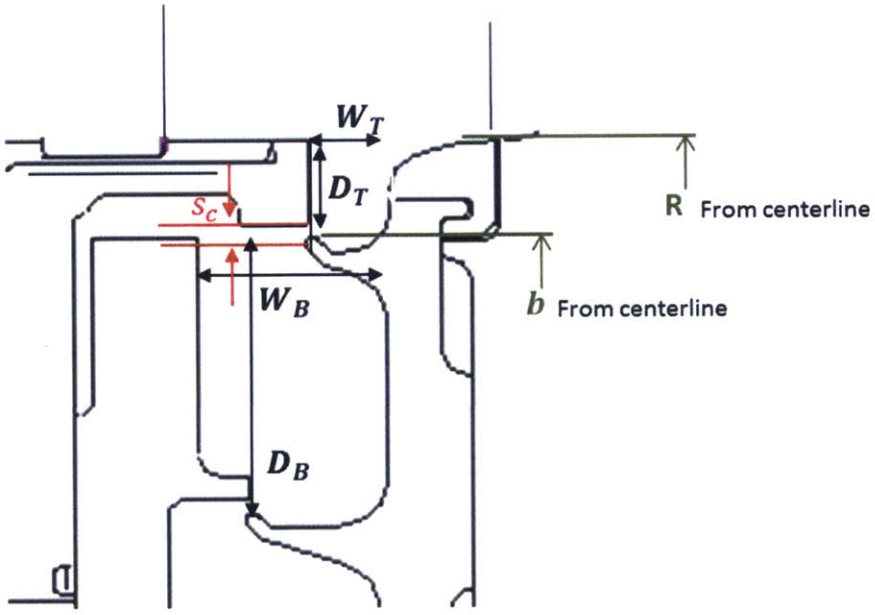

Figure 2.1: Depiction of parameters used to characterize the turbine rim-cavity wheelspace system.

2.2.1 Geometry Characterization

Important considerations for characterizing the geometry of a turbine rim-cavity wheelspace system are the aspect ratio of the trench cavity, the aspect ratio of the buffer cavity, and the ratio of the seal height to the seal radius from the engine centerline.

Equation 2.1 and Equation 2.2 provide the equations for the aspect ratio of the trench and buffer cavity, respectively, where D is the depth of the cavity and W is the width of the cavity.

$$AR_T = \frac{D_T}{W_T} \qquad \text{Equation 2.1}$$

$$AR_B = \frac{D_B}{W_B} \qquad \text{Equation 2.2}$$

Equation 2.3 gives the expression for the non-dimensional seal clearance, where s_c is the seal clearance gap height and b is the radial distance from the seal to the centerline.

$$G_c = \frac{s_c}{b} \qquad \text{Equation 2.3}$$

2.2.2 Aerothermal Characterization

A key parameter in the wheelspace configuration is the rotational Reynolds number, which is the ratio of the inertial force from the rotating disk to the viscous force of the fluid. The rotational Reynolds number is defined in Equation 2.4 , where ω is the rotational wheel speed of the turbine disk in radians per second, R is the distance from the engine centerline to the turbine blade hub, and ρ_∞ and μ_∞ are the density and dynamic viscosity of the main gas flowpath respectively.

$$Re_\Omega = \frac{\rho_\infty \omega R^2}{\mu_\infty} \qquad \text{Equation 2.4}$$

The Reynolds number of the purge flow injected into the cavity, defined by Equation 2.5, is also a characterizing parameter. In Equation 2.5, D is the depth of the cavity, U_c is the velocity of the injected gas based on the mass flowrate and cavity area, and ρ_c and μ_c are the density and dynamic viscosity of the injected flow respectively.

$$Re_c = \frac{\rho_c U_c D}{\mu_c} \qquad \text{Equation 2.5}$$

The flow coefficient that characterizes the purge flow is defined in Equation 2.6, where U_c is the velocity of the purge flow coolant gas, b is the radius of the rim seal as

measured from the centerline, and ω is the rotating speed of the rotor disk. It is similar to the Rossby number, quantifying the ratio between the inertial and Coriolis forces.

$$\Phi = \frac{U_c}{\omega b} \qquad \text{Equation 2.6}$$

In addition, the following non-dimnensional parameters are of relevance in characterizing the interaction between the cavity flow and main flow:

$\frac{T_c}{T_\infty}$	Ratio of gas temperature
$\frac{U_c}{U_\infty}$	Ratio of fluid velocity
$\frac{\dot{m}_c}{\dot{m}_\infty}$	Ratio of mass flow
$\frac{U_{\infty\Theta}}{U_{\infty x}}$	Ratio of tangential to axial components of primary flow
$\frac{U_{cr}}{U_{\infty x}}$	Ratio of radial component of purge flow to axial component of primary flow
$\frac{U_{c\Theta}}{U_{\infty x}}$	Ratio of tangential component of purge flow to axial component of primary flow
$\frac{\Delta p/\rho_\infty U^2{}_{\infty\theta}}{span/R}$	Streamline curvature effect
Re_∞	Reynolds number of primary flow

2.3 Experimental Aspects – GE GRC HGIR

The Hot Gas Ingestion Rig at GE Global Research [16] was developed to assess what sets acceptable levels of ingestion as well as the required attributes of CFD tools to calculate sealing effectiveness for a representative engine. The rig uses CO_2-seeded purge flow and CO_2 sensors in the wheelspace to measure concentrations of ingested flowpath air and the results are compared to those of reduced-sector CFD models. The wheelspace geometry design is representative of a gas turbine engine for power generation. A schematic of the rig and a picture of the HGIR facility are shown in Figure 2.2 and Figure 2.3, respectively.

Kulite data from the trench and buffer cavity are post-processed using the following strategy:

1. Interrogate HGIR results from 1 test configuration at multiple wheel speeds and purge flow levels
2. Formulate hypotheses on what causes the data to look the way it does
3. Assess hypotheses using data from additional rig configurations
4. Propose necessary experiments for identifying hypothesized flow drivers
    a. Implement experiments on HGIR at GE GRC
5. Complement data with CFD data for identifying flow features that could have controlling influences on ingestion
6. Develop general conclusions about phenomena that are generic to all wheelspace configurations

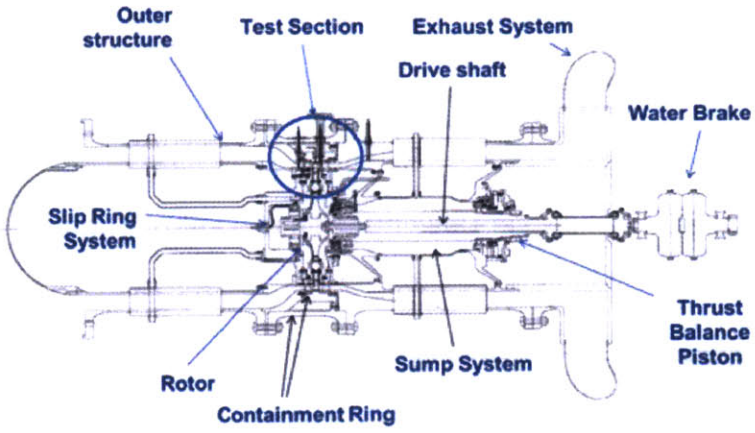

Figure 2.2: Global view of HGIR Test Facility with main auxiliary components. Palafox [16]

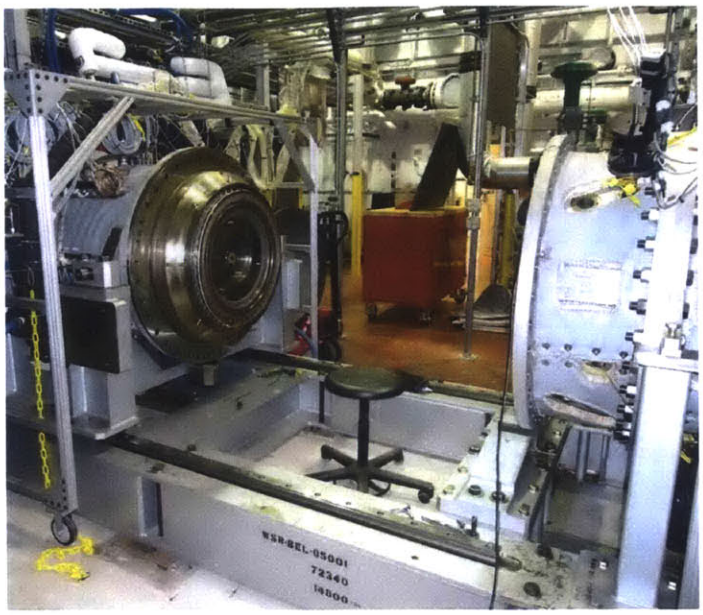

Figure 2.3: HGIR facility with exposed stator. Palafox [16]

2.3.1 HGIR Data Quality

The HGIR is instrumented with the following probes that would serve to provide selected quantitative aspects of the rim seal flow field:

1. Static pressure taps aft of the NGV trailing edge and along the stator disk wall
2. CO_2 ports along the stator disk wall
3. Kulites on the stator disk wall in the trench and buffer cavities, and on the rotor disk wall in the buffer cavity

Palafox et al. [16] summarizes the uncertainties for these key parameters measured on the rig and also provides typical results for the rig operating condition. In this thesis, an assessment of the data quality and measurement capabilities is addressed.

The static pressure taps provided data comparable to expected results for all configurations investigated. Aft of the NGV trailing edge, static pressure taps were located at 10 locations across a single vane passage and provided sufficient resolution to resolve the circumferential pressure variation at two axial locations behind the trailing edge. The locations of these pressure taps are indicated in Figure 2.4 and a rolled-out display of all instrumentation is provided in Figure 2.5.

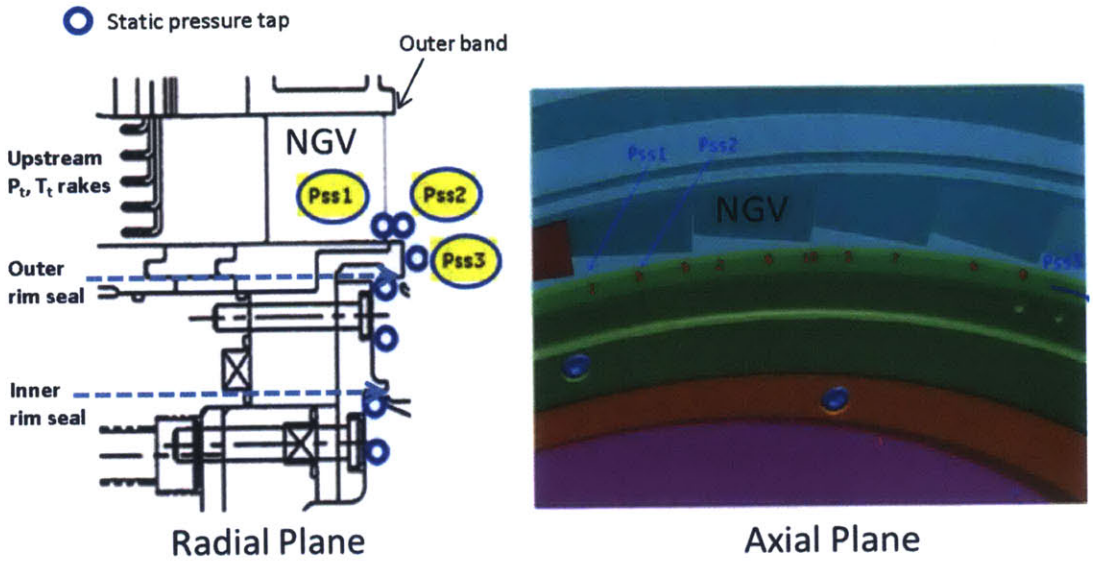

Figure 2.4: Static pressure tap locations on HGIR stator surface. Pss1-Pss3 indicate the static pressure taps located behind the NGV TE and in the trench cavity and are currently used for assessing the circumferential pressure variation. Palafox [16]

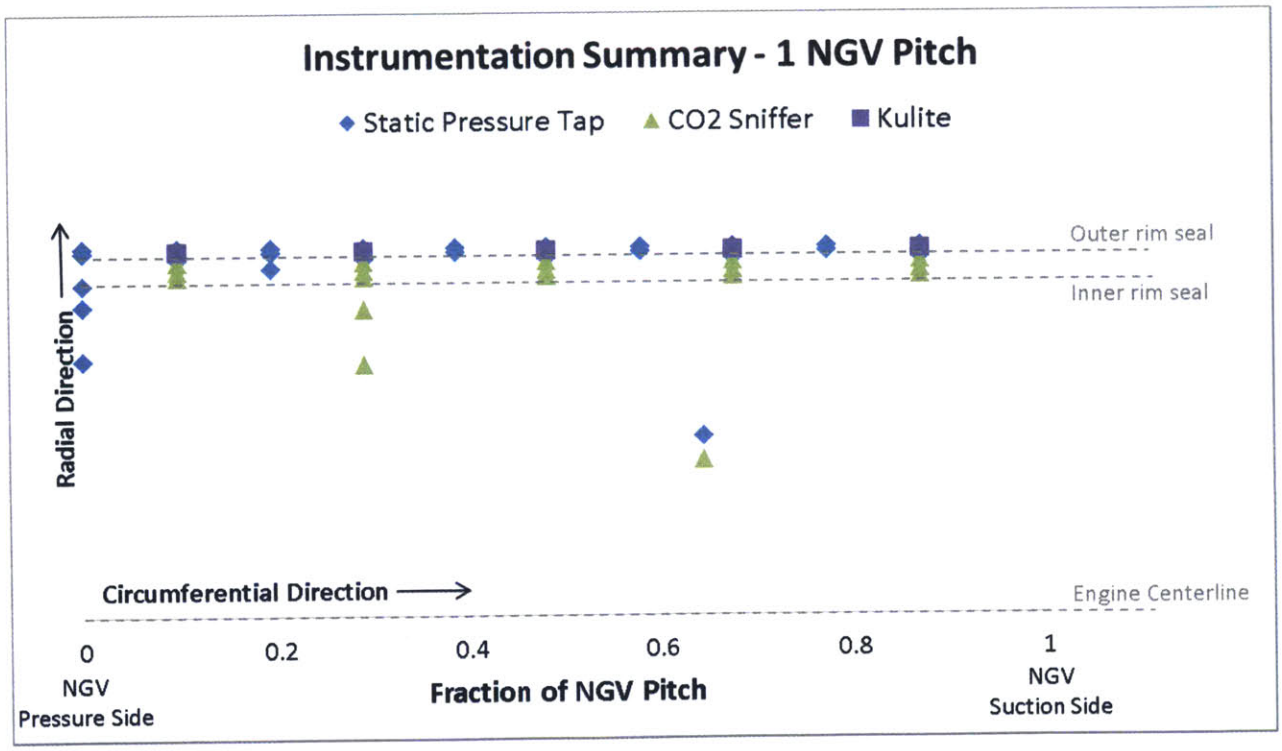

Figure 2.5: Summary of instrumentation at radial and circumferential locations with respect to engine centerline and NGV trailing edge.

The CO_2 detection system can only provide sufficient data to quantify the time-averaged ingestion levels for different configurations. The location of these CO_2 sniffers is shown in Figure 2.6. The limitation of these measurements is that they are unable to capture high frequency response changes in ingestion levels. For the study of cavity resonant mode impact on ingestion, it is imperative to capture time-resolved ingestion levels that can be assessed against the unsteady pressure fluctuations imparted by the resonance. Because the CO_2 sniffers cannot provide that level of resolution, it is difficult to assess whether bulk ingestion level changes may be due to changes in unsteady pressure fluctuations induced by resonant phenomena.

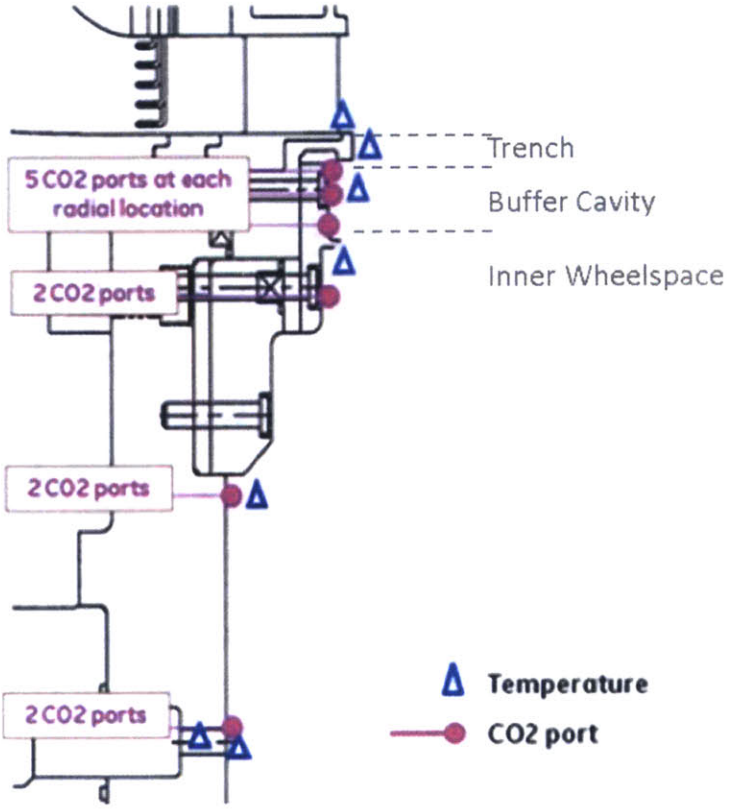

Figure 2.6: CO_2 sniffer port locations on HGIR stator surface. A total of 15 ports are located in the buffer cavity and 6 ports are located in the inner wheelspace. Palafox [16]

Pressure measurements from the Kulites were instrumental in the investigation of pressure disturbances and unsteadiness in the rim seal. A detailed assessment of the pressure disturbances present in the rim cavity and the sources of those disturbances has not been carried out on other rig studies described in Section 1.2.1 , but will be addressed in

this thesis. The location of these Kulites on the rotor surface is shown in Figure 2.7 and all Kulite locations are detailed further in Section 3.1 . The Kulites were sampled at 100 kHz for 1 second intervals. These measurements were then post-processed to identify any frequencies caused by fluid-dynamic and acoustic effects at the rim seal. The Kulites on this rig had several limitations that affected assessment, post-processing, and physical interpretation of the data. On average, 2/3 of the Kulites were non-functioning – these Kulites provided data that was too noisy to process or did not provide any data. Though investigations suggest that the high gas temperatures of the rig could be responsible for the Kulite failures, experiments with low rig temperatures also produced non-functioning Kulites.

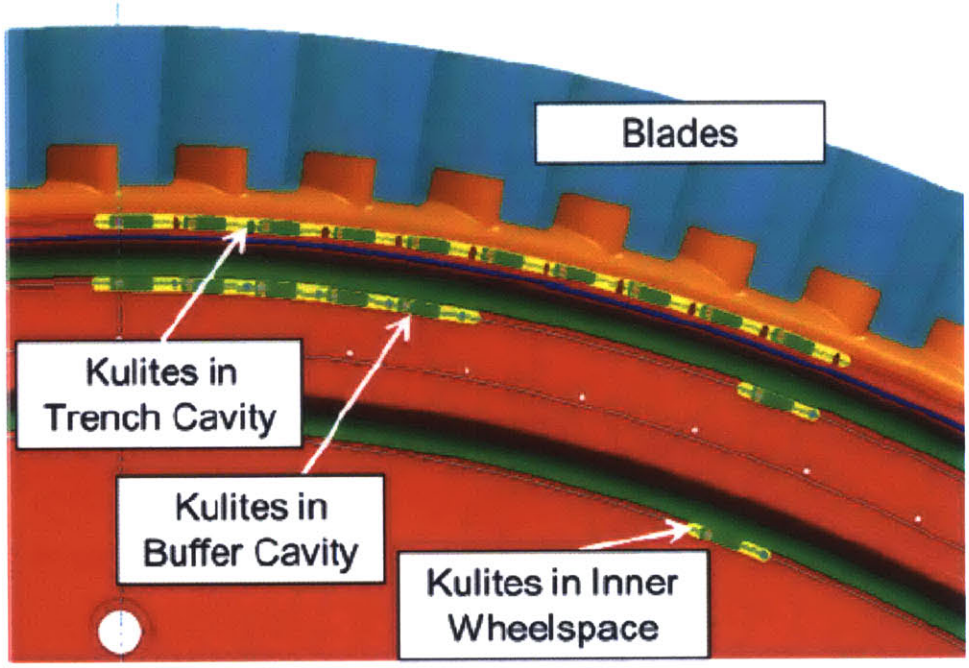

Figure 2.7: Kulite locations on HGIR rotor surface. There are a total of 30 dynamic Kulites in the trench cavity, 5 dynamic Kulites in the buffer cavity, and 2 static Kulites in the inner wheelspace. 10 of the Kulites in the trench cavity are located on the stator side of the trench cavity at the same radial location. Palafox [16]

For the Kulites that did provide data without failure, several frequencies of non-physical origin were identified. To understand what frequencies may be non-physical, data was collected from the Kulites by turning on the Data Acquisition System (DAQ) when the rig was not running. No other component of the rig was active during this data collection. However, Figure 2.8 shows that several frequencies were recorded by the Kulites for this test. These frequencies are non-physical and do not correspond to any fluid-dynamic or

acoustic effects in the rig, but do appear when processing data from the rig under operating conditions.

At the time of this thesis, the source of these frequencies is not understood. However, understanding what non-physical frequencies are present is critical for assessing the data. Therefore, available non-running rig data was used when possible to rule out frequencies during the assessment on the existence of cavity modes. For optimum assessment of the unsteady pressure field, it is recommended that the sources of non-physical frequencies on the HGIR Kulites be identified and addressed to clarify the results collected by the Kulite measurements.

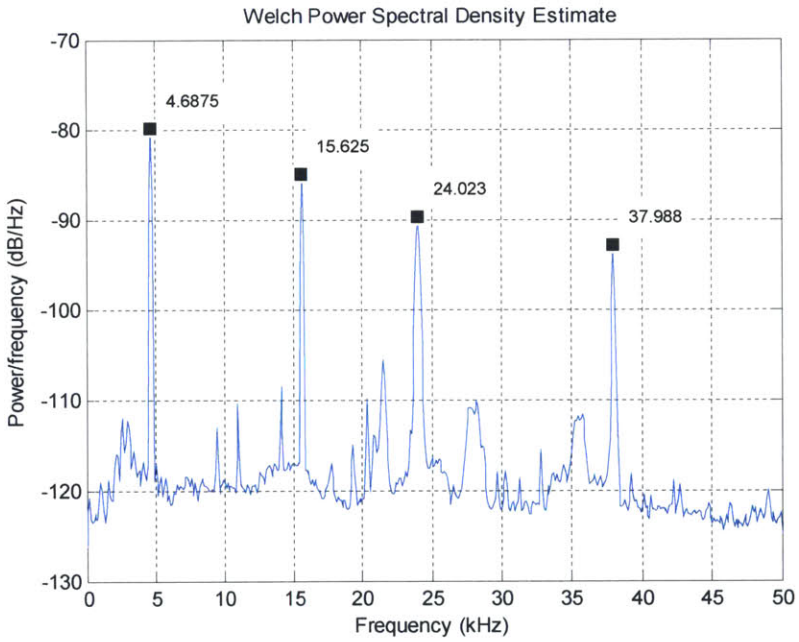

Figure 2.8: Erroneous frequencies in PSD from measured Kulite data sample for non-running rig. 4 frequencies of non-physical origin are identified at 4.7, 15.6, 24.0, and 38.0 kHz.

2.4 Characterization of Canonical Cavity Flow

In this section, the key parameters that describe the geometric and aerothermal characteristics of the canonical cavity are presented. These parameters are then compared to the turbine rim-cavity configuration on the HGIR. Figure 2.9 shows the key geometric parameters for a generic canonical rectangular cavity flow configuration.

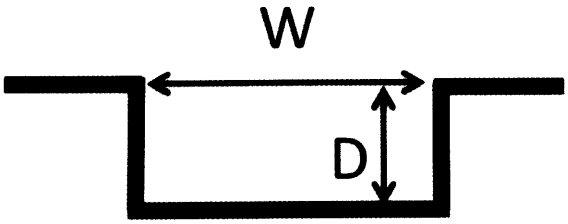

Figure 2.9: Depiction of parameters used to characterize a canonical rectangular cavity.

2.4.1 Geometry Characterization

Gharib et al. [28] identified the aspect ratio of the cavity to be an important factor in the shallow cavity response. The aspect ratio of the cavity is defined by Equation 2.7, where D is the depth of the cavity and W is the width of the cavity.

$$AR = \frac{D}{W} \qquad \text{Equation 2.7}$$

2.4.2 Aerothermal Characterization

The approach boundary layer thickness is an important parameter in the shallow cavity response, as identified by Sarohia [27]. Therefore, the Reynolds number based on the momentum boundary layer thickness is a non-dimensional characterizing parameter in the canonical configuration. It is defined in Equation 2.8, where θ is the momentum boundary layer thickness, $U_\infty$is the velocity in the main gas flowpath, and ρ_∞ and μ_∞ are the density and dynamic viscosity of the main gas flow respectively.

$$Re_\theta = \frac{\rho_\infty U_\infty \theta}{\mu_\infty} \qquad \text{Equation 2.8}$$

The Reynolds number of the flow injected into the cavity (the purge flow in the turbine rig configuration), defined by Equation 2.9, is also a characterizing parameter. In Equation 2.9, D is the depth of the cavity, $U_c$is the velocity of the injected gas based on the

mass flowrate and cavity area, and ρ_c and μ_c are the density and dynamic viscosity of the injected flow respectively.

$$Re_c = \frac{\rho_c U_c D}{\mu_c} \qquad \text{Equation 2.9}$$

The blowing ratio, defined by Equation 2.10, is another important flow parameter in the interaction of injected flow and main gas flow. In this formulation, ρ_c is the density of the injected flow, ρ_∞ is the density of the main flowpath, U_c is the velocity of the injected flow, and U_∞ is the velocity of the main flowpath.

$$BR = \frac{\rho_c U_c}{\rho_\infty U_\infty} \qquad \text{Equation 2.10}$$

2.5 Computational Aspects – Canonical Configurations

To complement the investigation of wheelspace cavity modes hypothesized from data acquired on the HGIR, an evaluation on the fundamental aspects of the cavity modes is performed. The hypothesis on the presence of Shallow Cavity mode is developed by comparing data from the HGIR to calculations of modes for canonical cavity configurations, as described in the following. However, the HGIR cavities exhibit complexities not present in the canonical configurations. These complexities include, but are not limited to: mass injection via purge flow, axisymmetric geometry, swirled velocity component in the main gas flowpath, non-rectangular geometrical features of the cavity, and NGV/blade rows located upstream and downstream of the cavity.

Basic canonical cavities referred to in published literature are often rectangular-shaped configurations that lack the previously mentioned features typically found in a turbine rim-cavity. To break down the effects of this additional complexity, CFD methods are used to assess and identify modal unsteadiness in canonical geometry and compared against publicly available data. Additional assessments are carried out to incorporate those features unique to gas turbines, such as the purge flow and the swirling flow environment of the main flowpath. Specifically, assessments are carried out on the role of the tangential velocity component in the gas flowpath and the effects of mass flow injection through the

cavity. These features are assessed individually to examine their effect on the cavity mode frequency and amplitude, as described in Chapter 4 .

2.6 Connection to Representative Gas Turbine Engine Operating Environments

Table 2.1 gives the quantitative value of the non-dimensional parameters characterizing the geometry and flow dynamics of the HGIR and how they contrast with those parameters used in the CFD assessment of the canonical cavity flow configuration. The canonical CFD model refers to the computed flow in a canonical rectangular cavity such as that shown in Figure 2.9.

The rotational Reynolds number, Re_{Ω}, and the Mach number at the trailing edge of the NGV on the HGIR are representative of typical engine operation. The Mach number of the flow in the main gas flowpath of the HGIR is transonic. The Mach number of the main outer flow in the canonical geometry is 0.75 and is used for the CFD studies. The momentum thickness Reynolds number, Re_{θ}, is the same order of magnitude between the HGIR and canonical configuration.

Three different coolant flow levels were tested on the HGIR. These levels were also assessed using the canonical CFD model. For a consistent comparison between the gas turbine and canonical geometry, the injected mass flow in the CFD model was chosen such that the coolant flow Mach number was matched to the HGIR values. For the three purge flow levels investigated, the blowing ratio is compared between the HGIR and CFD model. The blowing ratio for the three levels is comparable between the two cases. There are two primary configurations examined in the HGIR. Three cavity depths are examined for the canonical CFD studies. The deepest cavity is set so that it represents the same aspect ratio as one of the HGIR configurations.

Based on the non-dimensional parameters of the HGIR versus the CFD model, the computed flows for the canonical cavity are expected to provide sufficient representation of the flow characteristics to drive an understanding of the fundamental flow behavior in the HGIR cavity modes.

	HGIR	Canonical CFD
M_∞	1.13	0.75
Re_θ	2437	1192
M_c	0.30, 0.46, 0.66	0.30, 0.46, 0.66
Re_c	5040, 7804, 11121	10031, 15381, 22089
BR	0.40, 0.55, 0.78	0.35, 0.61, 0.88
AR_t	1.46, 2.92	0.2, 0.5, 1.44

Table 2.1: Comparison of non-dimensional parameters between the HGIR and the canonical cavity CFD studies.

2.7 Synergism in Experiments and Computations

The framework of approach thus consists of both the experimental assessment of the HGIR data and the computational assessment of a canonical cavity flow configuration. This is then followed by synthesis of the results to infer upon the physical rationale for why the data looks the way it does as well as the key controlling aspects of flow that would impact ingestion.

2.8 Summary

To summarize, the overall research framework consists of post-processing and interrogating the data on the HGIR complemented by computational assessment of flows in canonical cavity configurations. The perceived inadequacy in the current instrumentation setup on the HGIR is noted, and suggestions for mitigating the inadequacy are put forward for future experiments. Nevertheless, the data acquired to date on the HGIR has technical utility value as the results to be described and presented will show.

Chapter 3 Experimental Assessment of Cavity Modes (HGIR Testing)

In this chapter, Kulite data on the Hot Gas Ingestion Rig (HGIR) is interrogated and assessed to determine the existence of cavity modes alluded to in Chapter 2 . Kulite data responses are compared for varying probe locations within the cavity, rotor speeds (i.e. Re_Ω), and purge flow levels (i.e. $\frac{\dot{m}_c}{\dot{m}_\infty}$). The responses are then analyzed for the presence of characteristic features that reflect the existence of Shallow Cavity mode and Helmholtz resonance in the HGIR rim-seal cavity system.

3.1 Kulite Instrumentation and Results

Several rim-cavity wheelspace configurations for a specific turbine stage have been tested on the HGIR at the GE Global Research Center to investigate the effects of configuration variation on purge flow effectiveness in the forward wheelspace. For these experiments, high-speed Kulite pressure transducers were located in the trench and buffer cavities. The results obtained from this instrumentation were interrogated to determine the pressure field in the wheelspace, followed by hypothesizing what set it. Cavity location, rotor speed (i.e. Re_Ω), and purge flow level (i.e. $\frac{\dot{m}_c}{\dot{m}_\infty}$) were three factors investigated and assessed.

The Kulite data from these configurations was also interrogated to determine what cavity modes may be present. From this effort, it was found that plausible sources of pressure unsteadiness in the forward wheelspace are a Helmholtz resonance in the buffer cavity and a Shallow Cavity response in the trench cavity.

3.2 Effect of Probe Location on Response

Distinct responses in the Kulite data were observed; thus, it is important to assess what impacts these responses have in order to identify the source and why the data appears the way it does. The data interrogation begins by assessing the difference in frequency content and magnitude for Kulites at different probe locations within the cavities.

The first set of experimental data available from the HGIR testing will be referred to as Configuration 1. The following data is for a low purge flow level (0.8% of the gaspath mass flow) and rotational Reynolds number (defined in Equation 2.4) of 3.06E6. It is hypothesized that there is attenuation of the unsteady pressure response associated with the passing of the airfoils in the buffer and wheelspace cavities and that other unsteady pressure responses due to cavity modes will be present.

For this configuration, in addition to the trench and buffer cavity Kulites, a static Kulite located on the inner wheelspace of the rotor was sampled at 100 kHz to determine the differences in unsteady pressure distribution at different radial locations. Figure 3.1 shows the locations of the pressure tap and Kulites.

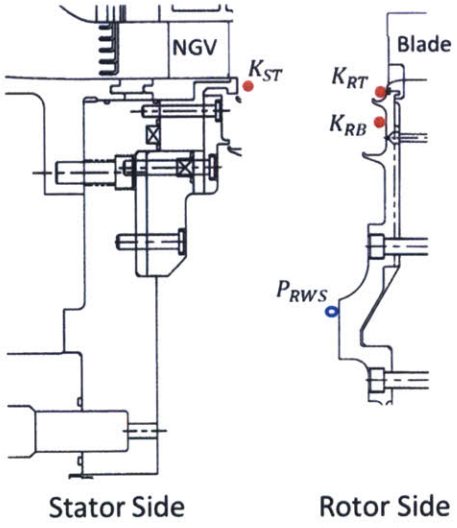

Figure 3.1: Labels and positions of Kulites in the Trench cavity on the Rotor (K_{RT}) and Stator side (K_{ST}), Kulites in the Buffer cavity on the Rotor (K_{RB}), and static Pressure taps on the Rotor in the Inner Wheelspace (P_{RWS}).

Figure 3.2 and Figure 3.3 present the power spectrums extracted from post-processing the pressure data output from stator and rotor Kulites located in the trench cavity. The results are normalized by the blade passing frequency at the rig rotating speed. A representative data set was taken for each location. The power spectrum for the Kulite on a non-running rig is overlaid in each figure to identify the erroneous non-physical frequencies that may be present and should be ignored. For the Kulite on the stator surface (K_{ST}), an erroneous frequency due to signal noise is seen at 0.488 of blade passing frequency. The

frequency at approximately 1 is the blade passing frequency. There are also responses at 0.783 and 4.82 of blade passing frequency.

These responses can be compared to those measured by the Kulite on the rotor surface (K_{RT}). For the rotor surface Kulite, a response due to the passing NGVs is expected at 0.5 (and harmonics at 1, 1.5, etc.). The response at this expected frequency is convoluted with the non-physical response identified at 0.488. The responses at 0.783 and 4.82 are also present on the rotor side with similar magnitudes, and an additional response is measured at 0.203. The source of the 0.783 frequency is hypothesized to be a Shallow Cavity mode discussed in Section 3.6.2 . The 0.203 is thought to be a Helmholtz resonance discussed in Section 3.5.2 . The source of the 4.82 frequency cannot yet be ascertained.

Figure 3.4 and Figure 3.5 present the power spectrum of the Kulite data in the buffer (K_{RB}) and wheelspace (P_{RWS}) cavities on the rotor surface. In the buffer cavity, similar responses are present that were measured in the trench cavity. The response at 0.203 has a smaller magnitude in the buffer cavity and is not present in the wheelspace. The effect on the response due to the NGV is difficult to discern from the erroneous response. The harmonic at ~1.0 is hardly discernable in the buffer or wheelspace cavities. The buffer cavity Kulite data may not have been sensitive enough to pick up the response or the harmonic is attenuated across the rim seal. The 0.738 and 4.82 responses have similar magnitude in the both the buffer and wheelspace cavities.

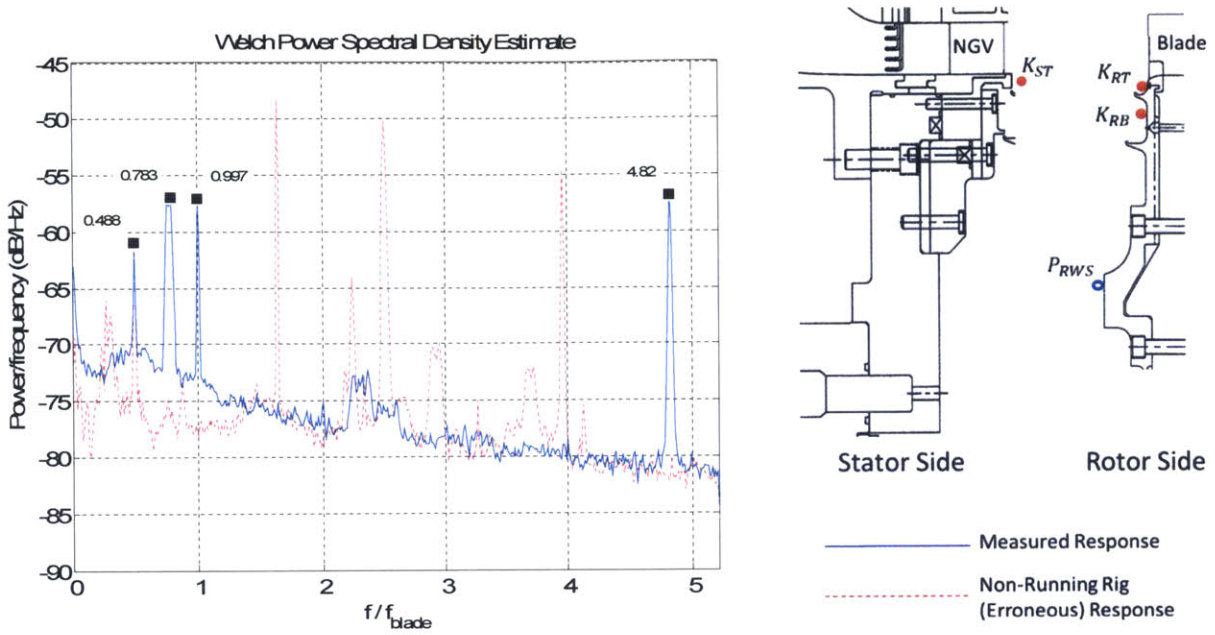

Figure 3.2: PSD for K_{ST} in Figure 3.1 – Kulite in trench cavity on stator surface for Configuration 1. Responses are normalized to the blade passing frequency.

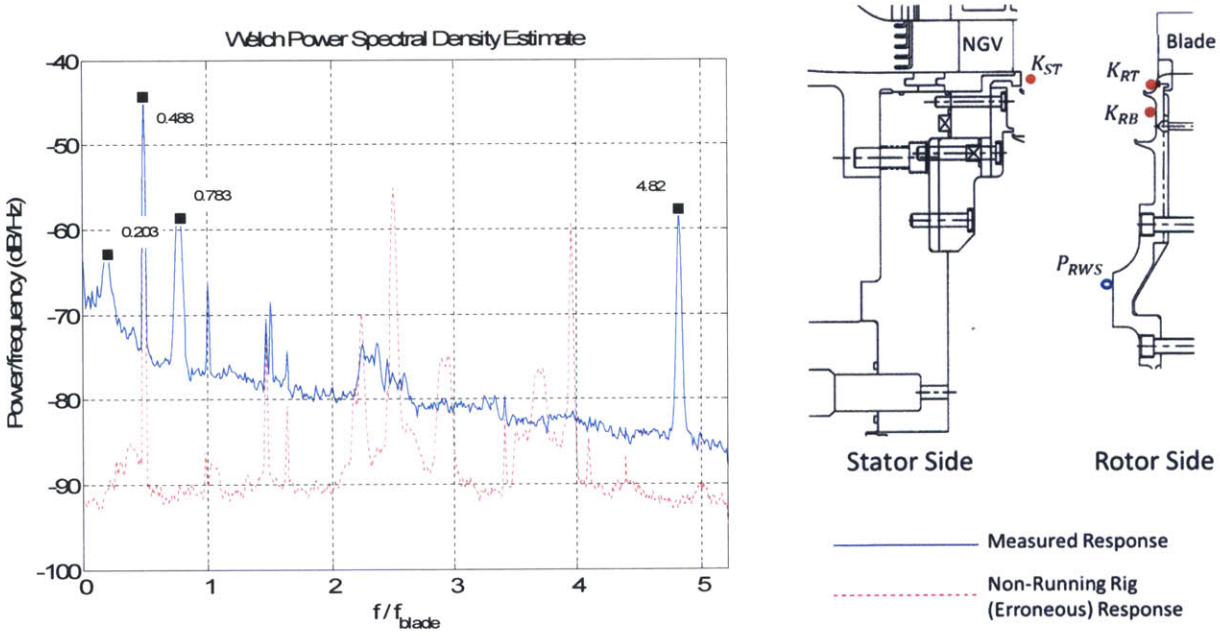

Figure 3.3: PSD for K_{RT} – Kulite in trench cavity on rotor surface for Configuration 1. Responses are normalized to the blade passing frequency. An erroneous data point is present at 0.488.

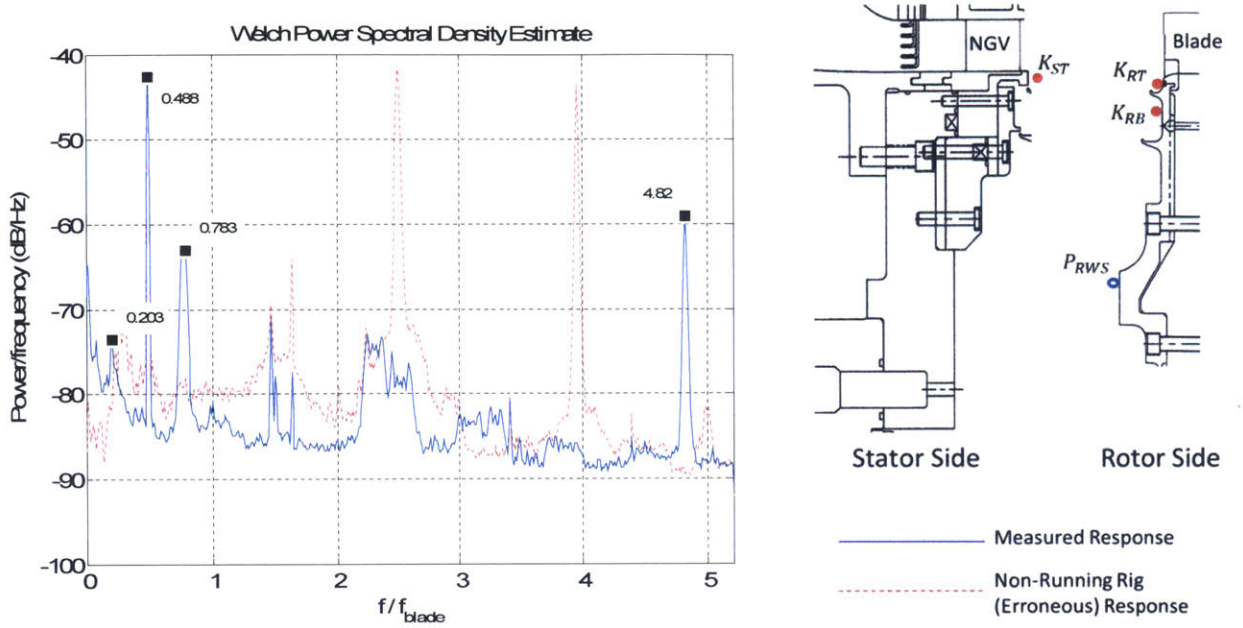

Figure 3.4: PSD for K_{RB} – Kulite in buffer cavity on rotor surface for Configuration 1. Responses are normalized to the blade passing frequency.

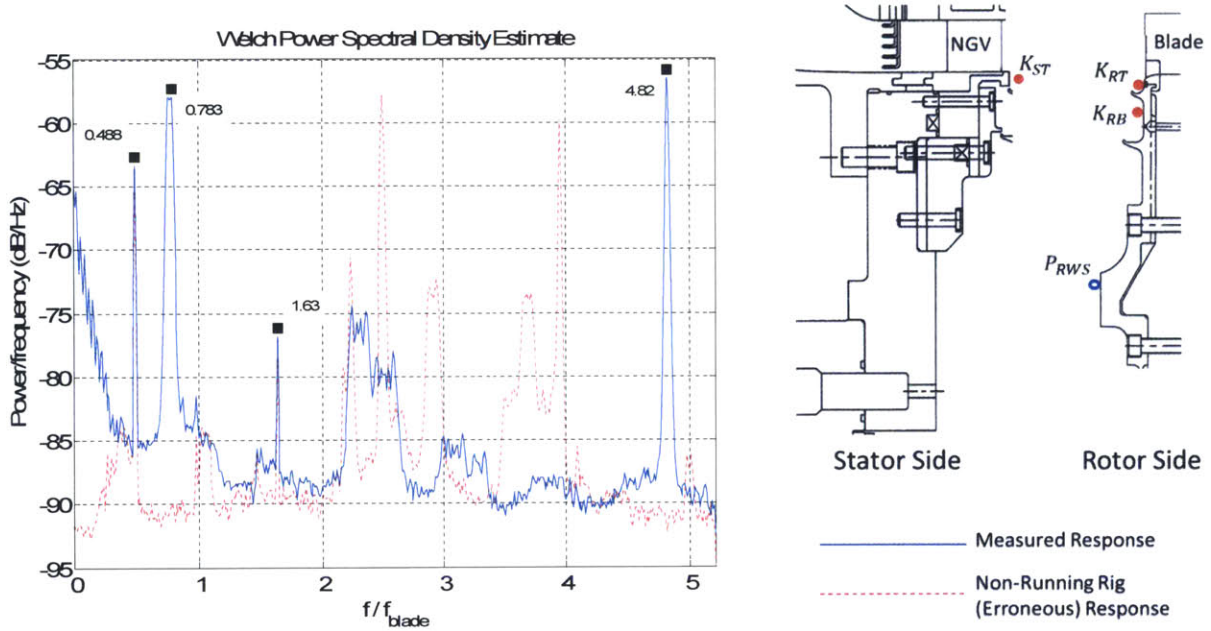

Figure 3.5: PSD for P_{RWS} – Pressure measurement in wheelspace on rotor surface for Configuration 1. Responses are normalized to the blade passing frequency. Erroneous data points are present at 0.488 and 1.63. Hypothesized Shallow Cavity response is present at 0.783 of blade passing frequency.

To summarize:

i. The responses from Kulites at various locations within the cavity show the existence of Shallow Cavity mode and Helmholtz resonant mode.

ii. It can be inferred from the data presented above that there is attenuation of the unsteady pressure response associated with the passing of the airfoils in the buffer and wheelspace cavities.

3.3 Effect of Rotational Reynolds Number on Unsteady Response

The second set of data interrogation consists of assessing whether the rotational Reynolds number has an impact on frequency content and magnitude of the unsteady pressure field. This assessment will provide guidance for identifying the causes of these frequencies.

Configuration 1 was tested for three different rotor speeds at the 0.8% purge flow level. The corresponding rotational Reynolds numbers Re_Ω are 2.04E6, 3.06E6, and 3.87E6 for the three rotor speed levels. To investigate the effect of these rotor speeds on the unsteady pressure response, the Kulite on the rotor surface in the trench cavity (K_{RT}) presented in Figure 3.3 will be assessed for each Re_Ω. It is hypothesized that the unsteady pressure response resulting from cavity modes will be unaffected by the rotational Reynolds number of the flow.

Figure 3.6 presents the power spectrum for the experiment corresponding to $Re_\Omega = 3.87E6$. Because the rotational speed is higher for this situation, the blade passing frequency is also greater and is reflected in the different f_{blade} scale in the plot. The passing NGV response and harmonic can still be seen at $Re_\Omega = 3.87E6$ and with similar magnitude to the $Re_\Omega = 3.06E6$ situation. The hypothesized Helmholtz and Shallow Cavity responses are present at 0.22 and 0.741 with similar magnitudes. Higher-order harmonics that were present in the $Re_\Omega = 3.06E6$ data are not observed in the $Re_\Omega = 3.87E6$ situation.

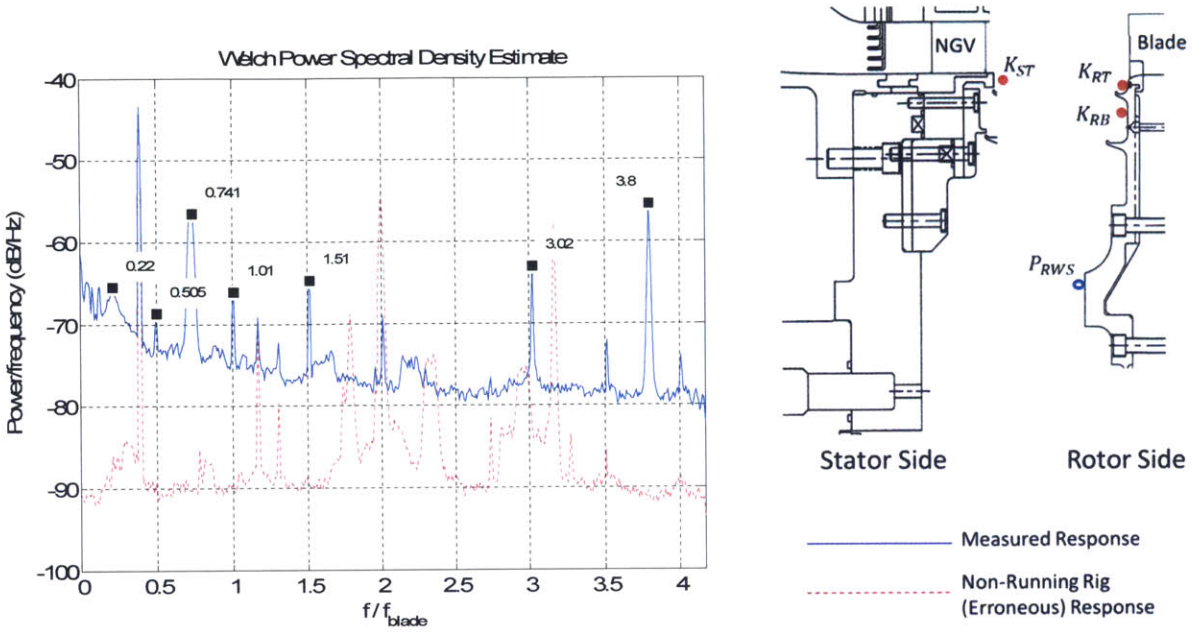

Figure 3.6: PSD for K_{RT} – Kulite in trench cavity on rotor surface at $Re_\Omega = 3.87E6$ for Configuration 1. Responses are normalized to the blade passing frequency. Hypothesized Helmholtz and Shallow Cavity responses are present at 0.22 and 0.741 of blade passing frequency, respectively.

Figure 3.7 presents the power spectrum for the $Re_\Omega = 2.04E6$ experiment. Because the rotational speed is lower for this situation, the blade passing frequency is also lower and is reflected in the different f_{blade} scale in the plot. The passing NGV response can be seen at the $Re_\Omega = 2.04E6$ level and appears to have greater amplitude than the $Re_\Omega = 3.87E6$ situation. Although several harmonics are captured for $Re_\Omega = 3.87E6$ (1.0, 1.5, 2.0, ...), these were not seen in the Kulite data for $Re_\Omega = 2.04E6$. The hypothesized Helmholtz response is not apparent, but the Shallow Cavity response appears at 1.1 with a similar magnitude.

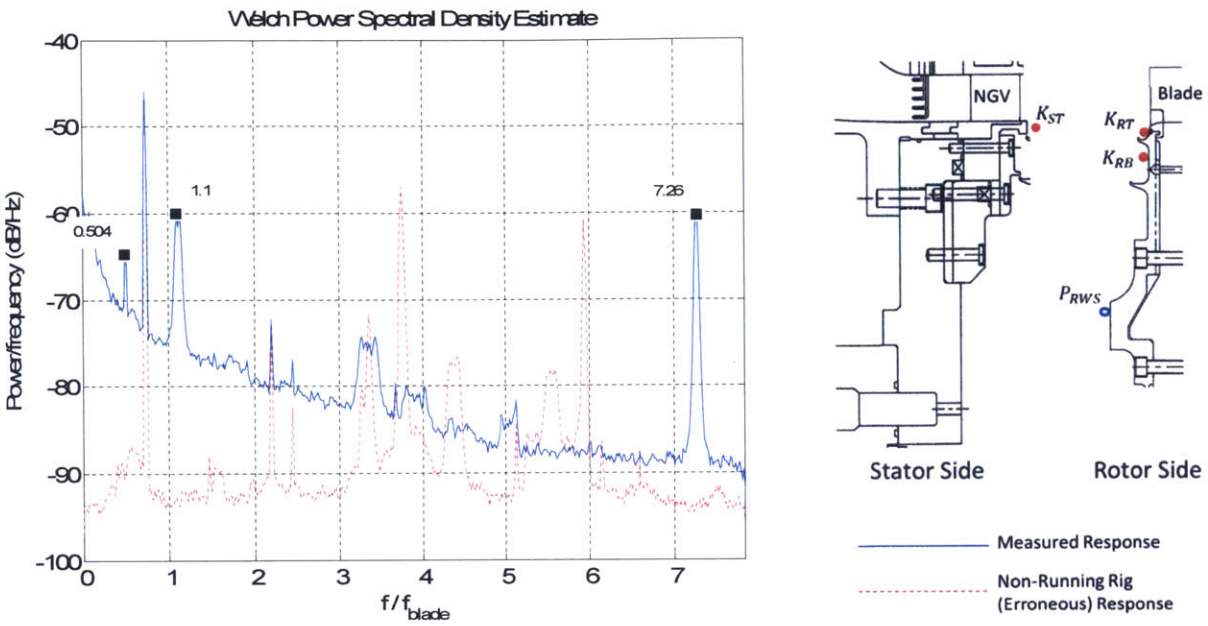

Figure 3.7: K_{RT} – Kulite in trench cavity on rotor surface at $Re_{\Omega} = 2.04E6$ for Configuration 1. Responses are normalized to the blade passing frequency. Hypothesized Shallow Cavity response is present at 1.1 of blade passing frequency.

To summarize:

i. It can be inferred that the Shallow Cavity and the Helmholtz response appear to be unaffected by the variation in rotational Reynolds number.

ii. The higher harmonics associated with the NGV are suggested at high rotational Reynolds number.

3.4 Effect of Purge Flow on Unsteady Flow Response

The third set of data interrogation consists of assessing whether the level of purge flow between the rotor and stator has an effect on the frequency content and magnitude of the unsteady pressure field.

A set of experiments was performed on a separate configuration that will be referred to as Configuration 2. The Kulites for this experiment were in the trench and buffer cavities at the same location as for Configuration 1.

Configuration 2 was tested for three different purge flow levels at $Re_{\Omega} = 3.87E6$. These purge flow levels are 0.8%, 1.6%, and 3.2% of gaspath mass flow purge levels. To investigate the effect of the purge flow levels on the unsteady pressure response, a Kulite on

the stator surface in the trench cavity will be compared between the purge flow levels. It is hypothesized that increasing purge flow will result in decreasing amplitude of the unsteady pressure response.

Figure 3.8 presents the power spectrum for the 0.8% purge flow experiment. The blade passing response is present along with the 2nd-4th harmonics. Hypothesized Helmholtz response is present at 0.353 and Shallow Cavity responses are present at 1.33 for the first mode and 3.45 for the higher-order second mode.

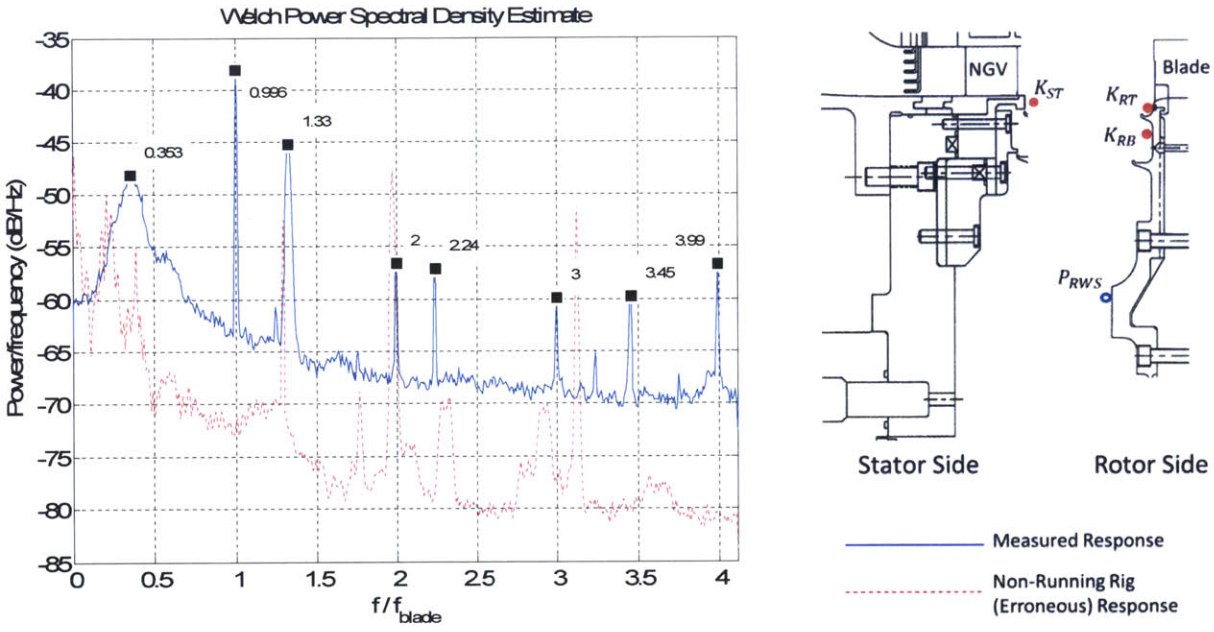

Figure 3.8: PSD for K_{ST} – Kulite in trench cavity on stator surface with 0.8% purge flow on Configuration 2. Responses are normalized to the blade passing frequency. Hypothesized Helmholtz response is present at 0.353 and Shallow Cavity first and second mode responses are present at 1.33 and 3.45 of blade passing frequency, respectively.

Figure 3.9 presents the power spectrum for the 1.6% purge flow experiment. The blade passing response is present along with the 2nd-4th harmonics with similar magnitude to the 0.8% purge flow response. Hypothesized Helmholtz response is present at 0.353 and Shallow Cavity responses are present at 1.33 for the first mode and 3.45 for the higher-order second mode.

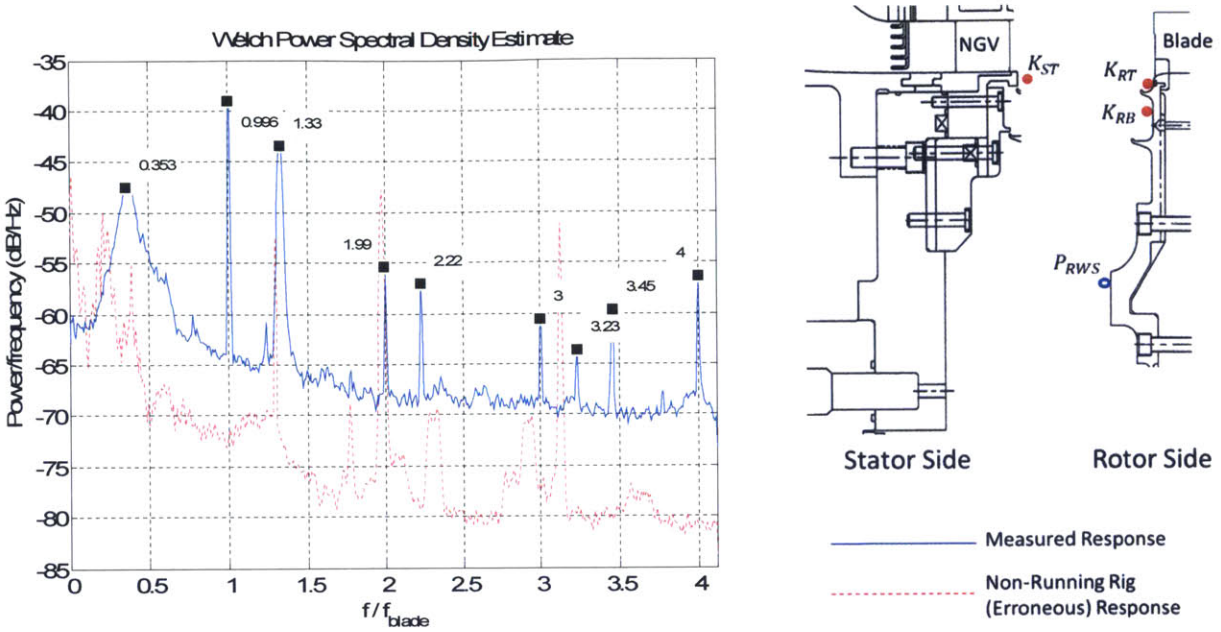

Figure 3.9: K_{ST} – Kulite in trench cavity on stator surface with 1.6% purge level on Configuration 2. Responses are normalized to the blade passing frequency. Hypothesized Helmholtz response is present at 0.353 and Shallow Cavity first and second mode responses are present at 1.33 and 3.45 of blade passing frequency, respectively.

Figure 3.10 presents the power spectrum for the 3.2% purge flow experiment. Again, the blade passing response is present along with the 2nd-4th harmonics, with lower magnitude than the other two cases. Hypothesized Helmholtz response is present at 0.321 and Shallow Cavity responses are present at 1.38 for the first mode and 3.42 for the higher-order second mode.

Figure 3.11 provides a comparison of the response amplitudes for the three separate purge flow levels. The magnitude of the blade passing response is 15% lower for the highest purge flow level. The Helmholtz Resonance response magnitude only demonstrates 3% variation between the different purge flow levels. There is a 10% variation in response amplitude for the Shallow Cavity modes, where the first mode exhibits decreasing amplitude and the second mode demonstrates increasing amplitude for increasing purge flow level.

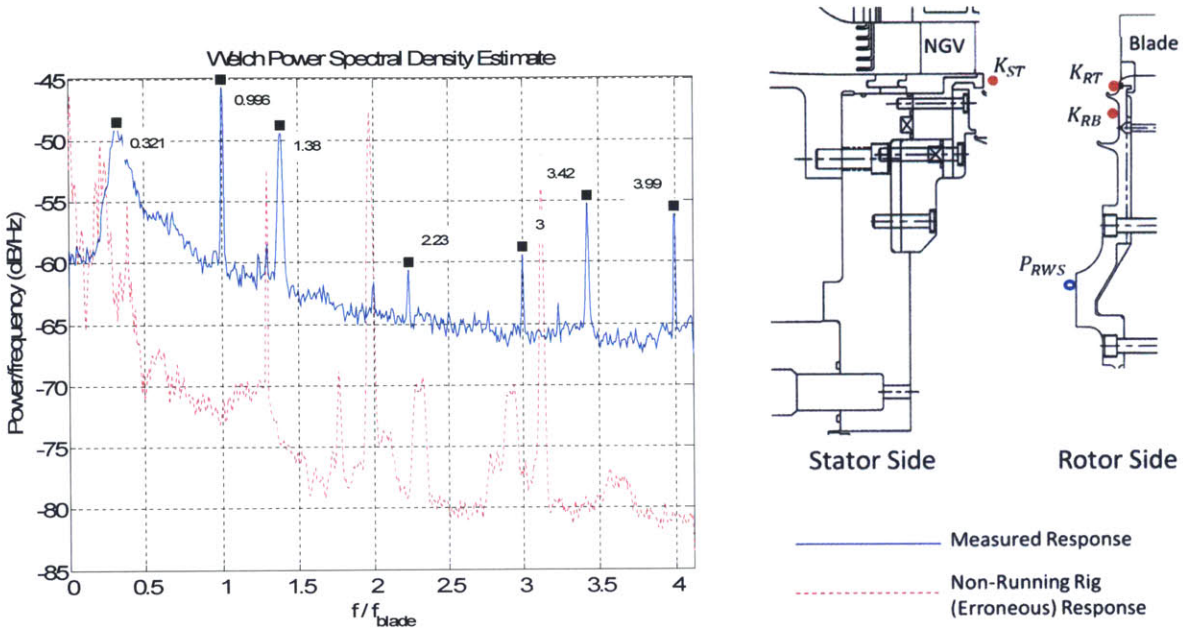

Figure 3.10: K_{ST} – Kulite in trench cavity on stator surface with 3.2% purge level on Configuration 2. Responses are normalized to the blade passing frequency. Hypothesized Helmholtz response is present at 0.321 and Shallow Cavity first and second mode responses are present at 1.38 and 3.42 of blade passing frequency, respectively.

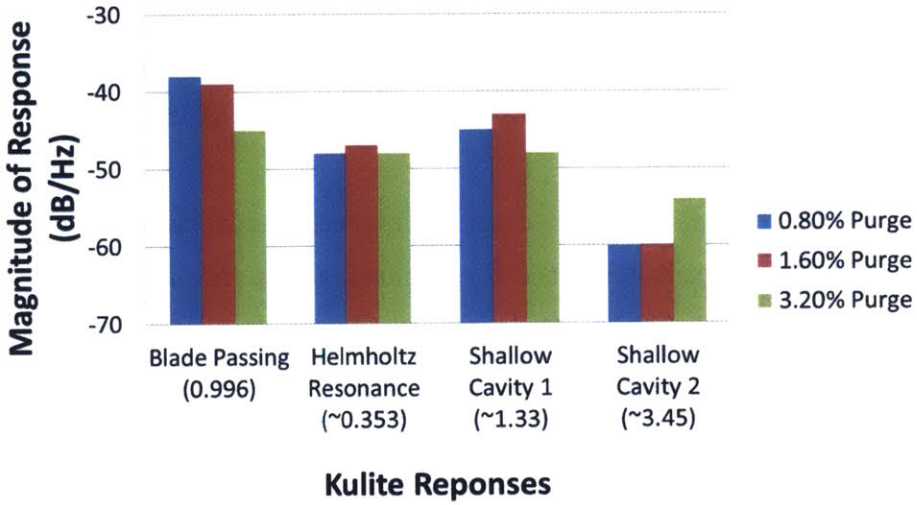

Figure 3.11: Comparison of response amplitudes for K_{ST} (Kulite in trench cavity on stator surface) for varying purge levels 0.8%-3.2% for hypothesized sources of unsteady pressure variation.

In summary:

i. There is negligible quantitative difference in the frequencies measured for Blade Passing, Shallow Cavity, and Helmholtz responses at the different purge flow levels that were tested for $Re_\Omega = 3.87E6$.

ii. There is negligible variation in response amplitude for the Helmholtz response, but a variation larger than 10% in Blade Passing and Shallow Cavity response amplitudes due to the different purge flow levels that were tested for $Re_\Omega = 3.87E6$.

3.5 Helmholtz Resonance

3.5.1 Calculation

A Helmholtz resonance is a consequence of an excitation by a shear layer across a cavity opening leading to fluid dynamic/acoustic coupling as the cavity is subjected to a pressure disturbance. Figure 3.12 depicts a typical Helmholtz resonator and the hypothesized application to the buffer cavity. In this approximation, the buffer cavity represents the volume while the rim seal represents the neck in a Helmholtz resonator. Also shown in the figure is the equivalent spring-mass system representation of a Helmholtz resonator.

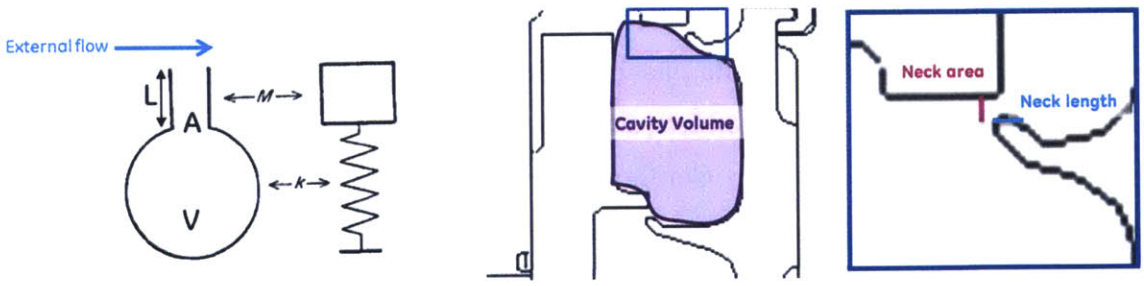

Figure 3.12: (a) Canonical Helmholtz resonator and equivalent spring-mass system adopted from Alster [33].
(b) Application of canonical resonator to turbine-rim buffer cavity geometry whereby the volume is represented by the buffer cavity and the neck geometry is represented by the outer rim seal.

3.5.2 Helmholtz Mode Response Identified in HGIR Data

Three HGIR configurations, shown in Figure 3.13 were interrogated for evidence of a Helmholtz resonance, each with a different buffer cavity. Configuration 1, described in Section 3.2 was retested and that data is presented here. Configuration 2 has a buffer cavity width equal to 80% that of Configuration 1, and Configuration 3 has a buffer cavity height equal to 25% that of Configuration 1 and Configuration 2.

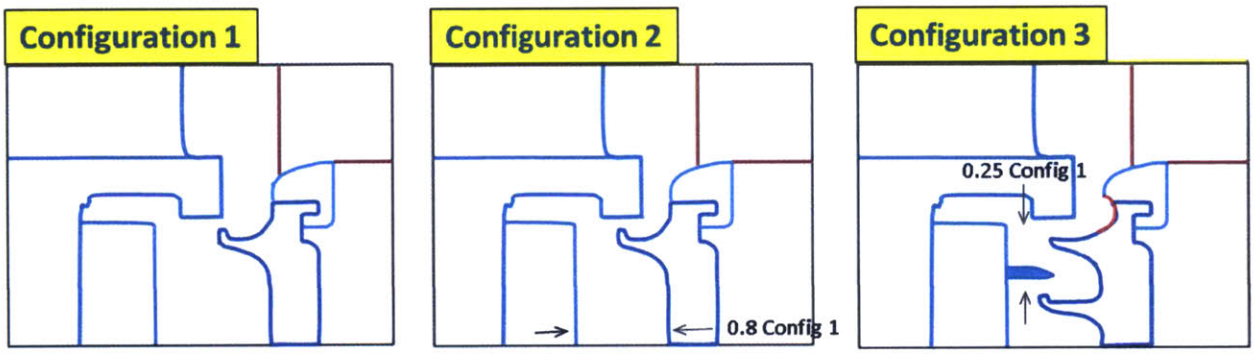

Figure 3.13: Comparison of Configurations 1-3 for Helmholtz resonator study. Configuration 2 has a narrower buffer cavity than Configuration 1 and Configuration 3 has a shorter buffer cavity that eliminates the distinct volume apparent in Configurations 1 and 2.

The data used for assessing the three configurations for the existence of Helmholtz resonant mode is for the turbine stage operating with 0.8% purge flow level and $Re_{\Omega} = 3.87E6$. The Kulite data is from the trench cavity on the stator surface (K_{ST}). Table 3.1 shows a comparison between the calculated and measured responses of experiments implemented in the HGIR for the three configurations. The reduced frequency as well as the frequency normalized to the blade passing frequency are provided. The measured frequency is comparable to the calculated frequency using an effective neck length of 1.55 times the physical neck length. Between Configurations 1 and 2, the frequency is expected to increase due to the smaller buffer cavity volume. For Configuration 3, a Helmholtz response is not expected because a distinct cavity volume is no longer present.

	f/f_{blade} , $\left[\frac{fW_b}{U_{\infty x}}\right]$		
	Calculated Using Equation 1.3 (Physical Length)	Calculated Using Equation 1.3 (Effective Length of 1.55 Physical Neck Length)	Measured
Configuration 1	0.43, [7.27]	0.31, [5.25]	0.31, [5.25]
Configuration 2	0.48, [6.49]	0.35, [4.71]	0.36, [4.84]
Configuration 3	Not present	Not present	Not present

Table 3.1: Assessing Helmholtz frequency using Equation 1.3 against measured values from Kulite data for 3 different rim-cavity configurations with 0.8% purge flow and $Re_{\Omega} = 3.87E6$. The response is normalized by the blade passing frequency and the quantity in [] is the reduced frequency.

Figure 3.14, Figure 3.15, and Figure 3.16 below present the normalized frequency response for each configuration. Overlaid with this response is the response from the same Kulite sensor during a non-running rig condition to bring out the "erroneous" non-physical frequency data. Any non-physical response is indicated by a red dotted line in the figures. The measured frequencies that are associated with the Helmholtz resonant mode are indicated in each figure. There is no response comparable to the Helmholtz resonant mode in Figure 3.16.

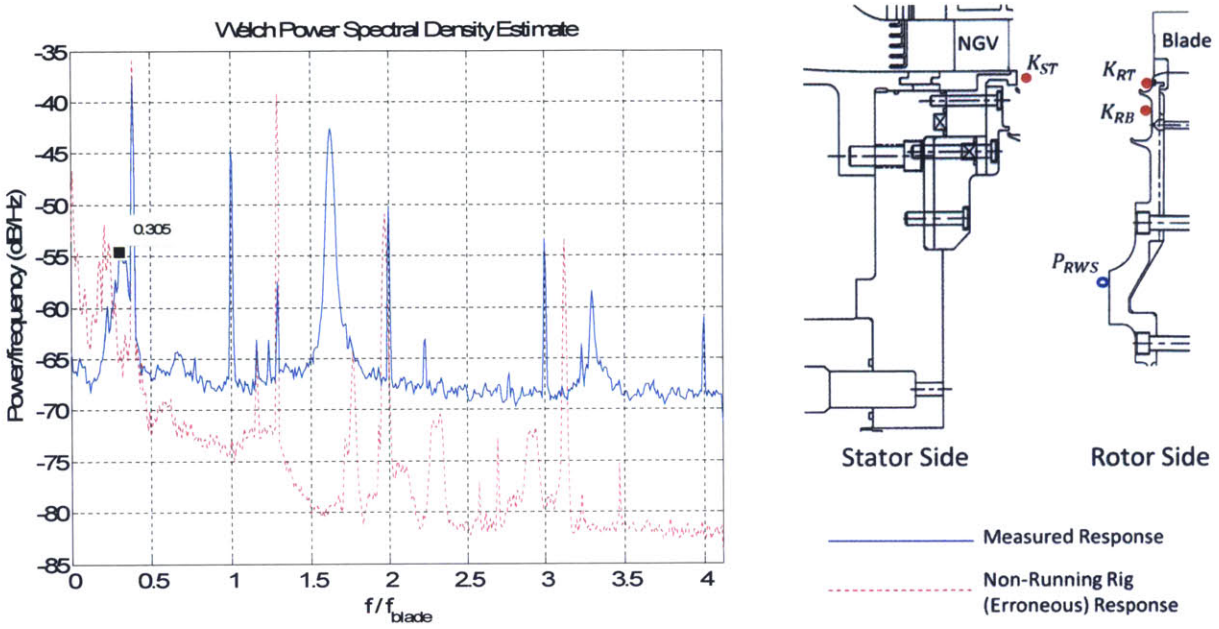

Figure 3.14: K_{ST} – Kulite in trench cavity on stator surface on Configuration 1 that was re-tested. Responses are normalized to the blade passing frequency. Hypothesized Helmholtz response is present at 0.305 of blade passing frequency.

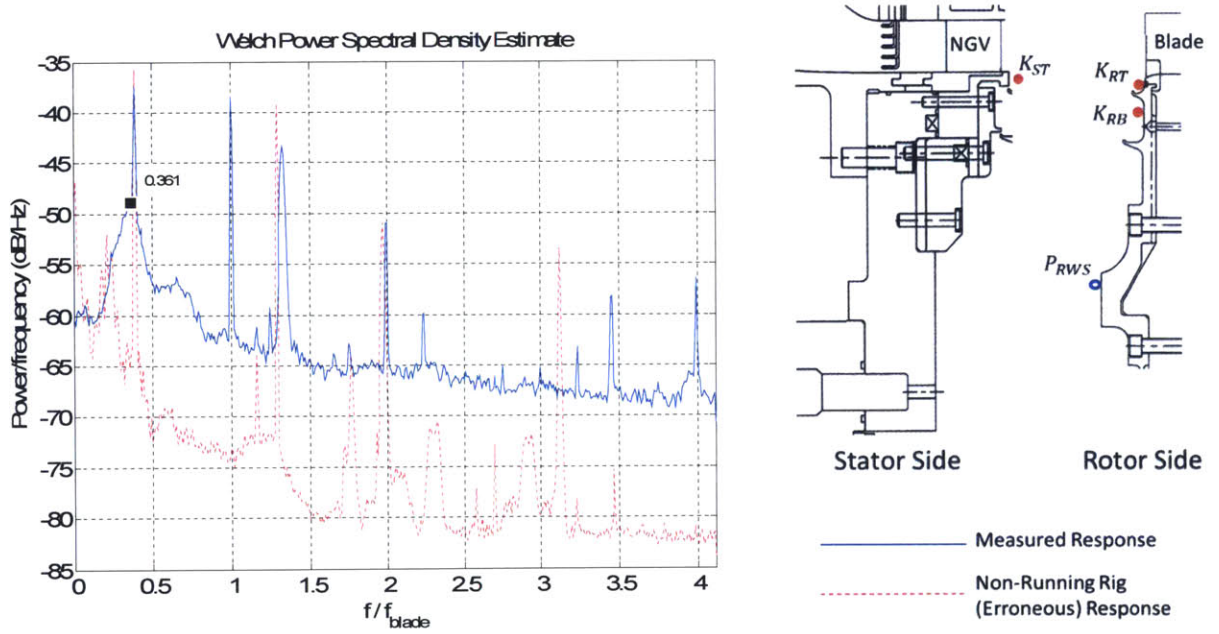

Figure 3.15: K_{ST} – Kulite in trench cavity on stator surface on Configuration 2. Responses are normalized to the blade passing frequency. Hypothesized Helmholtz response is present at 0.361 of blade passing frequency.

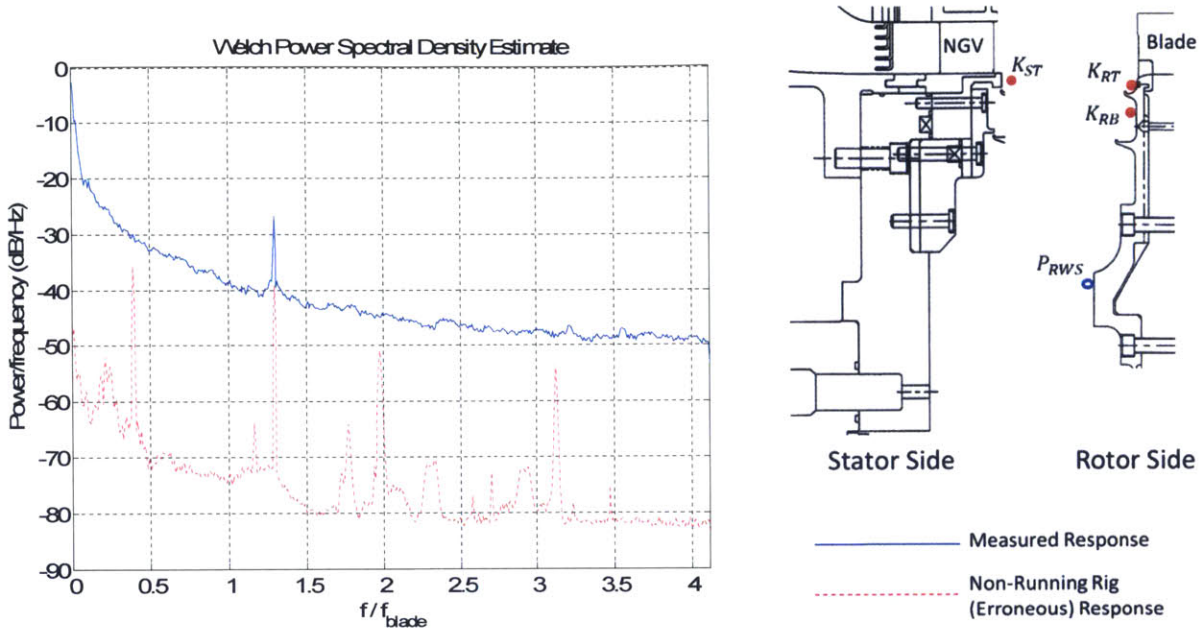

Figure 3.16: K_{ST} – Kulite in trench cavity on stator surface on Configuration 3. Responses are normalized to the blade passing frequency. Helmholtz response is not present, as hypothesized.

To summarize:

i. The expected shift in response associated with Helmholtz resonant mode is present in the data for Configurations 1 and 2, and the response does not appear for Configuration 3 as expected.

ii. The findings presented above support the hypothesis on the existence of Helmholtz acoustic response in a representative turbine rim-cavity-wheelspace configuration.

3.6 Shallow Cavity Mode

3.6.1 Calculation

A shallow cavity mode is an acoustic disturbance generated by instability in a shear layer over a cavity that forms a vortex and impinges on the opposing surface. Figure 3.17 depicts a typical example of shallow cavity mode behavior and the hypothesized application to the

trench cavity. In this approximation, the width of the trench cavity would be the extent over which the vortex is convected.

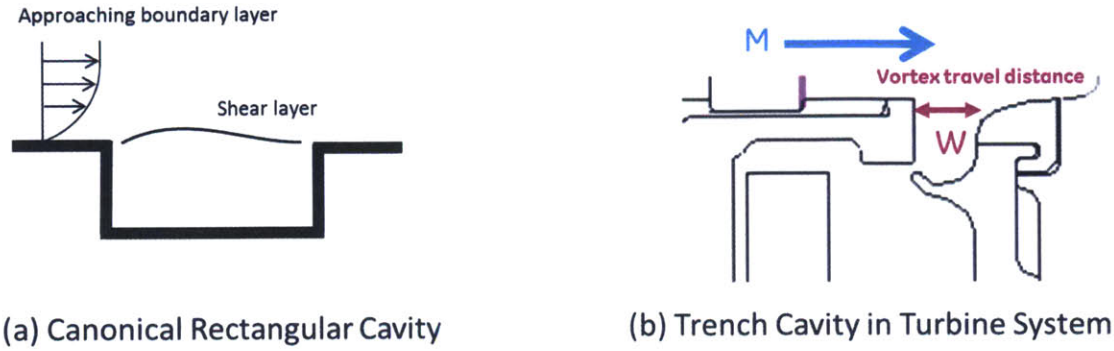

Figure 3.17: (a) Excitation of Shallow Cavity mode by shear layer over a rectangular cavity.
(b) Application to trench cavity in turbine system.

3.6.2 Shallow Cavity Mode Response in HGIR Data

Two turbine rim-cavity configurations were evaluated on the HGIR for evidence of a shallow cavity response, each with a different trench cavity width. Configuration 1 was described in Section 3.2 . Configuration 2, described in Section 3.5 , has a trench cavity width equal to half that of Configuration 1. These configurations are shown in Figure 3.18.

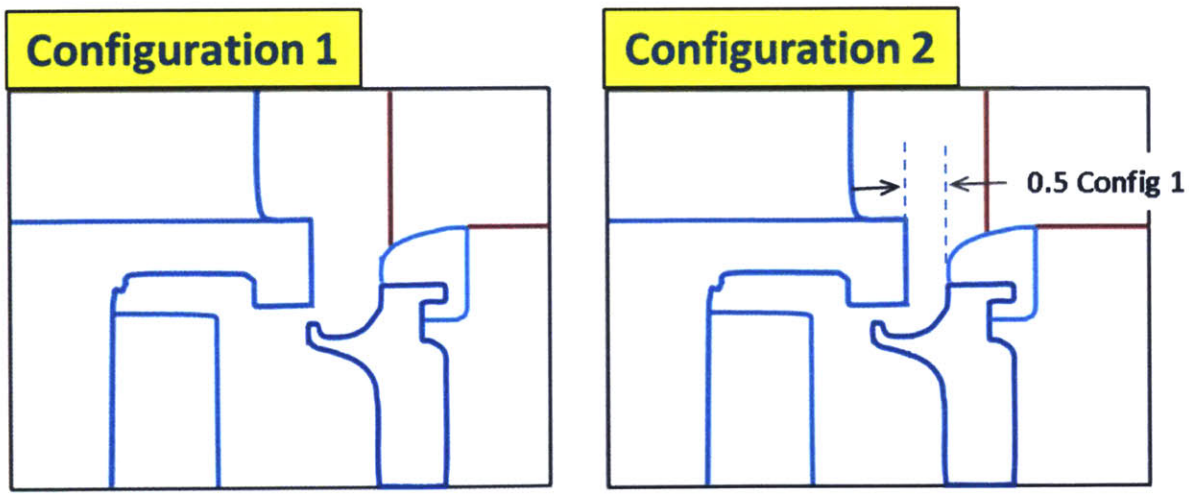

Figure 3.18: Comparison of Configurations 1 and 2 for Shallow Cavity mode study. Configuration 2 has a narrower trench cavity than Configuration 1, which would be expected to shift the Shallow Cavity mode frequency response.

The data used for assessing the two configurations for the existence of shallow cavity mode is taken for the turbine rig operating with 0.8% purge flow level and $Re_{\Omega} = 3.87E6$. The Kulite data is from the trench cavity on the stator surface (K_{ST}). Table 3.2 shows a comparison between the calculated and measured responses of experiments implemented on the HGIR for the two configurations delineated above. The frequency is expected to increase by a factor of 2 between Configurations 1 and 2 because of the dependence on trench cavity width. Both the frequency normalized to blade passing, as well as the reduced frequency, is provided.

	f/f_{blade} , $\left[\frac{fW_t}{U_{\infty x}}\right]$			
	Mode 1		Mode 2	
	Calculated Using Equation 1.1	Measured	Calculated Using Equation 1.1	Measured
Configuration 1	0.66, [4.45]	0.74, [5.09]	1.53, [10.39]	1.17, [8.04]
Configuration 2	1.31, [4.45]	1.33, [4.53]	3.05, [10.39]	3.46, [11.77]

Table 3.2: Calculated versus measured shallow cavity response frequency normalized by blade passing frequency, as well as shown by reduced frequency.

Due to measurement uncertainty for calculating the Mach number in the main gaspath, a range of expected responses can be calculated to take into account the uncertainty. Figure 3.19 and Figure 3.20 below present the normalized frequency response for each configuration as well as the computed range of expected frequency.

For Configuration 1, there are two frequencies within or near the calculated response range for a Shallow Cavity. These frequencies are at 0.741 and 1.17. Neither of these frequencies corresponds to a frequency associated with noise. These frequencies are expected to double in value for Configuration 2 due to the narrower trench cavity width. The results for Configuration 2 show responses at 1.33 and 3.45. These are within or near the calculated response range.

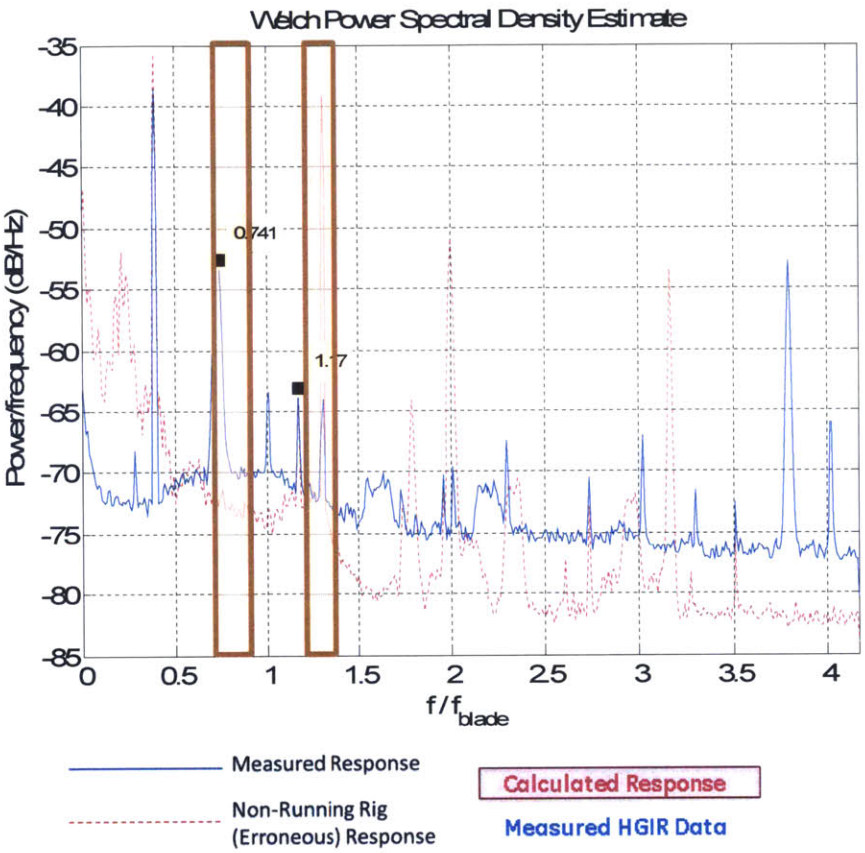

Figure 3.19: K_{ST} – Kulite in trench cavity on stator surface on Configuration 1. Responses are normalized to the blade passing frequency. Hypothesized Shallow Cavity response is present at 0.741 and 1.17 blade passing frequency for the 1st and 2nd modes, respectively. Measurements are in good agreement with calculated response.

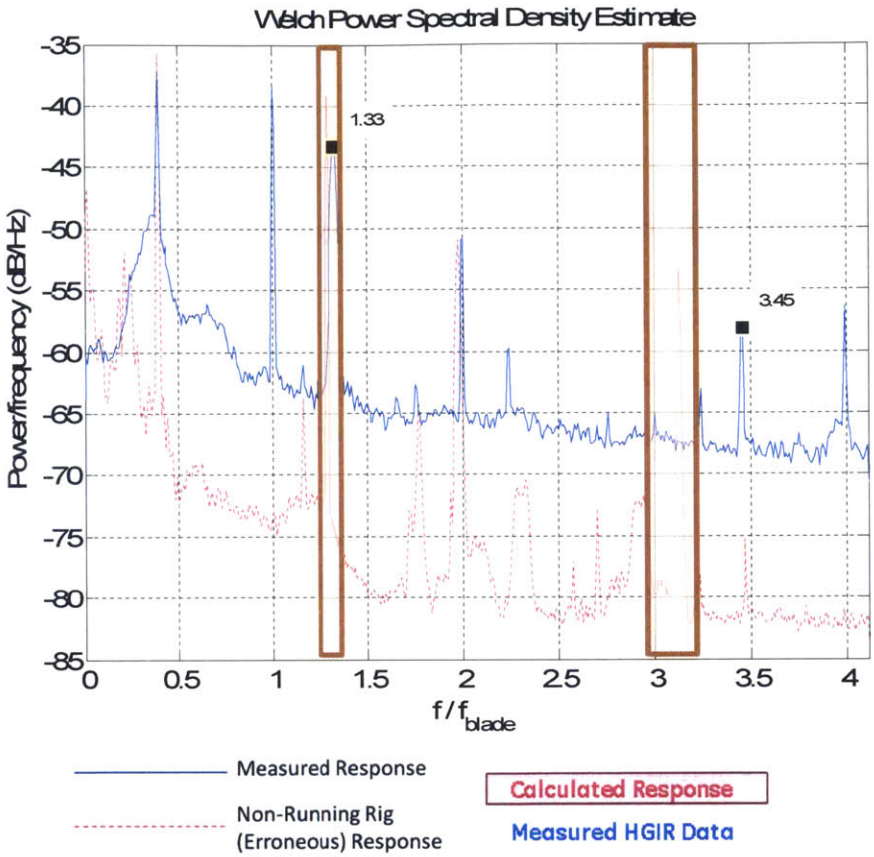

Figure 3.20: K_{ST} – Kulite in trench cavity on stator surface on Configuration 2. Responses are normalized to the blade passing frequency. Hypothesized Shallow Cavity response is present at 1.33 and 3.45 blade passing frequency for the 1st and 2nd modes, respectively. Measurements are in good agreement with calculated response.

In summary:

i. Responses are present in the data at the estimated frequency range for both configurations.

ii. The relative shift in frequency response between Configuration 1 and Configuration 2 are approximately equal to the estimated values, supporting the hypothesis of the presence of shallow cavity modes 1 and 2.

3.7 Assessment of Shallow Cavity Mode with Additional Parametric Experiments

3.7.1 Plan and hypothesis for additional experiments

The assessment of HGIR Kulite data thus supports the hypothesis of a shallow cavity mode in the trench cavity. To further assess this hypothesis, additional experiments were planned on the rig to provide additional data. A new configuration, developed by GRC and designated as Configuration 4 was installed on the rig along with a new set of Kulites on the stator side of the trench cavity. The geometry of this configuration is not disclosed due to GE proprietary information agreement. The experiments for this configuration were planned to take place during the shakedown testing of the new rig configuration.

3.7.1.1 Shallow cavity mode

From the expression in Equation 1.1, one infers that the key parameter affecting the reduced frequency, $\frac{fW_T}{U_{\infty x}}$, of the shallow cavity mode is the Mach number of the flow moving across the trench in the main flowpath. Since the experiments were carried out on only one configuration, the velocity of the flow moving across the trench was varied for the experiment. NGV trailing edge Mach numbers of 0.29, 0.42, and 0.6 were achieved with the rig and were expected to provide sufficient shift in frequency response for assessing the shallow cavity mode.

Because several Kulites had failed during previous HGIR experiments, a new set of Kulites was installed to provide reliable data with repeatability. The cause of Kulite failure during previous testing was thought to be a result of high temperatures in the gas flowpath. For the new set of experiments designed to assess the shallow cavity mode, a lower gas temperature below 100°F was used to mitigate potential issues of Kulite failure due to high temperatures. The spanwise-average Mach number at the exit of the NGV (and approximate Mach number at the trench leading edge) was calculated using the NGV inlet and exit conditions. The total purge flow for the cavity was held constant for this new set of

experiments. The data acquisition system (DAQ) recorded 8 sets of data from the Kulites at 100 kHz sample rate for 1 second duration.

The rotor speed was varied for each of the three Mach number conditions. Expected blade/nozzle passing frequencies were calculated for each experimental case. In the previous experiments, the NGV and blade passing frequencies were clearly seen in the frequency response/power spectrum of the HGIR Kulite data. Therefore, blade passing frequency was expected in the frequency response for this set of experiments. Unfortunately, there was significant noise at the lower frequency range near the blade passing frequency, so clear measurements of that frequency were not able to be undertaken in these experiments.

The expected responses based on the expression given in Equation 1.1 for the first and second modes of the shallow cavity response were calculated and are given in Table 3.3. The given range accounts for measurement uncertainty in the instrumentation. A Helmholtz resonance mode is not expected for this configuration based on the rim-cavity geometry characteristics.

	f/f_{blade}		$\frac{fW_t}{U_{\infty x}}$	
	Mode 1	Mode 2	Mode 1	Mode 2
M = 0.29	11.7-12.9	27.3-30.0	4.13-4.56	9.64-10.59
M = 0.42	9.1-11.4	21.3-26.5	3.70-4.63	8.66-10.77
M = 0.60	10.0-10.3	23.3-24.0	3.96-4.08	9.22-9.50

Table 3.3: Calculated shallow cavity response frequency using Equation 1.1 for shallow cavity modes; the computed frequency has been normalized using the blade passing frequency and also provided as the reduced frequency.

3.7.2 Assessment of Experimental Results Against Calculations

Figure 3.21 shows the frequency spectrum of the Kulite data from each of the experiments in order to assess shallow mode variation with Mach number. Kulite data was taken with the rig static (i.e. not operating with any flow in the rig) to provide baseline noise in the signal. This signal noise is plotted on top of each case to facilitate identifying which fre-

quency responses would have a physical source. The calculated frequency range is also provided. The range is calculated based on the standard deviation of pressure and temperature measurements used to calculate the Mach number at the trailing edge.

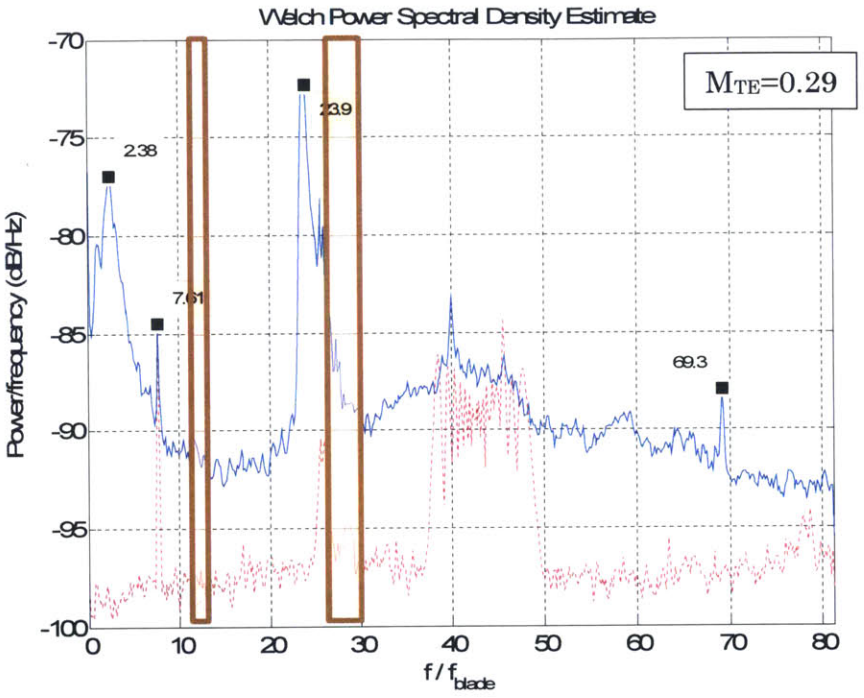

(a)

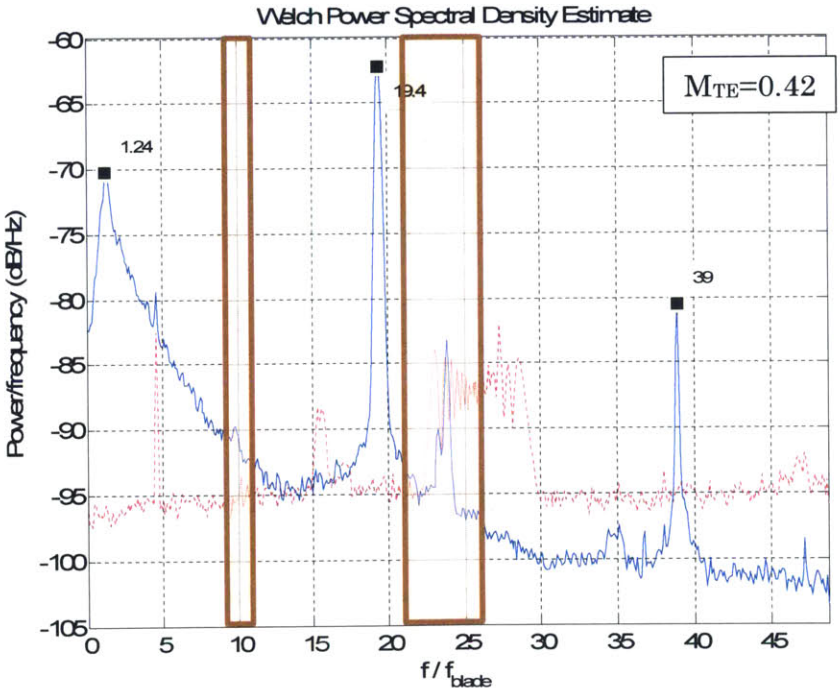

(b)

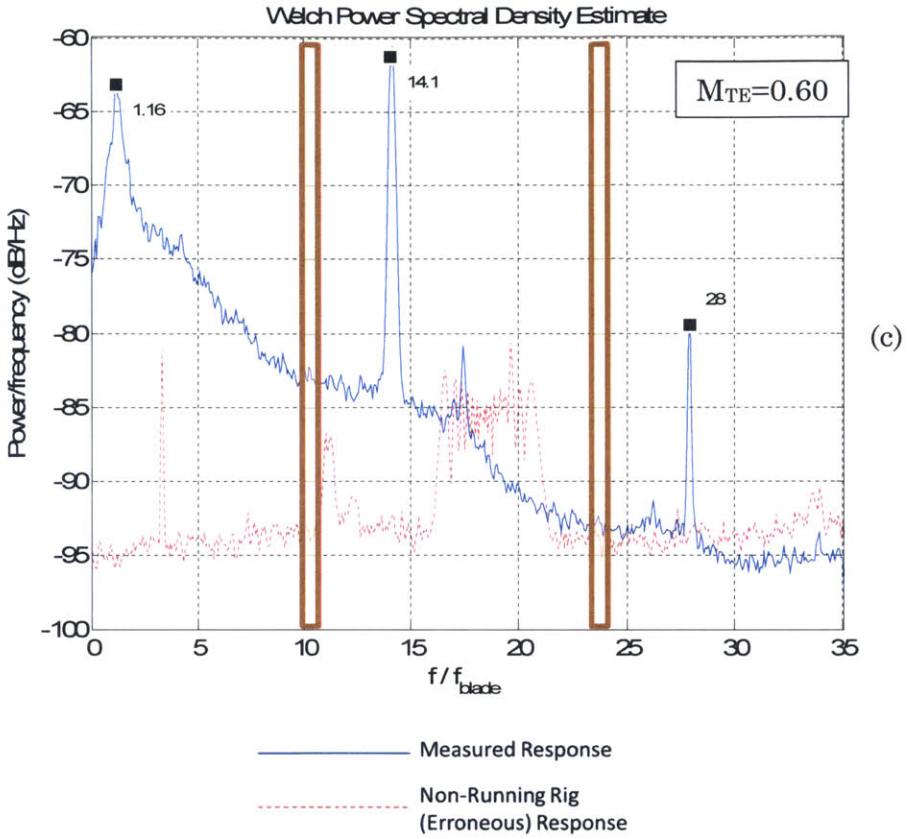

Figure 3.21. Frequency spectrum for HGIR trench cavity Kulite (K_{ST}) normalized by blade passing frequency for (a) M=0.29, (b) M=0.42, and (c) M=0.60. Red dotted-line curve represents noise in the signal. Blue solid curve represents signal recorded by Kulite during experimental run. Hypothesized Shallow Cavity 2nd mode response is present at 23.9 for M=0.29 with a shift to 19.4 for M=0.42. However, the response does not shift as hypothesized for M=0.60.

There are three prominent frequencies in the data that do not correspond to any signal noise. The first prominent frequency occurs at approximately 1.2-2.4 f_{blade}. This is hypothesized to be related to the Helmholtz response. The Helmholtz frequency was calculated using Equation 1.3 with the effective neck length equal to 1.55 times the physical neck length, as in Section 3.5.2 . However, the expected Helmholtz frequency calculated is an order of magnitude higher than the measured frequency, so further interrogation of the data is required to understand the source.

The next prominent frequency occurs at 23.9, 19.4, and 14.1 f_{blade} respectively for each experiment. The calculated shallow cavity response, accounting for measurement uncertainty in calculating the Mach numbers, is plotted in the figures. For M=0.29 and M=0.42, the measured frequencies fall just below the calculations for the second mode of the shallow

cavity mode frequency, but do show a trend consistent with the calculation. The 39 f_{blade} frequency for M=0.42 is equal to twice the 19.4, and therefore may be a harmonic of that frequency.

For M=0.60, the 14.1 f_{blade} measured response does not follow the expected trend. This condition also has a 28 f_{blade} frequency that is equal to twice the 14.1 measurement and may be a harmonic. At this time, it remains to be understood as to why the experimental response does not reflect the computed response as for the situations of M=0.29 and M=0.42.

Looking closer at the M=0.29 condition, there is a measured response at 7.61 that would fall approximately where the first Shallow Cavity mode response is expected. It appears this measurement may be contaminated by noise, as indicated by the measured response at that frequency when the rig was not running. Similarly, the M=0.42 condition shows measured response at approximately 5 that is also contaminated by noise but may be indicative of the first Shallow Cavity mode response.

3.8 Deep Cavity Mode

3.8.1 Calculation

A deep cavity mode is an acoustic disturbance generated by an instability in a shear layer over a cavity. This instability excites the natural acoustic mode in the cavity for a wave depth-wise into the cavity. Figure 3.22 depicts a typical example of deep cavity mode behavior and the hypothesized application to the trench cavity.

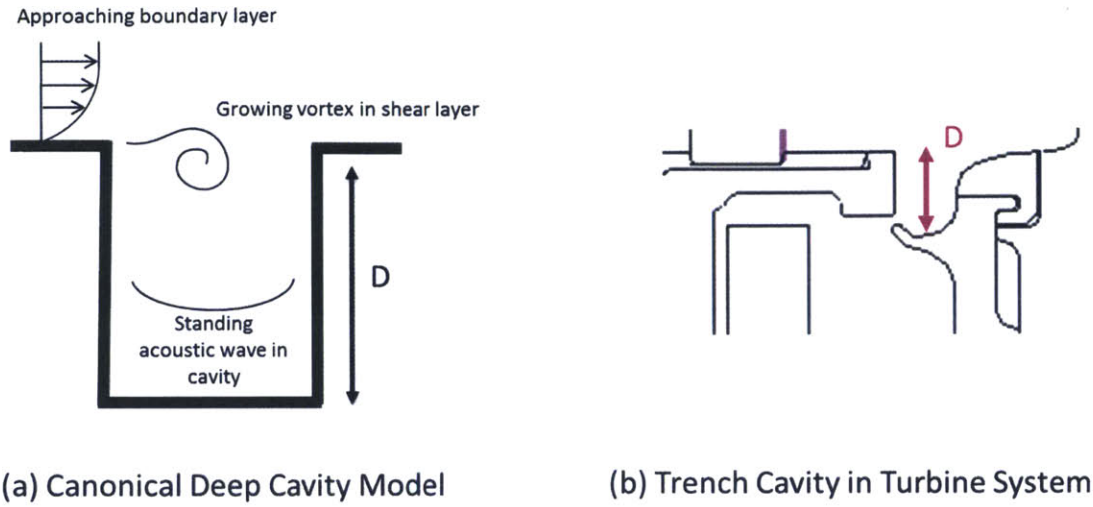

Figure 3.22. (a) Excitation of Deep Cavity mode by shear layer over a rectangular cavity.
(b) Application to trench cavity in turbine system.

3.8.2 Deep Cavity Mode Response in HGIR Data

East [20] performed experiments to understand unsteady pressure fields in deep cavities and developed an empirical formulation to determine the expected flow response in terms of resonant frequency given the cavity width and depth. This correlative relationship is given in Equation 3.1, where D is the cavity depth, W is the cavity width, and a is the speed of sound.

$$\frac{f_D \cdot D}{a}\left(1 + 0.65\left(\frac{W}{\mathrm{D}}\right)^{0.75}\right) = 0.25 \qquad \text{Equation 3.1}$$

The HGIR configurations were interrogated for evidence of a deep cavity response. However, the configurations showed no evidence of the expected response for deep cavity mode.

3.9 CO_2 Concentration Measurements on HGIR

As discussed in Section 2.3.1 , gas concentrations were measured along the stator disk to assess the level of hot gaspath ingestion for each configuration. To compare Configurations 1-3, the measurements from the 15 sensors located in the buffer cavity and shown in Figure

2.6 were averaged to provide a bulk assessment of sealing effectiveness for each configuration. The sealing effectiveness is defined in Equation 3.2 where $CO2_{WS}$ is the measured CO_2 level at the sensor, $CO2_{HGP}$ is the measured CO_2 level in the main gas flowpath, and $CO2_{Purge}$ is the measured CO_2 level of the purge air that is introduced into the wheelspace.

$$\eta_{CO2} = \frac{\mathrm{CO2_{WS}} - CO2_{HGP}}{CO2_{Purge} - CO2_{HGP}} \qquad \text{Equation 3.2}$$

Figure 3.23 plots the average sealing effectiveness for the Configurations analyzed in this chapter. Here we attempt to infer, albeit on an average basis, a correlation between the cavity mode response and sealing effectiveness. Configuration 2 had the highest amplitude Helmholtz and Shallow Cavity mode response amplitude and also has the lowest sealing effectiveness. This could suggest likelihood that the presence of cavity modes reduces the sealing effectiveness.

To establish conclusively the correlation between the cavity modes and sealing effectiveness would require time resolve data on CO_2 measurements. The measurements available are only time-averaged. However, adequate time and space-resolved measurements of the CO_2 data are needed to assess the impact of the Shallow Cavity and Helmholtz response on the sealing effectiveness of each configuration.

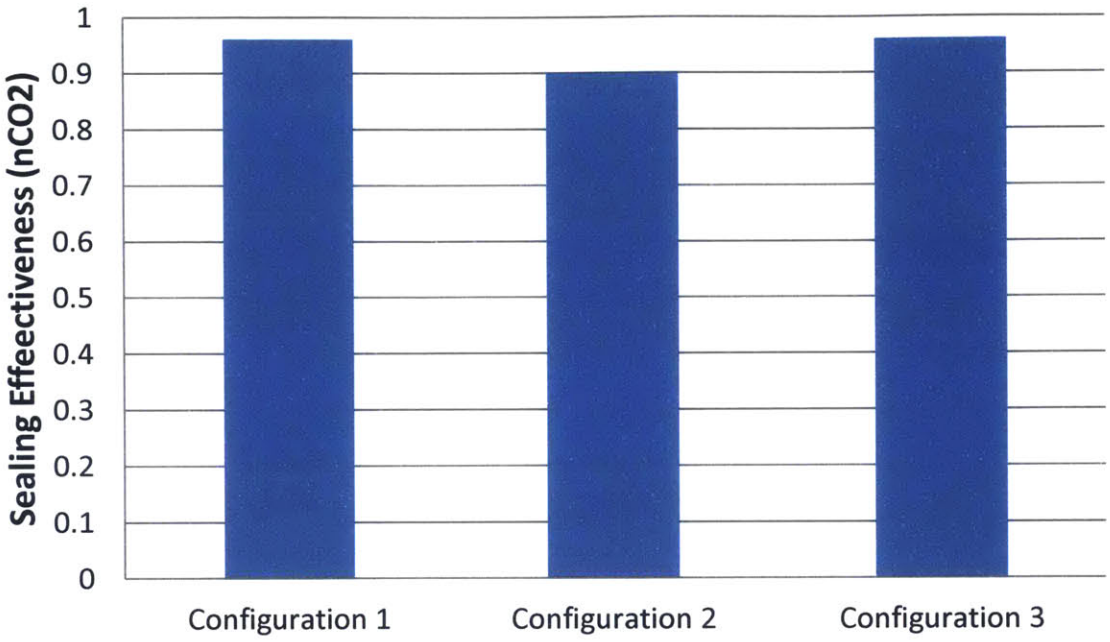

Figure 3.23: Sealing effectiveness based on average buffer cavity measurements for HGIR Configurations 1-3.

3.10 Summary of Experimental Results

In summary, the data from the HGIR shows the following:

1. Existence of Helmholtz resonant mode in the buffer cavity of the turbine rim-cavity system.
2. Existence of Shallow Cavity mode response in the trench cavity of the turbine rim-cavity system.
3. The cavity modes are unaffected by the change in rotational Reynolds numbers tested.
4. The Shallow Cavity response amplitude varies with purge flow for the levels tested.
5. Blade and NGV induced pressure disturbance is attenuated across the rim seals into the buffer and wheelspace cavities, but cavity mode responses are not.
6. Blade and NGV pressure disturbance harmonics increase in amplitude as flow coefficient decreases (corresponding to increasing rotor speed for the set of experiments) but cavity modes are unaffected by variation in the flow coefficient.

7. The amplitude of blade and NGV pressure disturbance as well as that of Shallow Cavity Mode 1 decrease with increasing purge flow, but the Helmholtz response is unaffected by purge flow levels.

Chapter 4 Computational Assessment of Shallow Cavity Mode

In this chapter, the Shallow Cavity mode is assessed computationally on canonical cavity geometry with key functionality representative of that in a turbine rim-cavity. The HGIR has parameters (in terms of geometry and flow conditions) beyond the canonical configuration, however consideration of purge flow and main flow swirl, which may affect the quantitative value of the frequency response, can readily be included as will be seen later. In order to understand the effects of rig-specific conditions on the calculated responses, CFD is used to model cavity mode experiments from literature and assess the effect of the additional parameters consisting of purge flow level (i.e. $\frac{\dot{m}_c}{\dot{m}_\infty}$) and main flow angle (i.e. $\frac{u_{\infty\theta}}{u_{\infty x}}$).

First, the computational results are assessed against available experimental data to ensure their fidelity. Next, upon satisfactory assessment, computational experiments are performed that reflect conditions of a representative gas turbine engine: mass injection (purge flow) and tangential flow in the main gas flowpath.

4.1 Canonical Experiment by Krishnamurty

The work by Krishnamurty [18] characterized the response of a simple 2D rectangular cavity with flow across its opening using the measurements from a hot-wire probe located on the forward wall of the cavity. A typical setup for his experimental investigation is shown in Figure 4.1. The experiment consisted of a cavity setup in a transonic wind tunnel. The cavity wall was adjustable to vary the width and provide variable width-to-depth aspect ratios. The results of his experiments are a set of empirical data that identifies a linear trend between the aspect ratio of the cavity and the dominant frequency response for several freestream Mach numbers. Krishnamurty published sufficient information on the situation with a flow Mach number of 0.75 and a cavity width-to-depth ratio of 0.5 to allow the setup of a computational model for assessments. Therefore, that case was selected for computational assessments as described below.

4.2 CFD model setup

The computational model of the cavity is shown in Figure 4.1. The stagnation temperature and pressure are defined at the inlet and an average static pressure is defined at the exit.

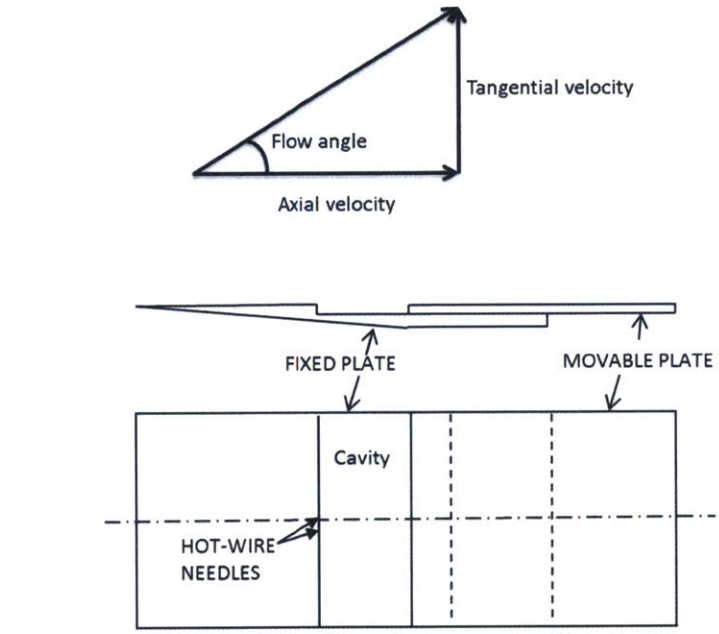

(a) Canonical Rectangular Cavity Experiment

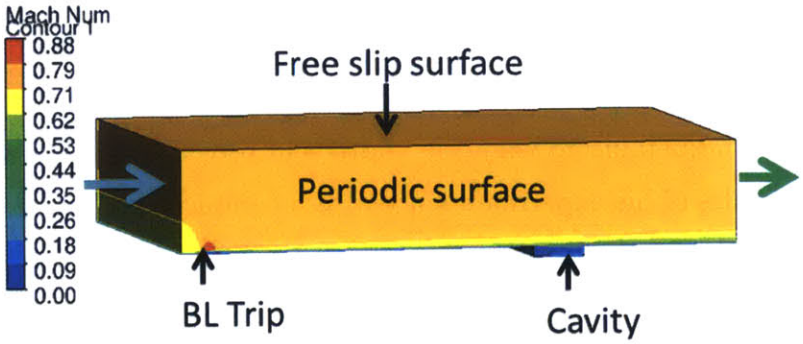

(b) Canonical Rectangular Cavity Computational Model

Figure 4.1: (a) Experimental setup of Krishnamurty [18]
(b) Computational model setup with boundary layer trip

To assess the effects of rig conditions, two studies were performed. One set of computations assessed the effect of mass flow injection into the cavity. This was implemented by imposing a mass flowrate boundary condition at the bottom surface of the cavity. A separate set of computations assessed the effect of tangential flow across the cavity. Several flow angles were modeled while keeping the axial component of velocity constant. Figure 4.2 shows the range of parameters that were assessed.

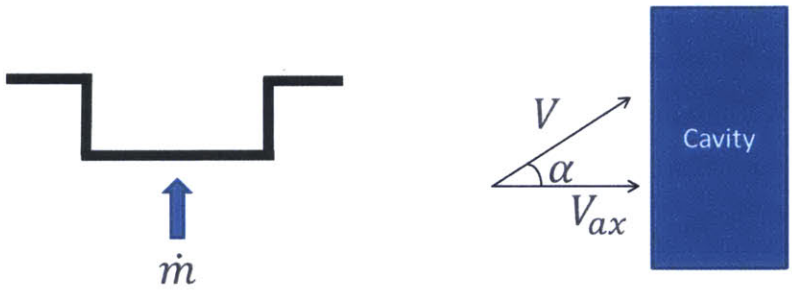

Blowing Ratio	Purge Flow Rate
0.35	0.8%
0.61	1.6%
0.88	3.2%

Flow Angle
0°
15°
30°
45°
60°

Figure 4.2: Parameters varied for computational model test configuration studies.

Before performing these studies, an assessment is performed to determine if key results from the experiments are reproducible in the computations. This assessment is described next.

4.3 Assessment of CFD results of canonical case compared to experiment

The computational model was formulated based on CFX 14.5 and consists of 4 million nodes and elements. The turbulence intensity and eddy viscosity ratio were set to 0.05 and 100, respectively. The boundary conditions were set as a stagnation pressure specified at the inlet, average static pressure at the outlet, free slip upper wall, and periodic boundaries as shown in Figure 4.1. For all computations, the model used a steady state solution as an ini-

tial condition for the time-accurate (unsteady) simulation. The unsteady results then served as the initial conditions for the next unsteady simulation with a different parameter or condition (higher mass injection flow rate or main flow angle). The unsteady solution was run with a 1E-6 timestep. A timestep sensitivity study was performed to consider larger timestep size but showed a timestep of 1E-5 was unable to capture the modes identified in the experiment. For all cases, convergence was determined when post-processing of subsequent timesteps yielded the same response frequency. Convergence was typically found within 50000 timesteps, which corresponds to 50 milliseconds. This is 1000 times larger than the 0.05 millisecond convective time for the primary flow over the cavity.

Table 4.1 compares relevant non-dimensional and aerodynamic parameters between the experimental setup and computational model.

	Experimental	Computational
M_∞	0.75	0.75
AR	0.2-0.5	0.2, 0.5, 1.44
$\frac{P_t - P_s}{\frac{1}{2}\rho_\infty U_\infty^2}$	1.17	1.17

Table 4.1: Comparison of non-dimensional parameters between the experimental setup and computational model for Shallow Cavity mode study.

4.3.1 Turbulent and Laminar Boundary Layer Assessment

For the initial unsteady calculation with 0° flow angle in the primary stream (i.e. axial flow with no tangential velocity) and no cavity throughflow, the frequency response of a probe located in the computational domain was determined. We will refer to this flow configuration as the baseline configuration. The experiments by Krishnamurthy included both the laminar and the turbulent boundary layer flow. The turbulent boundary layer was created by introducing a trip far upstream of the cavity. Both cases were modeled computationally – the laminar case was modeled without the use of a turbulence model while the turbulent case included a turbulence model as well as geometric representation of the trip.

The computed flow field for the baseline turbulent boundary layer configuration is shown in Figure 4.3. Also indicated in the figure is the location of the probe at which the

computed results were interrogated. This probe is placed at the same location from which measurements were recorded in Krishnamurty's experiments. A Fast Fourier Transform of the CFD model probe was performed using the pressure output at 1000 kHz.

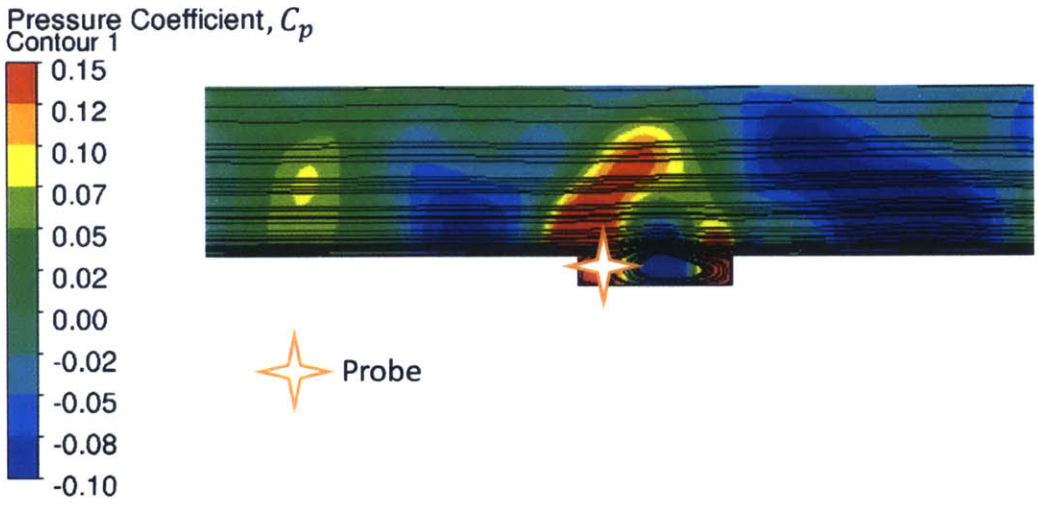

(a)

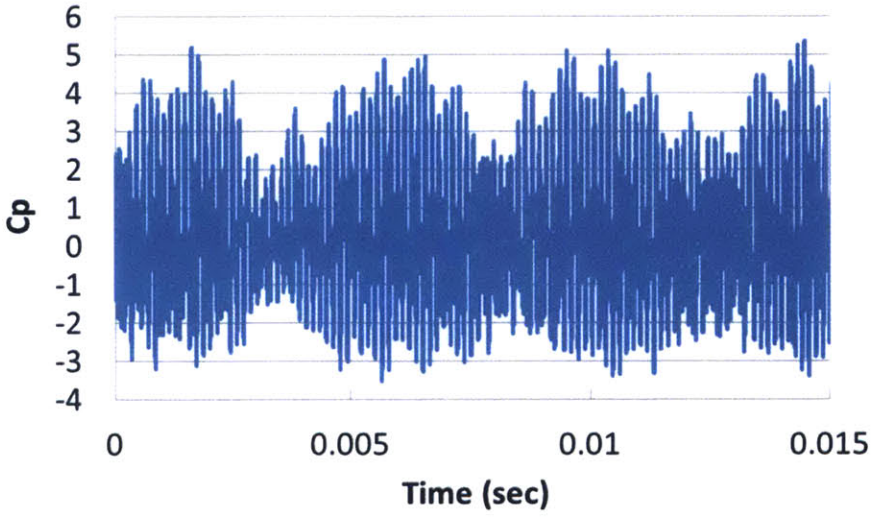

(b)

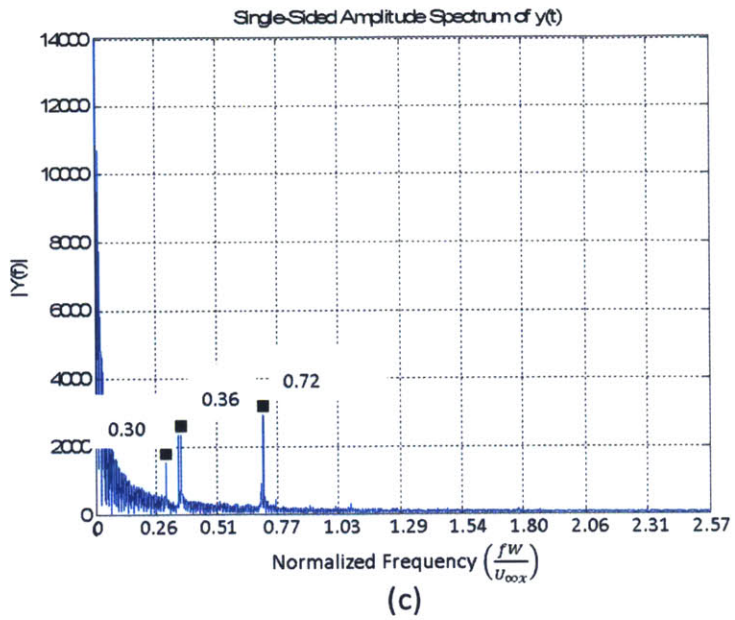

Figure 4.3: (a) Representative computed flow for the situation of a turbulent boundary layer demonstrating the instantaneous flow pattern and corresponding pressure coefficient contour, $C_p = \frac{P_s - P_{s\infty}}{\frac{1}{2}\rho_\infty U_\infty^2}$. The pressure field is monitored at the probe location.
(b) A representative pressure change with time at the probe location.
(c) Power spectrum of the pressure time series over 15000 timesteps (15 milliseconds) showing presence of distinct acoustic modes.

The pressure coefficient contour of the flow field in Figure 4.3(a) shows that there is a periodic structure to the flow upstream of the cavity. This periodic structure intensifies as the vortex forms in the cavity. The streamlines show the primary vortex that fills the domain of the cavity.

In the time history plot of pressure at the probe location in Figure 4.3(b), a low-order and higher-order mode can be identified in the oscillations. These two modes appear in a power spectrum analysis in Figure 4.3(c). For this case, the low-order mode appears to be split between two adjacent reduced frequencies: 0.30 and 0.36.

The computed frequency responses are shown in Figure 4.4 for the turbulent boundary layer and Figure 4.5 for the laminar boundary layer for assessment against the experimental results. For each of the figures, the ordinate is the measured/computed frequency while the abscissa is the cavity aspect ratio.

For the situation with a turbulent boundary layer in Figure 4.4, two dominant frequencies were identified in the experiments. The computed flow in the cavity also shows the ex-

istence of these two frequencies. The results in Figure 4.4 show that the computed cavity modes are in accord with the two modes experimentally determined by Krishnamurthy.

For the laminar case in Figure 4.5, the experiment identified only one dominant frequency. The computational model captured two frequencies: the dominant frequency also identified in the experiments and an additional lower-order mode not present in the experimental measurements. Walls were added to the current periodic boundary in the model in an attempt to mitigate the lower-order mode, but it was not successful: the same lower-order mode remained.

The cavity flow with the turbulent boundary layer can be considered as representative of the conditions encountered in a gas turbine engine environment. The agreement between the computational model and the experiment implies that the computational model has the required attributes for carrying out additional parametric assessment of flow response on the cavity. The parameters to be assessed for their impact on the cavity flow behavior include aspect ratio, mass injection (i.e. $\frac{\dot{m}_c}{\dot{m}_\infty}$), and tangential flow (i.e. $\frac{u_{\infty\theta}}{u_{\infty x}}$).

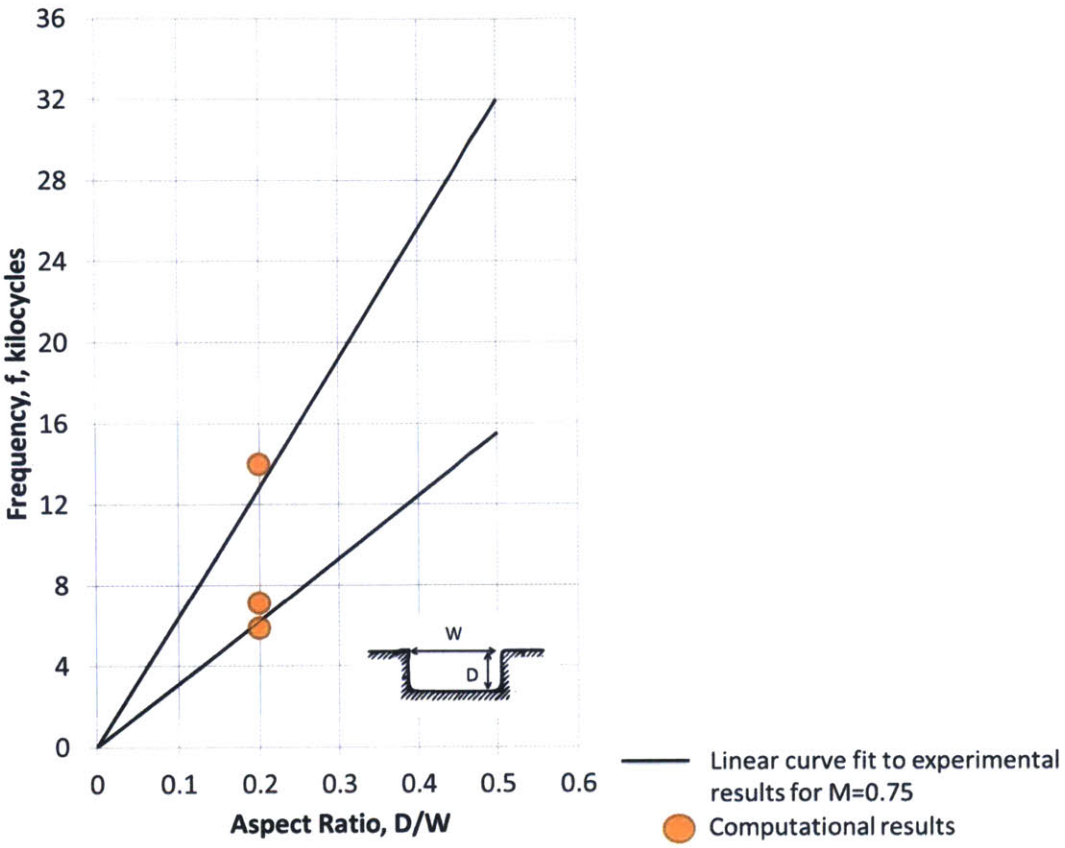

Figure 4.4: Calculated baseline shallow cavity response versus experimental measurements by Krishnamurty [18] for a turbulent boundary layer show good agreement.

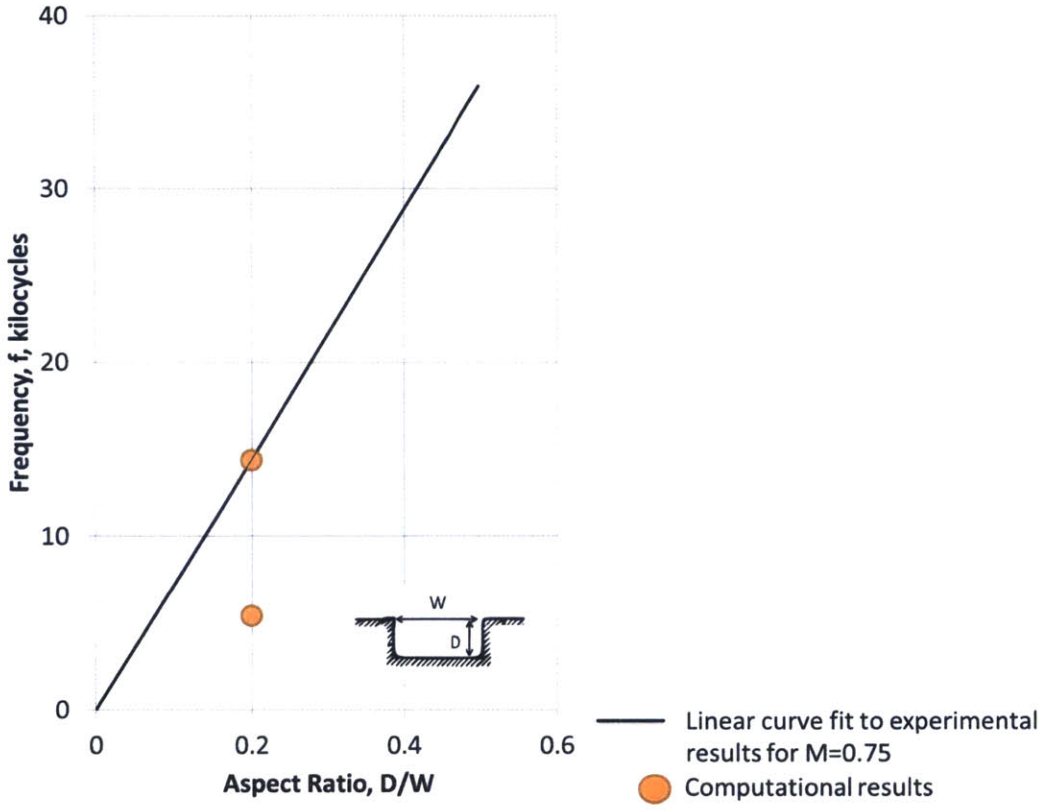

Figure 4.5: Calculated baseline shallow cavity response versus experimental measurements by Krishnamurty [18] for a laminar boundary layer show good agreement for the higher order mode. The computational results show a lower order mode not present in the experiment.

4.3.2 Cavity Aspect Ratio Assessment

The experiments by Krishnamurty were performed for a range of cavity aspect ratios. For the baseline width-to-depth ratio of 0.2, the computed cavity mode response is in agreement with those from the experiment. To assess the capability of the computational model, the shallow cavity mode response in a cavity with an aspect ratio of 0.5 was determined. The results from this set of computations are shown in Figure 4.6 for assessing against the experimentally measured values. As shown, the model does capture the primary low frequency shallow cavity mode but does not capture the higher-order mode. The same number of grid points was used for both the 0.2 and 0.5 aspect ratio geometries. Therefore, the 0.5 aspect ratio grid density was less than that for the 0.2 aspect ratio. The lower grid density

may have been too coarse to capture the higher order modes that were captured in the 0.2 aspect ratio model.

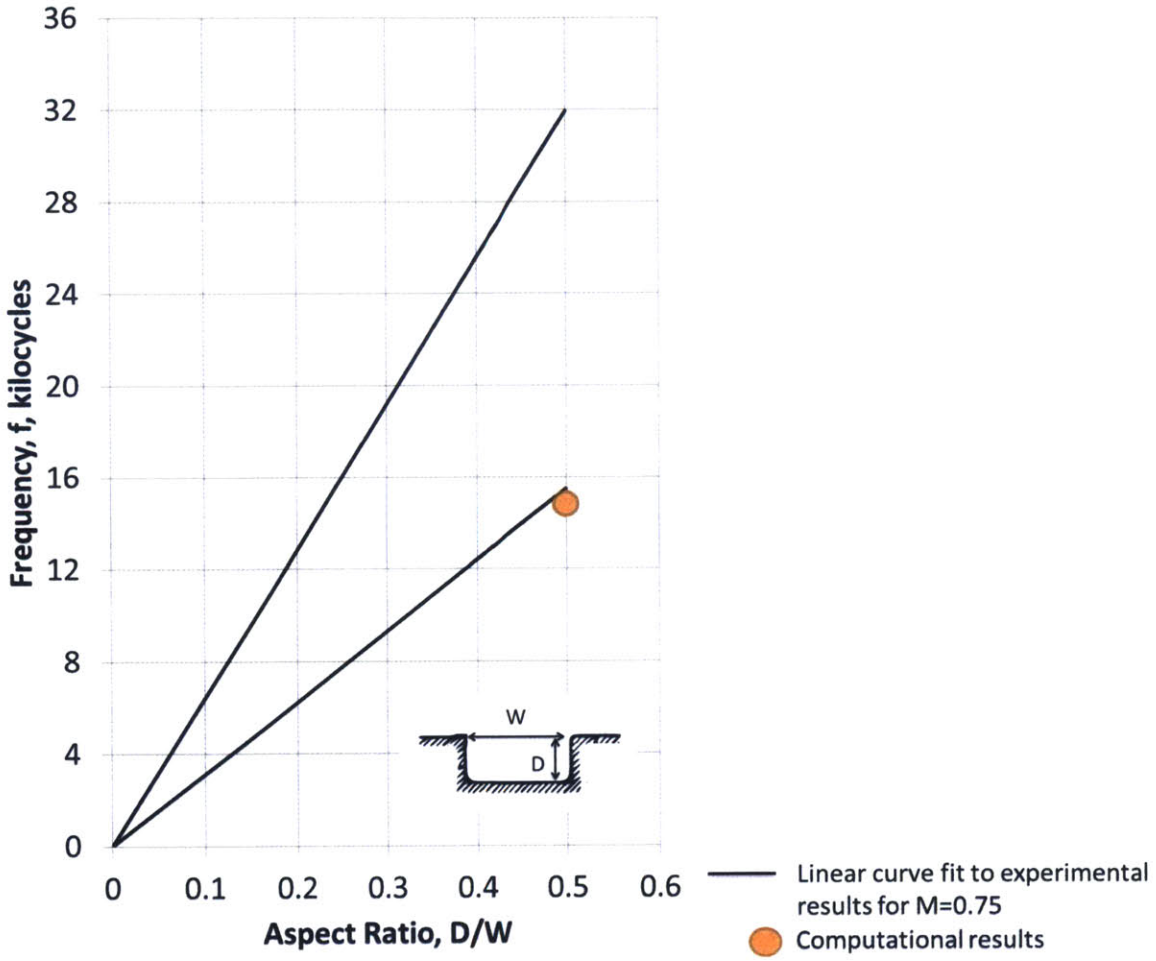

Figure 4.6: Calculated medium depth shallow cavity response versus experimental measurements by Krishnamurty [18] layer shows good agreement for the lower order mode. The computational results do not capture the higher order mode present in the experiment.

Although the Krishnamurty experiments did not include a cavity configuration with cavity aspect depth-to-width ratios greater than 0.5, a cavity with an aspect ratio of 1.44 is more representative of the trench cavity in the HGIR. Thus, there is a need to determine the effect on frequency of such a larger aspect ratio. Such a set of computations on flow in a cavity of aspect ratio 1.44 has been completed. The dominant frequency extracted from the computed results for this cavity with high aspect ratio is shown in Figure 4.7. The frequency no longer follows the linear trend for the cavity of lower aspect ratios less than 0.5. It is

suggested that the mode has transitioned from a shallow cavity mode to a deep cavity mode.

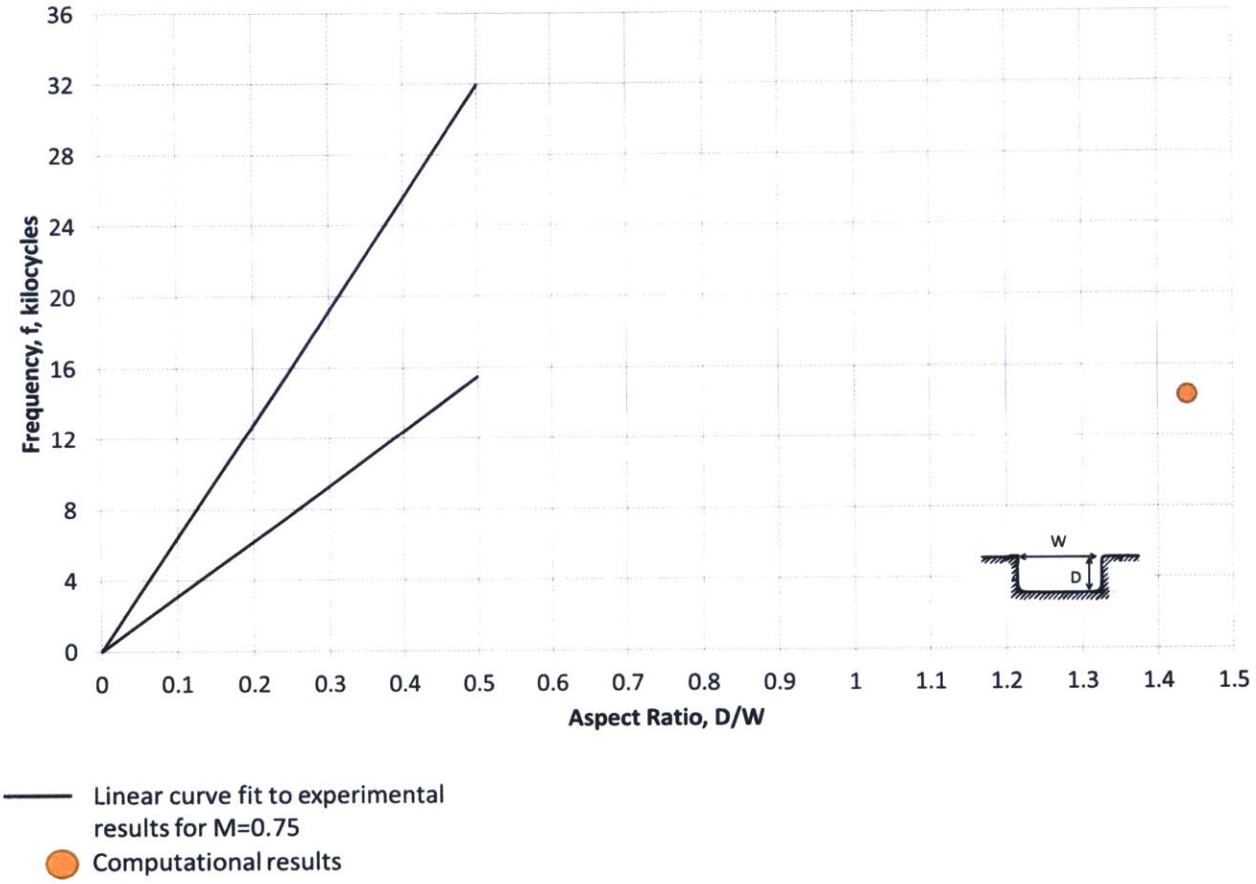

Figure 4.7: Calculated shallow cavity response for deep cavity versus experimental measurements by Krishnamurty [18]. The frequency appears to be a similar value to the medium depth cavity. Only one frequency mode is captured.

Figure 4.8 shows the instantaneous streamline pattern for cavity flow of different depths (but same width, thus varying cavity aspect ratio). For all cases, these streamlines show a primary vortex that appears in the cavity and grows to occupy the available size of the cavity. For the two lower aspect ratio situations, a secondary vortex is also present in the cavity. The baseline configuration appears to have the strongest pressure gradient across the cavity, with the lowest pressure at the center. The pressure field changes as the cavity depth increases. For the medium depth cavity, the low pressure zone is shifted to the aft side of the cavity. The deep cavity has a periodic structure similar to the baseline cavity, but with the highest pressure at the center.

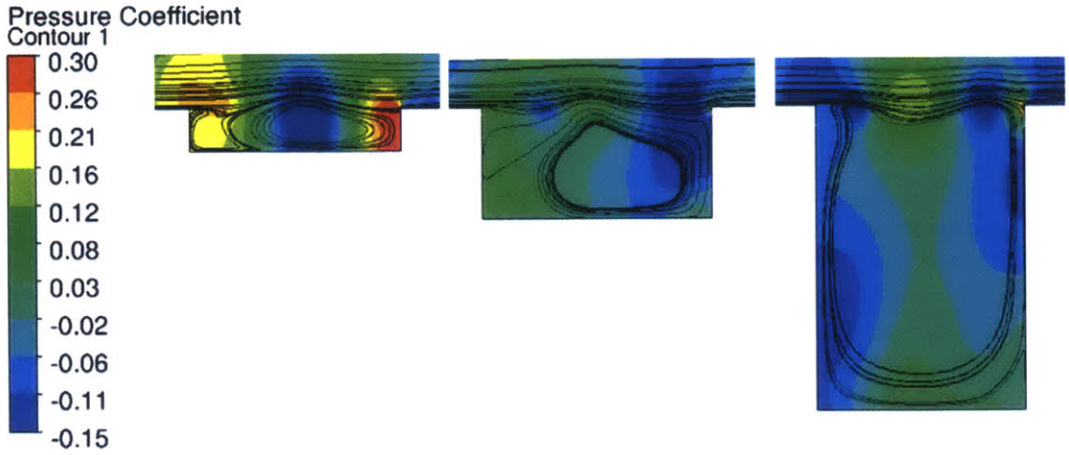

Figure 4.8: Streamlines for baseline, medium depth, and deep cavities. A primary vortex emerges for each configuration that fills the cavity volume. The pressure coefficient, $C_p = \frac{P_s - P_{s\infty}}{\frac{1}{2}\rho_\infty U_\infty^2}$, has greater variation in the shorter cavity than in the deeper cavities.

East [20] studied canonical deep cavity modes and evaluated the effect of cavity aspect ratio on the frequency of the deep cavity mode. Figure 4.9 shows the results of his experiments which indicate the discrete first and second modes that appear for different cavity depths.

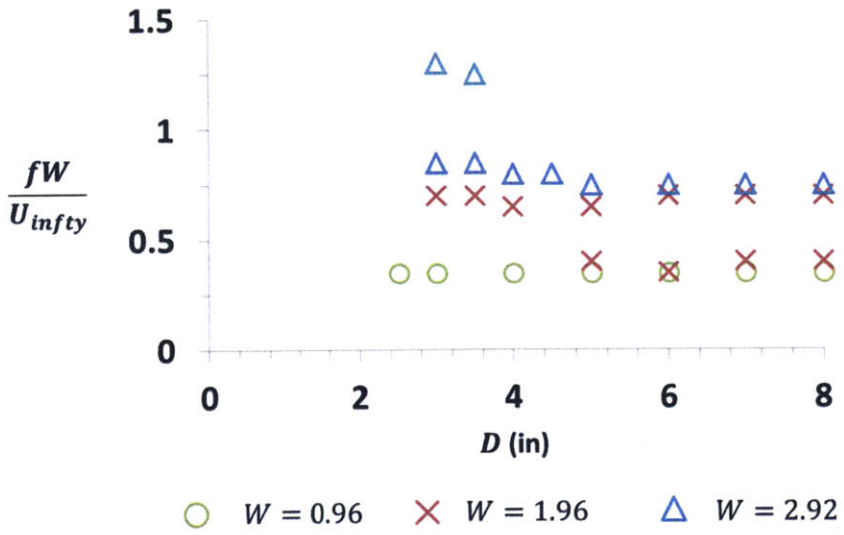

Figure 4.9: Plot of Strouhal number against cavity depth for deep cavity resonant conditions. Data from East [20]. Nearly-constant reduced frequency exists at each cavity width.

It is instructive to now reexamine the experimental results of Krishnamurty and East as well as the present computational results on a holistic basis. To do so, we need to recast all the results based on an identical set of non-dimensional parameters. Furthermore, it would also be useful to cast the results in terms of two forms of reduced frequency: one based on the cavity width and the other based on the cavity depth.

Figure 4.10 shows the reduced frequency based on cavity width versus aspect ratio for the results from Krishnamurty's, East, and the computational model. The velocity of the primary flowstream is used for the reduced frequency calculation. The first observation is that the reduced frequency trend based on cavity width is consistent between the shallow cavity frequencies of Krishnamurty and the deep cavity frequencies of East.

The next observation is that the CFD model appears to be capturing the 1st mode for aspect ratio of 0.2, but transitions to capturing 2nd mode as the depth is increased. There is a transition that occurs at a discrete cavity depth. Based on the current available computed results, it cannot be inferred with certainty if this transition is to a new cavity mode (from shallow to deep) or simply to a higher-order mode (remaining as a shallow cavity mode).

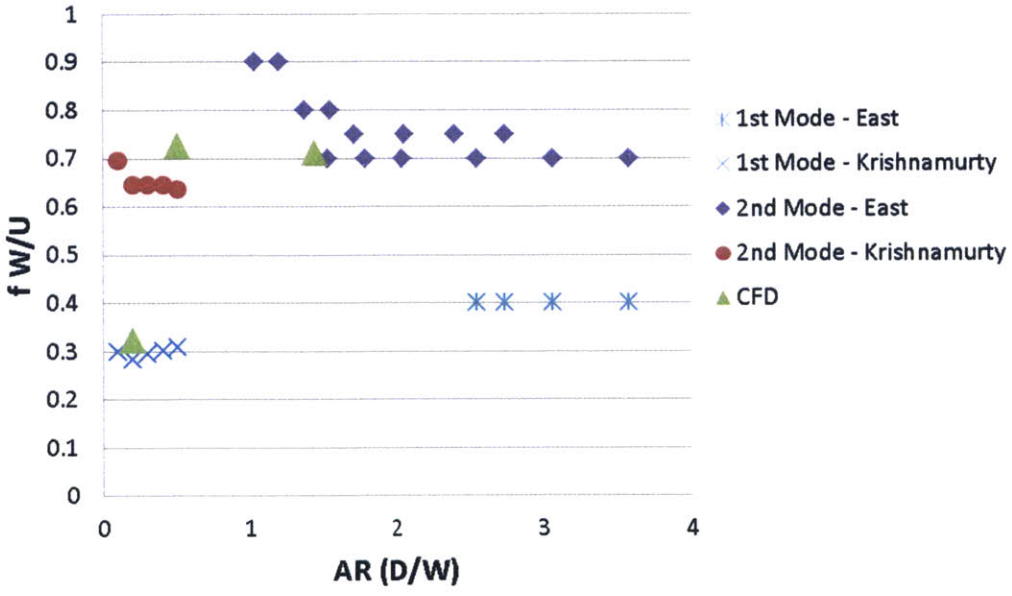

Figure 4.10: Reduced frequency based on cavity width for Krishnamurty and East results for Shallow and Deep Cavity modes compared to CFD results. 1st and 2nd mode have consistent trends between shallow and deep cavity modes.

Figure 4.11 shows the reduced frequency based on cavity depth versus aspect ratio. The velocity of the primary flowstream is used for the reduced frequency calculation.

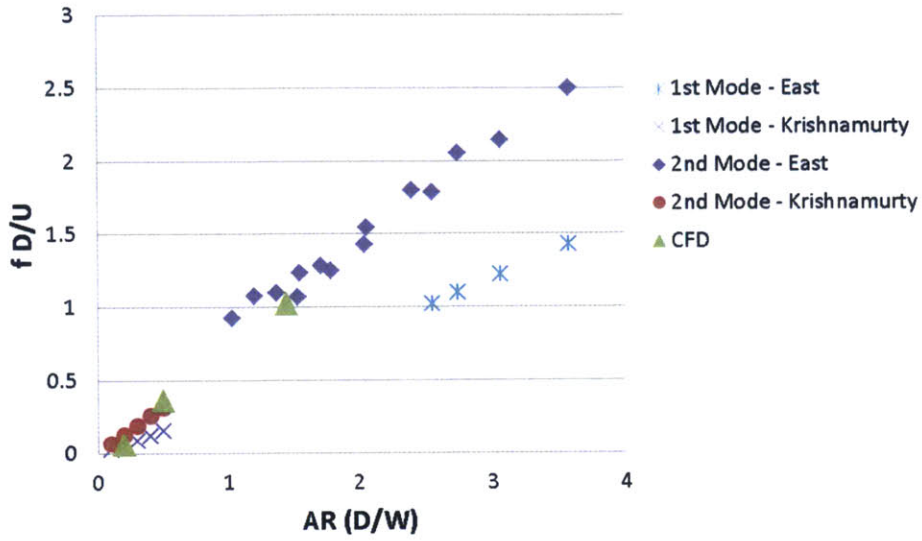

Figure 4.11: Reduced frequency based on cavity depth for Krishnamurty and East results for shallow and deep cavity modes compared to CFD results. 1st and 2nd mode reduced frequencies have consistent trends between shallow and deep cavity modes.

The first observation is that the reduced frequency trend based on cavity depth is linear and is consistent between the shallow cavity modes of Krishnamurty and the deep cavity modes of East. As before, the next observation is that the CFD model appears to be capturing the 1st mode for aspect ratio of 0.2, but transitions to capturing 2nd mode as the depth is increased.

In summary, with the limited set of computations, the observation is that the computed reduced frequency trend appears to follow the experimental trend. It would thus be inferred that the current computed results capture the cavity modes even for the higher aspect ratio situation.

4.4 Adequacy of Grid Resolution

A grid sensitivity study has been performed by scaling the domain up and down by a factor of 2. Scaling the domain changes the size of the geometry and expands or contracts the grid for that geometry. For these cases, the grid density is scaled down and up by a factor of

two, respectively. An assessment of the flow parameters shows that the ratio of momentum thickness to cavity dimensions remains constant between the scaled models. Table 4.2 details the Courant number, momentum thickness-to-cavity dimension ratios, and shape factor for each case.

	0.5X	**Baseline**	**2X**
Courant #	1.2	0.6	0.3
θ/W	0.016	0.020	0.018
θ/D	0.08	0.1	0.09
H	1.57	1.50	1.56

Table 4.2: Flow details for baseline and scaled domain models. Flow parameters are consistent between scaled models.

The power spectrum for each model is shown in Figure 4.12. The frequencies are presented as a reduced frequency using the width of the cavity as the length scale and the velocity of the main flow as the velocity scale. The reduced frequency is consistent between the baseline and scaled 2X cases. Between the 2X and baseline case, the low frequency is split into a pair of similar frequencies. The reduced frequencies for the scaled 0.5X case are similar to the baseline and 2X cases as well. Between the baseline and 0.5X case, the primary frequency amplitude is within 3%. Based on the results of this study, the grid size is determined to be sufficient for computing unsteady cavity flows in the configurations considered here.

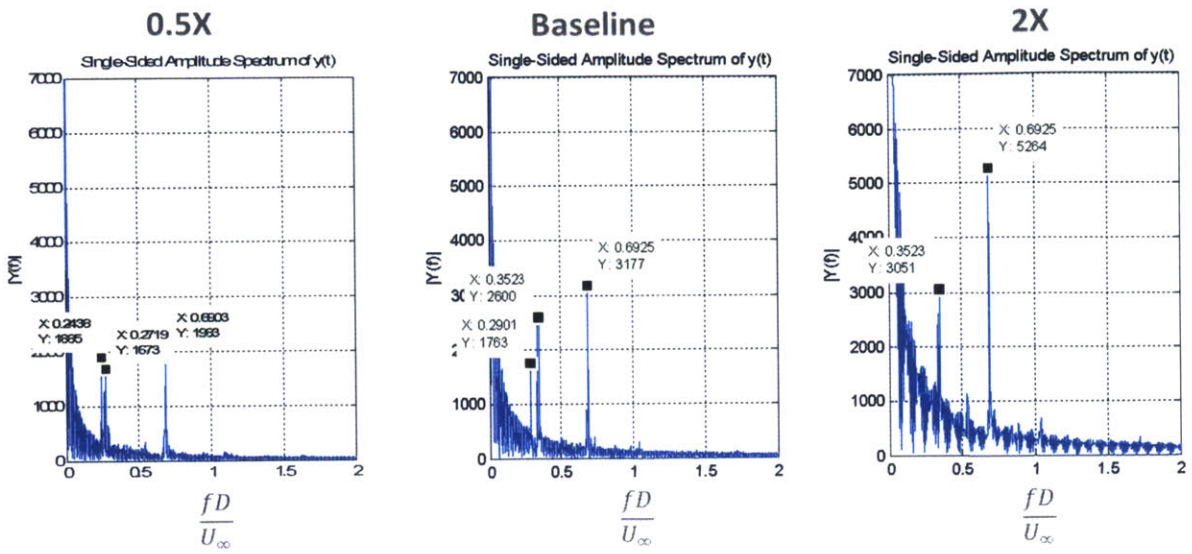

Figure 4.12: Power spectrum of baseline and scaled domain models normalized as a reduced frequency. Results comparison between the models concludes that grid density for the baseline model is sufficient.

4.5 Assessment of HGIR Conditions on Frequency of Shallow Cavity Mode

The operating conditions of the HGIR introduce complexities that are not present in the canonical rectangular cavity configuration for the determination of the various cavity modes. Two important characteristics are the presence of a mass flow injection (the purge flow through the cavity) and a tangential velocity component of the flow moving across the top of the cavity. The impact of these two characteristics on the shallow cavity mode is investigated computationally using the computational model for the cavity flow with a turbulent boundary layer. The effects of tangential velocity assessment is performed on the baseline cavity with an aspect ratio of 0.2 in order to isolate the effects of only modifying the tangential velocity component. The effect of mass injection assessment is performed on the cavity with an aspect ratio of 1.44 in order to reflect the interaction of primary and injected flows representative of a gas turbine engine.

4.5.1 Mass Injection Assessment

The first study assesses the role of mass injection into the trench cavity on the cavity flow response. Existing studies of Shallow Cavity mode assumes flow over a cavity with a solid wall. However, in a gas turbine there is a purge flow through the cavity to prevent the ingestion of hot gas flowpath air. The injection of mass flow into the cavity is hypothesized to attenuate the shallow cavity mode (i.e. to reduce the receptivity) due to the disturbance the additional mass flow would have on the unsteady shear layer. This hypothesis is assessed by varying the purge flow levels in the model followed by interrogation of the computational results.

The deep cavity modeled in Section 4.3.2 is used as the baseline for this study. Three levels of cavity purge flow are used that match the Mach number of the cavity flow through the HGIR trench cavity for purge flow levels 0.8%, 1.6%, and 3.2% of the main gaspath flow. The blowing ratios for these three cases, described in Section 2.7 , are 0.35, 0.61, and 0.88 respectively.

The reduced frequency versus blowing ratio for the cases studied is shown in Figure 4.13. Although there is only one dominant frequency present for the deep cavity with no mass flow injection, another dominant frequency appears for blowing ratios of 0.35 and 0.61. Blowing ratios at 0 and 0.88 only yield the second mode.

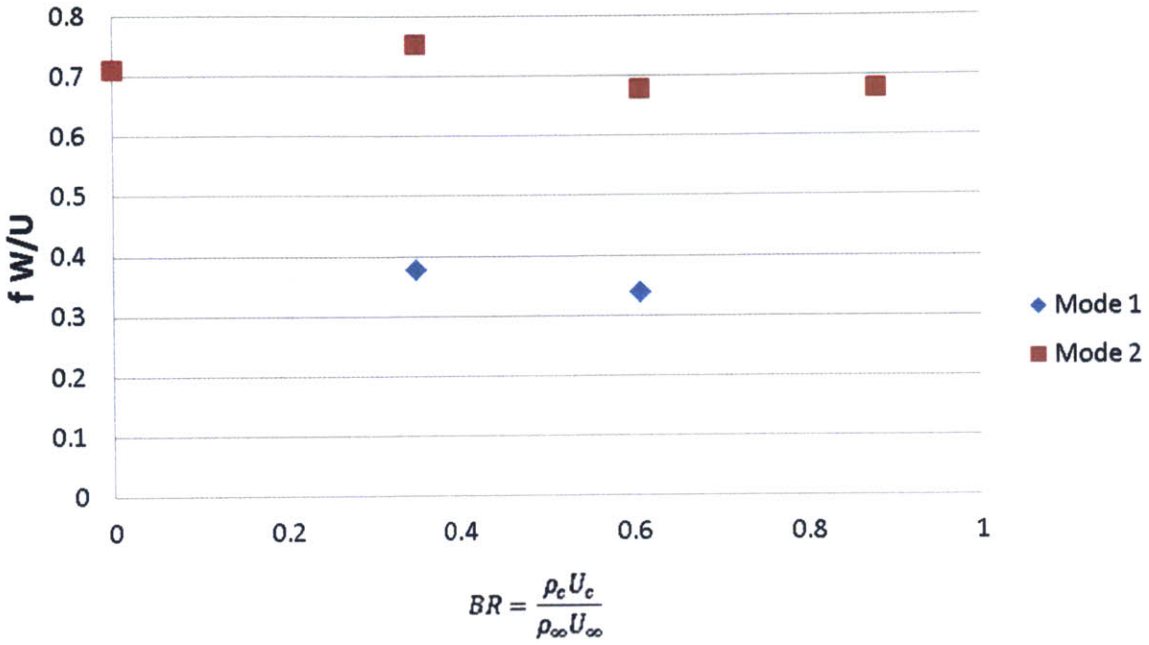

Figure 4.13: Effect of cavity purge flow on frequency response based on CFD results. Reduced frequency based on cavity width is shown versus blowing ratio. Frequency remains essentially invariant with blowing ratio. 1st mode only appears for two blowing ratios and does not appear for the others.

Figure 4.14 details the change in amplitude for both modes at each of the blowing ratios. For both Modes 1 and 2, a clear trend emerges that demonstrates the amplitude of the unsteady pressure field caused by the shallow cavity mode decays as the purge flow fraction introduced is increased. Again, for blowing ratios 0 and 0.88, only Mode 2 is present.

In Figure 4.15, the instantaneous flow field of the cavity is shown for the baseline deep cavity with three levels of purge flow. The progression of added purge flow exhibits a shift from a single vortex filling the cavity, to a single vortex that is confined to the outer third of the cavity, to one that is purged out of the cavity as inferred from the streamline pattern.

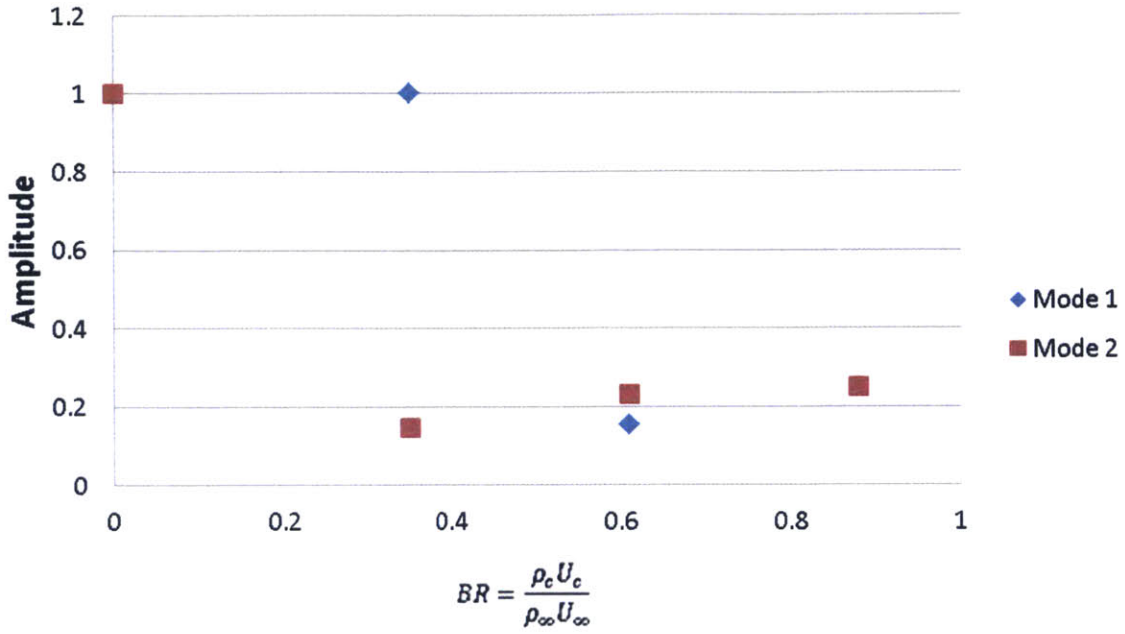

Figure 4.14: Effect of cavity purge flow on frequency response amplitude based on CFD results. Relative amplitude, normalized to the maximum amplitude of the studied cases is plotted against blowing ratio. There is a clear trend of decreasing amplitude with increased blowing ratio.

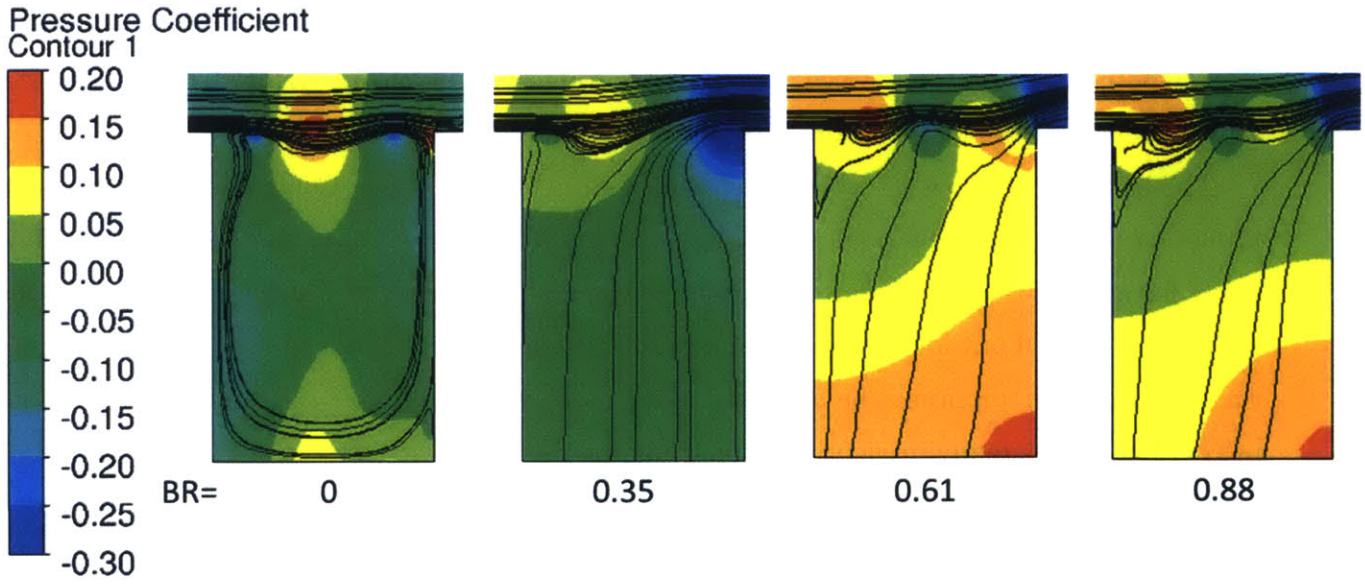

Figure 4.15: Effect of cavity purge flow on flow field in cavity. Streamlines are presented along with contours of the pressure coefficient, $C_p = \frac{P_s - P_{s\infty}}{\frac{1}{2}\rho_\infty U_\infty^2}$. The single vortex in the cavity is visibly being pushed out of the cavity when purge flow is added with a blowing ratio of 0.35. At higher blowing ratios, the flow exiting the cavity does not allow a vortex to form. The unsteadiness in the shear layer continues to be present.

It can be inferred from these computed results, though somewhat limited, that the mass flow injection into the cavity does have an effect on the shallow cavity mode. The frequency remains nearly constant for increased purge flow, but the response appears to significantly decrease, which can be the result of the increasing purge flow dislodging the vortex out of the cavity. The implication is that unsteady pressure fluctuations resulting from the Shallow Cavity mode response can be mitigated by purge flow in a turbine rim-cavity. It is of engineering significance to assess the minimum requirements of purge flow to eliminate this pressure unsteadiness (as reducing the purge flow level for improved turbine performance may result in the emergence of modes that promote ingestion).

4.5.2 Tangential Velocity Component Assessment

The effects of a tangential velocity component in the main gaspath on cavity flow response is presented in this section. Existing studies of shallow cavity mode are for situations where the flow moves axially over the cavity. However, in a gas turbine there is a tangential component of the velocity in the main gas flowpath as a result of the upstream nozzle guide vane. The flow angle, or ratio of tangential to axial velocity of the primary flow, across the cavity is hypothesized to have no effect on the shallow cavity mode frequency. This hypothesis is assessed by varying the incoming flow angle (see Figure 4.1) in the model followed by interrogating the computational results.

The baseline shallow cavity with an aspect ratio of 0.2 is used. Computations have been implemented for four flow angles: 15°, 30°, 45°, and 60°. The reduced frequency versus flow angle for each of these four flow situations is shown in Figure 4.16. Although computations have been carried out for flow angles up to 60°, it was observed that above 45°, the tangential flow acted to suppress the shallow cavity mode with negligible response, i.e. there appears to be no unsteady pressure response for the 60° case.

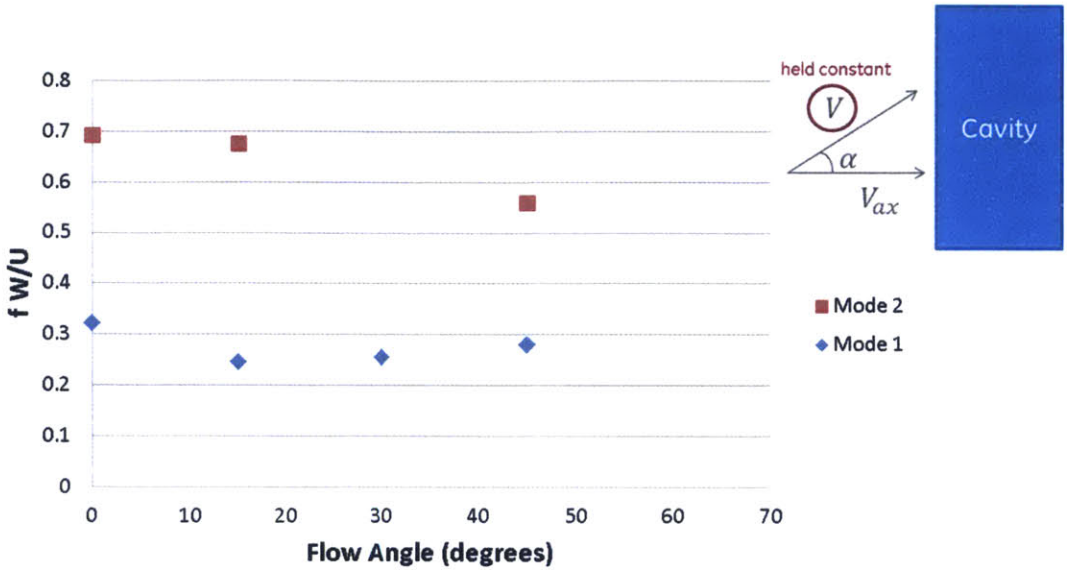

Figure 4.16: Effect of flow angle on frequency response based on CFD results. Reduced frequency based on cavity width is shown versus flow angle. Frequency remains essentially invariant, but at 60°, there is a cut-off where no response is present.

In Figure 4.17, the computed flow field of the cavity is shown for the baseline cavity flow for four different flow angles in the main gas flowpath. Increasing the flow angle results in a reduction of pressure non-uniformity until it is uniform.

To further investigate the effects of the increasing the main flow angle, a cut is made down the middle of the cavity on which the pressure field and tangential velocity vectors are shown in Figure 4.18. Most notable in the observations of these results is that, although there is no tangential flow for the 0° flow angle case, the presence of a modal disturbance can be inferred. As the flow angle is increased, this pressure non-uniformity is attenuated. Beyond a flow angle of 45°, the pressure field is nearly uniform. This result is consistent with the frequency assessment that showed no unsteady pressure fluctuations for the highest flow angle of 60° assessed.

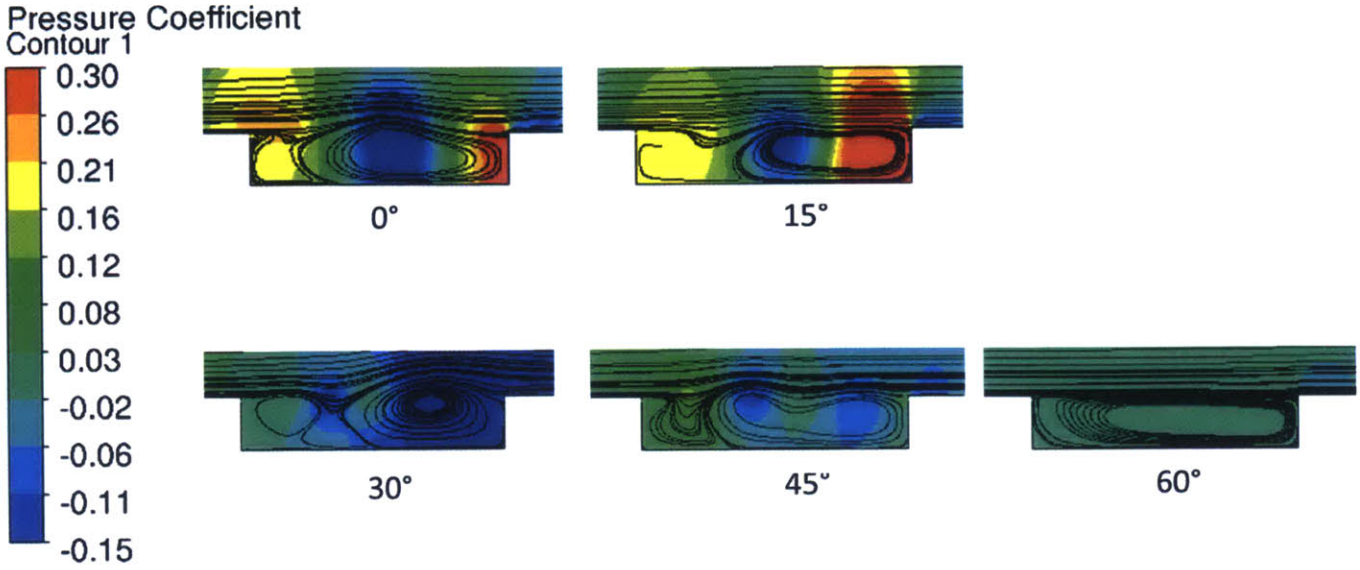

Figure 4.17: Effect of flow angle on flow field in cavity. Streamlines are presented along with contours of the pressure coefficient, $C_p = \frac{P_s - P_{s\infty}}{\frac{1}{2}\rho_\infty U_\infty^2}$. The single vortex expands lengthwise in the cavity as flow angle is increased, with no visible unsteadiness present for 60°.

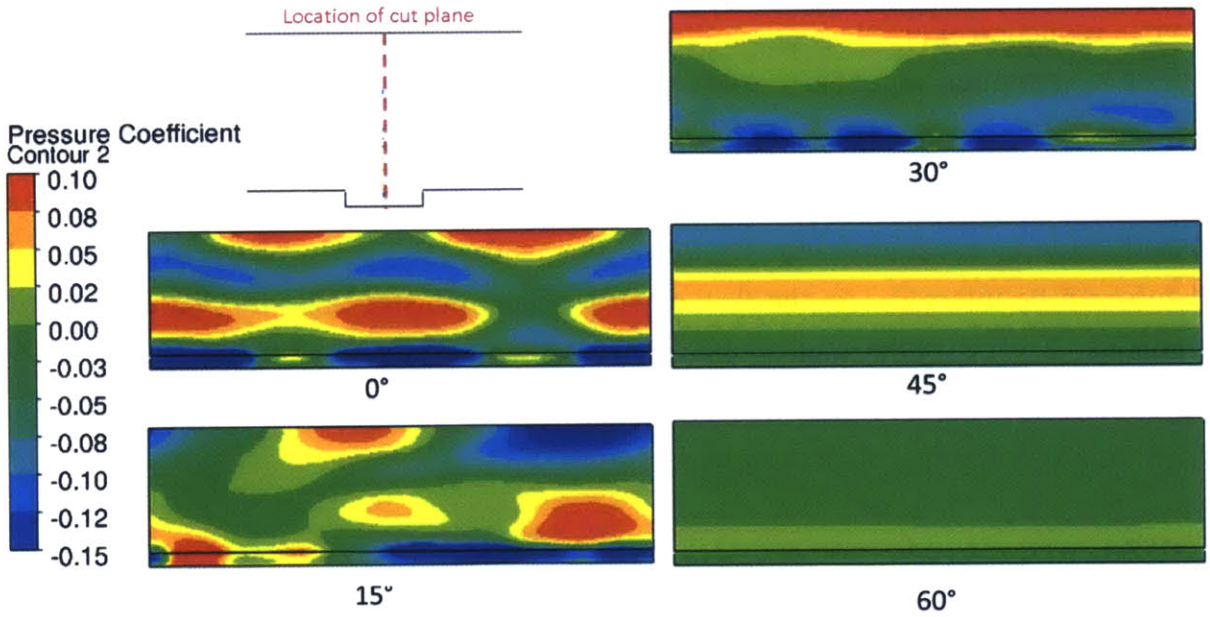

Figure 4.18: Effect of flow angle on pressure field in the cavity. Contours of the pressure coefficient, $C_p = \frac{P_s - P_{s\infty}}{\frac{1}{2}\rho_\infty U_\infty^2}$ are presented. Although the flow is entirely axial in the 0° case, there is tangential variation. As the flow angle is increased, this non-uniformity is reduced until there is complete uniformity for 60°.

The pressure field on several axial planes from upstream locations to within the cavity is examined for its development from upstream to downstream location. The solution of 0° flow angle with substantial static pressure non-uniformity is interrogated further as follows. Figure 4.19 shows the pressure field for the 0° flow angle at several locations upstream of the cavity. It appears that the non-uniform pressure field begins at the trip upstream of the cavity and strengthens as the flow approaches the cavity.

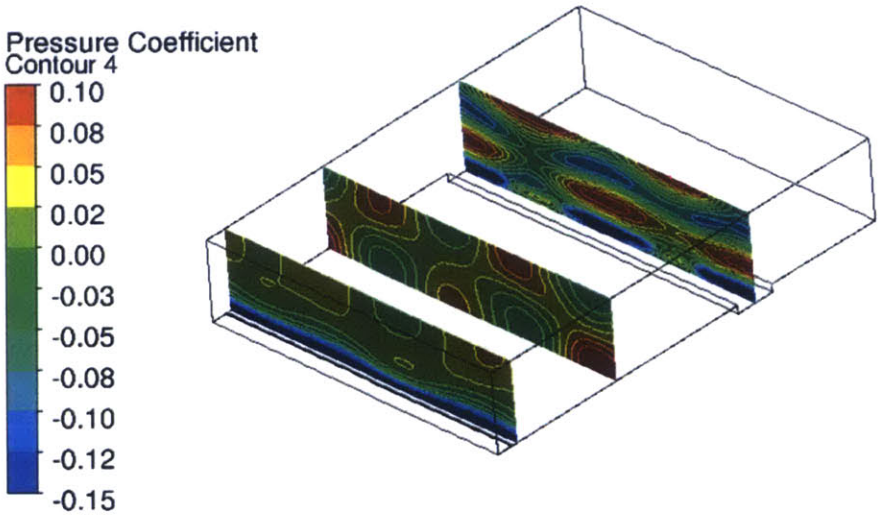

Figure 4.19: 0° flow angle pressure field upstream of and within the cavity. Contours are for the pressure coefficient, $C_p = \frac{P_s - P_{s\infty}}{\frac{1}{2}\rho_\infty U_\infty^2}$. Variation in the pressure field in the tangential direction is apparent after the boundary layer trip located at the inlet.

The unsteady pressure field is prominent not only at the cavity but also at the outer boundary. For this CFD model, the outer wall has been set as a free slip boundary condition. To assess whether this free slip boundary condition may be numerically inducing this variation, the model was run with the outer boundary as a no-slip solid wall. The results of this study, shown in Figure 4.20 , conclude that the non-uniform pressure field is present at the cavity even with the solid wall boundary condition. Therefore, the no-slip boundary condition is not the source of the static pressure modal disturbance.

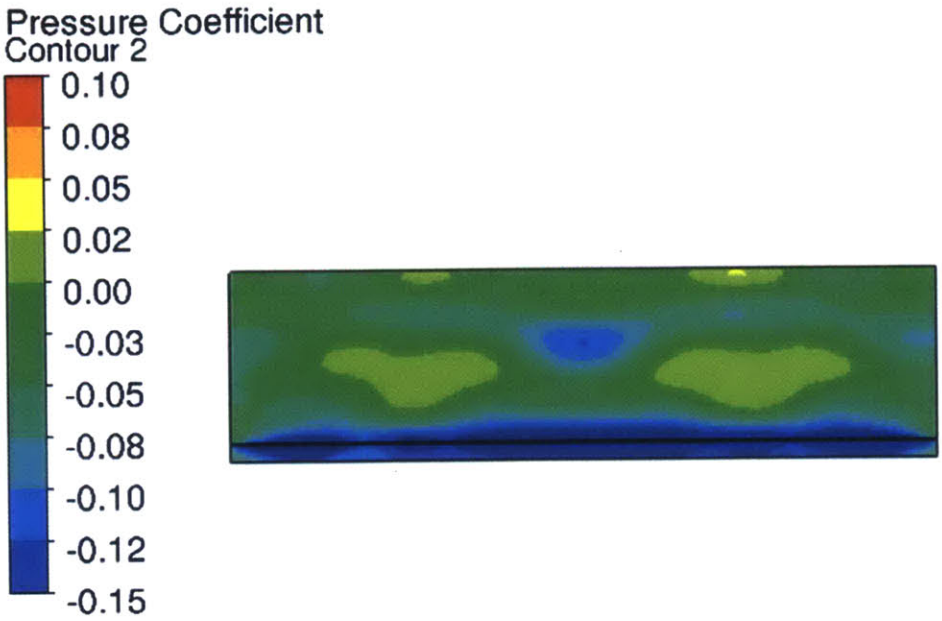

Figure 4.20: CFD domain modified with no-slip solid outer wall for 0° flow angle. Contours are of the pressure coefficient, $C_p = \frac{P_s - P_{s\infty}}{\frac{1}{2}\rho_\infty U_\infty^2}$ are plotted for a plane within the cavity. Tangential variation in the pressure field continues to be present in the cavity.

In summary, the flow angle of the main gas flowpath does have an effect on the shallow cavity mode. As the flow angle increases, the pressure field becomes more uniform and there is a cut-off between 45°and 60° where the unsteady pressure field is suppressed. The underlying rationale as to why this is so has not been sorted out yet. The implication of this observed result is that the swirl angle imparted on the main gas flowpath by the NGVs in a gas turbine may have a stabilizing effect on the Shallow Cavity response in the turbine-rim cavity.

4.6 Summary of Computational Results

In summary, the results from the computational assessment show the following:

1. There is good agreement between the computational model and experimental results for main flow Mach number of 0.75, aspect ratios of 0.2 and 0.5, and turbulent boundary layer induced by a trip upstream of the cavity.

2. There is a transition between Shallow Cavity and Deep Cavity mode as the aspect ratio of the cavity increases from 0.5 to 1.44 which was not identified in the HGIR data and should be further investigated.
3. Mass injection into the cavity suppresses the Shallow Cavity response, implying that the purge flow in a turbine rim-cavity provides a stabilizing effect on the response.
4. Increasing the flow angle (the ratio of tangential velocity component to axial velocity component) of the primary flow over the cavity provides a stabilizing effect on the Shallow Cavity response when the flow angle is greater than 45°. This implies that the swirl angle induced by the NGV in a gas turbine would also have a stabilizing effect on the response.

Chapter 5 Synthesizing Experimental and Computational Results

This chapter brings together the experimental and computational assessments of flow features in the turbine rim-seal cavity. A recap of the experimental results highlights the relevance to the central theme on the presence of cavity modes in the stator/rotor rim-seal cavity wheelspace system. The computational assessment is also addressed in terms of their importance to understanding cavity modes.

5.1 Integrating Experimental and Computational Results into the Central Theme

The central theme of this thesis is on the presence of cavity modes in the stator/rotor rim-seal cavity wheelspace system. The experimental data from the HGIR led to the conclusion that there are cavity modes present. Specifically, a Shallow Cavity mode is present in the trench cavity and a Helmholtz resonance is present in the buffer cavity. These modal responses are not affected by the rotational Reynolds number, the Shallow Cavity response amplitude is affected by purge flow ratio, and the effect of the response is not attenuated across the rim seals.

Computational assessment based on canonical cavity configurations show the presence of a primary vortex in the cavity and that one or two Shallow Cavity modes may be present for a given configuration. The assessments also indicated that increasing mass flow injection into the cavity reduces the amplitude of the response. This is in agreement with data from the HGIR for Shallow Cavity Mode 1, but in contrast to data from HGIR for Shallow Cavity Mode 2 which shows trench cavity modal response increasing with purge flow level. Tangential flow in the main flowpath also affects the response in that it acts to reduce the cavity-induced pressure non-uniformity and hence no Shallow Cavity response for a main gas flowpath with a flow angle beyond 45°. While no physical rationale has been put forward to explain this observation in the computed results, it is nevertheless an interesting observation that may have engineering implication on the design of the turbine rim-cavity system.

5.2 Connecting Results to Representative Engine Operating Conditions

In order to understand how the conclusions of the experimental and computational assessments can be linked to all wheelspace configurations, the results must be connected to the expectations at representative engine operating conditions. The HGIR was designed to operate at engine-matched conditions for an industrial gas turbine [16]. Therefore, the observations that the Shallow Cavity mode and the Helmholtz resonant mode are present in the rim-seal cavity of the HGIR would imply that these modes are also likely in operating industrial gas turbines for power generation.

There are two primary conclusions from the computational assessment that need to be linked to operating engines: those relating to mass flow injection and tangential flow component impact on the Shallow Cavity mode. For the mass injection study, the Mach number of the exiting purge flow was matched between the HGIR and the CFD model. Therefore, the Mach number and blowing ratio of the CFD model are representative of engine operating conditions. The three purge flows tested were equivalent to the HGIR gaspath mass flow purge levels of 0.8%, 1.6%, and 3.2%. The results of the computational model showed that the amplitude of the response decreased as additional mass flow injection was added. This is in agreement with the experimental findings that the Shallow Cavity Mode 1 amplitude decreases with increasing purge flow. However, the experimental data did not show a significant decrease in response amplitude for Mode 2 at the largest purge level of 3.2%. It is thus inferred that there could be other flow drivers that sustain the cavity mode in the HGIR – an obvious source would be the unsteady flow disturbances and the circumferentially varying pressure field in the main gas flowpath generated by the upstream NGV and downstream blade.

The effect of a tangential component of velocity on cavity mode response in a canonical configuration has been assessed for flow angle up to 60°. This value of flow angle is representative of that in an engine operating environment. The results of the computational model showed that beyond a flow angle of 45°, the Shallow Cavity mode response is absent. In the HGIR, the swirl angle of the flow exiting the upstream NGV is greater than 60°, but the Shallow Cavity mode is nevertheless identifiable. This observation again suggests that there could be other flow drivers in the main flowpath (external to the rim cavity) that is sustaining the cavity mode.

5.3 Summary

While the data from the HGIR and the canonical computational model of the cavity show the existence of cavity modes, the modal response to variation in the purge flow level and the swirl angle in the main flowpath is not identical. An implication is that the canonical computational model of the cavity flow may not have incorporated other flow processes present in the main gas flowpath of the HGIR; this could include the pressure non-uniformity and flow unsteadiness introduced by the NGV and blade interaction, as well as radial pressure gradient associated with streamline curvature in the main flow.

Despite the difference in the response of the cavity mode to mass flow injection and tangential flow angle between the HGIR data and results based on computational model of the canonical cavity, the turbine rim-cavity system can sustain the presence of cavity modes. The link between the presence of cavity modes and hot gas ingestion has not been established because of the lack in adequacy of data in CO_2 traces on the HGIR.

Chapter 6 Summary and Conclusion

In this chapter, a summary of this thesis is presented, the key findings are delineated, and suggestions are provided for future work on this topic.

6.1 Summary

The underlying research questions addressed in this thesis are to identify what sources of unsteadiness and acoustics are present in the wheelspace cavity. Both experimental and computational approaches were taken to assess the unsteady pressure field. Instrumentation from the Hot Gas Ingestion Rig (HGIR) at GE Global Research provided data that supports the presence of cavity modes in the stator/rotor wheelspace cavity. Computational studies of canonical cavity configurations provided insight into the flow field at the rim-seal cavity and the effects of engine operating conditions on the unsteadiness. The work has identified that cavity modes exist in the wheelspace and that there are specific engine operating conditions for purge flow levels and swirl angle that can suppress the response of these modes.

6.2 Key findings

The key findings of this thesis provide insight into unsteady pressure field at the stator/rotor rim-seal cavity wheelspace and the presence of cavity modes. These findings are as follows:

1. Cavity modes exist in the turbine rim-cavity wheelspace of a gas turbine. This is supported by experimental data on a test rig with turbine stage and wheelspace configuration representative of that on a gas turbine engine. Cavity modes identified in this work are the Shallow Cavity mode and Helmholtz resonance.
2. Computational modeling of canonical cavity flow suggests that increasing mass flow injection into the cavity (more precisely, increasing the ratio of injected mass flow rate to the main flow mass flow rate) reduces the amplitude of the response of Shallow Cavity modes. This is in agreement with data from the HGIR for Shallow Cavi-

ty Mode 1, but in contrast to data from HGIR for Shallow Cavity Mode 2 which shows trench cavity modal response increasing with purge flow level.

3. Computational modeling of canonical cavity flow suggests that increasing the primary flow tangential to axial velocity ratio mitigates the shallow cavity mode response, exhibiting a cut-off point where the response is no longer present for flow angle beyond 45°. Again this observation is in contrast to the HGIR data that show the modal response is present with a flow angle greater than 45°.
4. The implication of 2 and 3 in the computational assessment is that the purge flow and main gas flowpath swirl angle in a gas turbine provide a stabilizing effect on the cavity modal response.
5. Experimental requirements to capture the effects of cavity modes are identified along with inadequacies in the current rig set-up with the associated instrumentation system.
6. Because of 5, the role of cavity modes on hot gas ingestion cannot be clarified based on the current set of data.

6.3 Future Work

There are several threads of investigations worthwhile to pursue in further evaluating cavity modes in a stator/rotor wheelspace cavity. Below is a summary of the primary areas of study uncovered by the investigation in this thesis that would provide further insight.

1. Experimental Investigation
    a. Data acquisition on HGIR: A primary way to detect cavity modes in an operating engine environment is to acquire the data using unsteady pressure measurements on a functional rig set-up. The data acquired in the HGIR had several issues that clouded the ability to make clear judgments on the sources of all the responses extracted. It is highly recommended that adjustments are made to the data gathering procedure so that there is repeatability and reliability in the data. Additional instrumentation should also be added at other locations in the stator/rotor wheelspace cavity to enable identifying other modes that may be present and to enable measuring the attenu-

ation of the known cavity mode response in different regions of the wheelspace cavity.

b. Kulite measurements on HGIR: Current Kulite placement is a limitation in assessing the data for cavity modes. There are currently no Kulites in the inner wheelspace and the buffer cavity Kulites produce significant noise. Therefore, only Kulites in the trench cavity on the stator surface can be reliably assessed with the available data for most experiments. For future work, it is important to resolve flow unsteadiness in the buffer cavity and lower wheelspace to assess the attenuation of flowpath pressure unsteadiness as well as to determine other modes that are dominant in the buffer and wheelspace cavities that may impact ingestion.

c. Static pressure measurements on HGIR: The current instrumentation layout lacks the capability to resolve the axial evolution in circumferential variation away from the trailing edge. At the present time, static pressure taps in the trench could be used as a third data point to identify the trend. For future study, improved instrumentation of the rig should include additional static pressure taps. Because of the limited space behind the trailing edge, these pressure taps could be located at the outer band of the flowpath. Positioning the pressure taps at the outer band of the flowpath would also isolate them from the cavity purge flow to more clearly identify the unsteady pressure variation due to the upstream NGVs and downstream blade row.

d. Hot gas ingestion measurements on HGIR: Accurate, time-resolved gas concentration measurements are required to fully assess the impact of cavity modes on hot gas ingestion. Instrumentation that can provide the necessary level of detail should be added to the HGIR and assessed versus the Kulite data to determine what correlation may exist between the cavity modes and level of ingestion.

e. Experiments on HGIR: Upon obtaining a cleaner set of unsteady pressure measurement data, additional experiments should be carried out to further assess the presence of Shallow Cavity mode and Helmholtz resonance. Additional experiments should modify the trench and buffer cavity dimensions independently. The available data from the latest experiments investigating

the Shallow Cavity mode should also be further interrogated to arrive at answering why the data looks the way it does.

2. Computational Investigation
    a. Mass flow injection: There are several studies that could be performed using the computational model to further quantify the impact of engine operating conditions on the Shallow Cavity mode. It was found that increasing the purge flow did reduce the amplitude of the Shallow Cavity mode response. However, this was not observed for Shallow Cavity Mode 2 in the data. This leads to the conclusion that there are other factors (other than mass injection flow level or blowing ratio) that affect the amplitude. Additional flow factors should be investigated to determine what key flow features are required to reduce the amplitude of the response.
    b. Flow angle: Further investigation on the effect of flow angle on the unsteady pressure field should be pursued. Additional studies should be undertaken on the observed behavior of increased flow angle stabilizing the pressure field to verify that this result is not numerical in nature and that this result manifests itself in operating engine conditions. It would be useful to assess this finding via an experimental rig, where the flow angle can be varied on a canonical geometry to identify the effect of the flow angle.
    c. Other factors: Many engine-specific factors that may have an effect on the Shallow Cavity mode were not investigated but are listed here as recommended future work.
        i. Axisymmetric geometry rather than rectilinear cavity
        ii. Rotating turbine wheel wall
        iii. Curved disk walls rather than 90° corners
        iv. Presence of upstream NGVs and downstream turbine blades
    d. Helmholtz resonator: The studies performed on a canonical geometry for the Shallow Cavity mode would be equally beneficial to perform on a canonical geometry representing the Helmholtz resonator. Because the buffer cavity is expected to perform as a Helmholtz resonator, studies should be undertaken to determine how engine operating conditions may have an impact on such resonant phenomena and how that response may be mitigated.

Chapter 7 Bibliography

[1] J. L. Kerrebrock, Aircraft Engines and Gas Turbines (Second Edition), MIT Press, 1992.

[2] R. T. Balmer, Modern Engineering Thermodynamics, Burlington: Elsevier, 2011.

[3] B. Saracoglu, G. Paniagua and S. Salvadori, "Energy Analysis of Pulsating Coolant Ejection," in *Proceedings of ASME Turbo Expo 2014: Turbine Technical Conference and Exposition*, Dusseldorf, 2014.

[4] C. Soares, Gas Turbines - A Handbook of Air, Land and Sea Applications (2nd Edition), Oxford: Elsevier, 2015.

[5] S. Zhang and Z. Dongliang, Aerospace Materials Handbook, Boca Raton: CRC Press, 2012.

[6] M. Zlatinov, "Secondary Air Interaction with Main Flow in Axial Turbines," Massachusetts Institute of Technology, Cambridge, 2009.

[7] W. Daniels, B. Johnson, D. Graber and R. Martin, "Rim Seal Experiments and Analysis for Turbine Applications," *Journal of Turbomachinery,* vol. 114, pp. 426-432, 1992.

[8] T. Green and A. Turner, "Ingestion Into the Upstream Wheelspace of an Axial Turbine Stage," *Journal of Turbomachinery,* vol. 116, pp. 327-332, 1994.

[9] D. Bohn, B. Rudzinski, N. Surken and W. Garter, "Experimental and Numerical Investigation of the Influence of Rotor Blades on Hot Gas Ingestion Into the Upstream Cavity of an Axial Turbine Stage," *In Proceedings of ASME Turbo Expo 2000,* pp. 1-8, 2000.

[10] K. Teramachi, M. Hamabe, T. Manabe and N. Yanagidani, "Experimental and Numerical Investigation of Sealing Performance of Turbine Rim Seals," in *Proceedings of the International Gas Turbine Congress,* Tokyo, 2003.

[11] C. Sangan, J. Scobie, J. Owen, O. Pountney, M. Wilson and G. Lock, "Experimental Measurements of Ingestion Through Turbine Rim Seals, Part 3: Single and Double Seals," in *Proceedings of ASME Turbo Expo 2012*, Copenhagen, 2012.

[12] J. Balasubramanian, N. Junnarkar, D. Zhou, R. Roy, Y. Kim and H. Moon, "Experiments on Aft-Disk Cavity Ingestion in a Model 1.5-Stage Axial Flow Turbine,"

in *Proceedings of ASME Turbo Expo 2011*, Vancouver, 2011.

[13] D. Zhou, R. Roy, C. Wang and J. Glahn, "Main Gas Ingestion in a Turbine Stage for Three Rim Cavity Configurations," *Journal of Turbomachinery,* vol. 133, 2011.

[14] R. Roy, J. Feng, D. Narzary and R. Paolillo, "Experiment on Gas Ingestion Through Axial-Flow Turbine Rim Seals," *Journal of Engineering for Gas Turbines and Power,* vol. 127, pp. 573-582, 2005.

[15] M. Barringer, A. Coward, K. Clark, K. Thole, J. Schmitz, J. Wagner, M. Alvine, P. Burke and R. Dennis, "The Design of a Steady Aero Thermal Research Turbine (START) for Studying Secondary Flow Leakages and Airfoil Heat Transfer," in *Proceedings of ASME Turbo Expo 2014: Turbine Technical Conference and Exposition* , Dusseldorf, 2014.

[16] P. Palafox, Z. Ding, J. Bailey, T. Vanduser, K. Kirtley, K. Moore and R. Chupp, "A New 1-1/2 Stage Turbine Wheelspace Hot Gas Ingestion Rig (HGIR) - Part I: Experimental Test Vehicle, Measurement Capability and Baseline Results," in *Proceedings of ASME Turbo Expo 2013*, San Antonio, 2013.

[17] Z. Ding, P. Palafox, K. Moore, R. Chupp and K. Kirtley, "A New 1-1/2 Stage Turbine Wheelspace Hot Gas Ingestion Rig (HGIR) - Part II: CFD Modeling and Validation," *ASME Paper,* Vols. GT 2013-96021.

[18] K.Krishnamurty, "Acoustic Radiation From Two-Dimensional Rectangular Cutouts in Aerodynamic Surfaces," *NACA TN-3487,* 1955.

[19] H. E. Plumblee, J. S. Gibson and I. E. Lassiter, "A Theoretical and Expirimental Investigation of the Acoustic Response of Cavities in an Aerodynamic Flow," *WADD-TR-61-75,* 1962.

[20] L. East, "Aerodynamic Induced Resonance in Rectangular Cavities," *Journal of Sound Vibrations,* vol. 3, pp. 277-287, 1966.

[21] J. Rossiter, "Wind Tunnel Experiments on the Flow Over Rectangular Cavities at Subsonic and Transonic Speeds," *Aeronautical Research Council Reports and Memoranda,* no. 3438, 1964.

[22] H. Heller, D. Holmes and E. Covert, "Flow Induced Pressure Oscillations in Shallow Cavities," *Journal of Sound Vibrations,* vol. 18, pp. 454-552, 1971.

[23] H. Heller and D. Bliss, "Aerodynamically Induced Pressure Oscillations in Cavities - Physical Mechanisms and Supression Concepts," no. AFFDL-TR-74-133, 1975.

[24] L. Shaw, "Supression of Aerodynamically Induced Cavity Pressure Oscillations," *Journal of the Acoustical Society of America,* vol. 66, no. 3, pp. 880-884, Sept 1979.

[25] V. Sarohia and P. Massier, "Control of Cavity Noise," *Journal of Aircraft,* vol. 14, no. 9, pp. 833-837, 1977.

[26] R. Sarno and M. Franke, "Supression of Flow-Induced Pressure Oscillations in Cavities," *Journal of Aircraft,* vol. 31, no. 1, pp. 90-96, 1994.

[27] V. Sarohia, "Experimental Investigation of Oscillations in Flows Over Shallow Cavities," *AIAA Journal,* vol. 15, no. 7, pp. 984-991, 1977.

[28] M. Gharib and A. Roshko, "The Effect of Flow Oscillations on Cavity Drag," *Journal of Fluid Mechanics,* vol. 177, pp. 501-530, 1987.

[29] D. Rockwell and E. Naudascher, "Review - Self-Sustaining Oscillations of Flow Past Cavities," *Journal of Fluids Engineering,* vol. 100, pp. 152-164, 1978.

[30] N. Komerath, K. Ahuja and F. Chambers, "Prediction and Measurement of Flows Over Cavities - A Survey," in *AIAA 25th Aerospace Sciences Meeting,* Reno, NV, 1987.

[31] C. Haigermoser, F. Scarano and M. Onorato, "Investigation of the Flow in a Rectangular Cavity Using Tomographic and Time-Resolved PIV," in *26th International Congress of the Aeronautical Sciences,* Anchorage, AK, 2008.

[32] N. Subrahmanyam and B. Lal, A Textbook of Sound, New Delhi: Vikas Publishing House, 1995.

[33] M. Alster, "Improved Calculation of Resonant Frequencies of Helmholtz Resonators," *Journal of Sound an Vibration,* vol. 24, no. 1, pp. 63-85, 1972.

[34] U. Ingard, "On the Theory and Design of Acoustic Resonators," *The Journal of the Acoustical Society of America,* vol. 25, no. 6, pp. 1037-1061, 1953.

[35] P. Welch, "The Use of Fast Fourier Transform for the Estimation of Power Spectra: A Method Based on Time Averaging Over Short, Modified Periodograms," *IEEE Trans Audio Electroacoustics,* Vols. AU-15, no. 2, pp. 70-73, 1967.

[36] W. Durgin and H. Graf, "Flow Excited Acoustic Resonance in a Deep Cavity: An Analytical Model," *Symposium on Flow-Induced Vibration and Noise,* vol. 7, pp. 81-91,

1992.